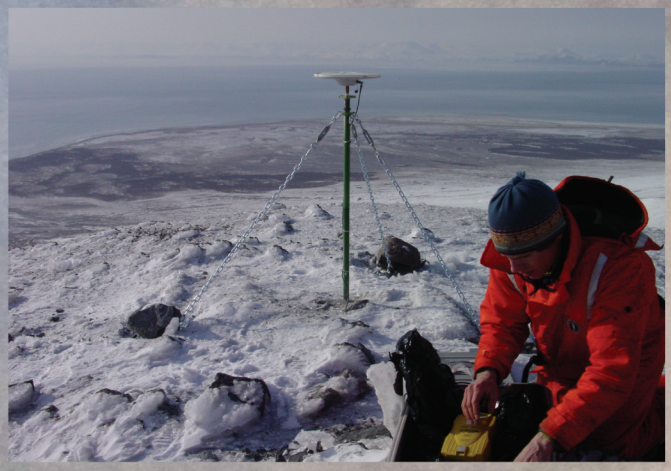
Geodesy













View of the north side of Augustine Volcano on August 7, 2006, showing the 2006 summit lava dome and north lava flow. Alaska Volcano Observatory photo by Michelle Coombs.

The 2006 Eruption of Augustine Volcano, Alaska
Power, J.A., Coombs, M.L., and Freymueller, J.T., editors
U.S. Geological Survey Professional Paper 1769

Chapter 17

Geodetic Constraints on Magma Movement and Withdrawal During the 2006 Eruption of Augustine Volcano

By Peter F. Cervelli[1], Thomas J. Fournier[2], Jeff T. Freymueller[3], John A. Power[4], Michael Lisowski[5], and Benjamin A. Pauk[5]

Abstract

For the first time in the United States, a modern geodetic network of continuously recording Global Positioning System (GPS) receivers has measured a complete eruption cycle at a stratovolcano, Augustine Volcano in Alaska, from the earliest precursory unrest through the return to background quiescence. The on-island network consisted of five continuously recording, telemetered GPS stations, four continuously recording, nontelemetered stations, and about 10 campaign bench marks. The continuous network recorded several distinct and conspicuous signals over the course of the unrest and eruption, starting with a months-long precursory inflation centered beneath the volcano at around sea level. Nearly coincident with the highest volumetric eruption rates, this inflation gave way to a more deep seated deflation that we interpret as a major withdrawal (approx. 25 million m^3 of compressed magma) from a nearly cylindrical magma reservoir centered about 5 km below sea level. Detailed analysis of the geodetic time series reveals additional nuance, including the probable upward propagation of a small dike into the edifice in the 60 days or so before the onset of large-scale explosive activity. Comparisons of the geodetic data and their resulting interpretations with other data, such as earthquake hypocenters and petrologically inferred magma-pressure histories, reveal a kinematic, if not mechanical, account of the 2006 eruption that details the shape and location of the magma source region, the means and velocity of magma transport, and the establishment of a short lived volume- (or pressure-) buffering capability held within the magma reservoir. The cumulative deformation over the course of the eruption shows a large signal close in and high on the edifice that decays rapidly with distance. This pattern indicates a small permanent increase in the edifice volume (beyond that added by the surficial lava dome) but also shows that without close-in (<2.5 km from the summit) stations, the eruption might have been invisible to campaign GPS stations alone.

Introduction

In this chapter we present a comprehensive account of the surface deformation that occurred before, during, and immediately after the 2006 eruption of Augustine Volcano. Following Coombs and others (this volume), we divide the eruption into five phases (table 1). The duration of the five phases, as well as the divisions between them, arises from basic geologic observations. Likewise, from a geodetic perspective, the phases make sense, although the timing of changes in deformation style do not always line up perfectly with the geologically established boundaries. Table 1 also lists, in one- or two-word summaries, general descriptions of the predominant geodetic observations during each phase, along with first-order interpretations. Organizationally, we largely follow this chronological sequence, bracketing the interpretative core of our report with a brief section on metadata at the start and, at the end, with discussions about the enduring changes at Augustine since the eruption.

[1] U.S. Geological Survey, 345 Middlefield Rd, Menlo Park, CA 94025.

[2]Rice University, Department of Earth Science, 6100 Main Street, Houston, TX 77005.

[3]Alaska Volcano Observatory, Geophysical Institute, University of Alaska Fairbanks, Fairbanks, AK 99775.

[4] Alaska Volcano Observatory, U.S. Geological Survey, 4200 University Drive, Anchorage, AK 99508.

[5]Cascades Volcano Observatory, U.S. Geological Survey, 1300 SE Cardinal Court, Vancouver, WA 98933.

Table 1. Phases of the 2006 Augustine Volcano eruption.

[BSL, below sea level; DRE, dense-rock equivalent]

Phase	Start	End	Deformation style	Deformation depth	Erupted volume (DRE; million m^3)[1]
Precursory	August 15	January 11	Slow inflation	Sea level	0
Explosive	January 11	January 28	Slow inflation	Sea level	30
Continuous	January 28	February 10	Rapid deflation	5–6 km BSL	19
Hiatus	February 10	March 3	Sluggish inflation	—	—
Effusive	March 3	March 16	Slow deflation	Shallow	23

[1]Data from Coombs and others (this volume).

In a section on the precursory phase, we revisit and refine the original analysis by Cervelli and others (2006), which treated the precursory deformation in detail but did not extend much beyond this interval. New data analyses, primarily petrologic geobarometry, provide constraints and insights that were not available at the time of Cervelli and others' report. In sections on the subsequent phases of the eruption, we focus on the three most conspicuous deformation signals: (1) the deformation immediately before the initial explosions of January 11, 2006, (2) the deflation approximately concurrent with the continuous phase of the eruption, and (3) the cumulative deformation that occurred over the course of the eruption. In addition to these conspicuous signals, we also present and, where possible, interpret several less distinct deformation features, including a minor inflation during the hiatus after the continuous phase and a small deflation that appears to accompany the effusion of early March 2006.

Each of the conspicuous deformation signals is remarkable it is own right. The precursory deformation before the explosions shows a stunning correlation with the seismic record (Power and Lalla, this volume) and provides strong corroborating evidence for the petrologic (Larsen and others, this volume) and mechanical (Coombs and others, this volume) accounts of the early eruptive processes. The deflation during the continuous phase also constrains petrologic analysis and, along with the petrology, provides insight into the shape and location of the midcrustal magma chamber, along with the timing of magma ascent. The cumulative (or net) deformation over the entire eruption indicates that a large part of the coeruptive deformation—nearly all of it, except for the near-field (<2.5 km from the summit) component—is transient and cannot be imaged without close-in continuously recording instruments or campaign bench marks.

Seeking a broader context, from a geodetic perspective we compare this eruption with eruptions elsewhere, particular at Mount St. Helens, 2004–8. These comparisons lead us to reflect on network design, station placement, the overall role of deformation measurements in volcano monitoring, and future opportunities for improved instrumentation and observation methodologies that promote a cross-disciplinary approach to the interpretation and modeling of volcanic processes. Finally, we emphasize the importance and underutilized potential of continuously recording GPS networks for volcano monitoring and short-term forecasts of volcanic hazard.

Metadata

Station and Observation History

Beginning in summer 2004, the National Science Foundation's Earthscope Project funded the installation of five continuously recording GPS instruments at Augustine Volcano, along with two nearby "backbone" stations (figs. 1, 2). As part of the Plate Boundary Observatory (PBO), these instruments were installed and are maintained by UNAVCO, Inc. (Pauk and others, this volume). Together with the Alaska Volcano Observatory (AVO)'s existing instrumentation and bench marks, these new GPS receivers formed a high-density, proximal geodetic network capable of recording the 2006 eruption and precursory unrest at an unprecedented level of detail. However, the Augustine GPS network had at least one shortcoming—an insufficient number of stations in the intermediate to far field. The size of the island imposes a basic constraint on the aperture size for any network on Augustine. Nonetheless, there was room for improvement, and so, in December 2005, we augmented the network with five additional continuously recording, though nontelemetered, receivers at campaign bench marks AUGB, AUGK, AUGS, A11, A5, (fig. 2), which we refer to below as the semipermanent network. Instrument and antenna information, installation history, and other relevant metadata, including the evolution of station nomenclature, for the permanent and semipermanent networks are listed in table 2.

The precise details of network design, though intended to provide the best possible geodetic coverage of the volcano, were largely constrained by external factors, including telemetry paths, scarce competent bedrock, budgetary limitations, and the inherent danger of working on an active volcano in a heightened state of unrest. The fact that the network in place at the beginning of the eruption was so comprehensive is entirely attributable to the judgment and effort of PBO and AVO engineers. In fact, mathematical deliberations about the strength of model-resolution kernels

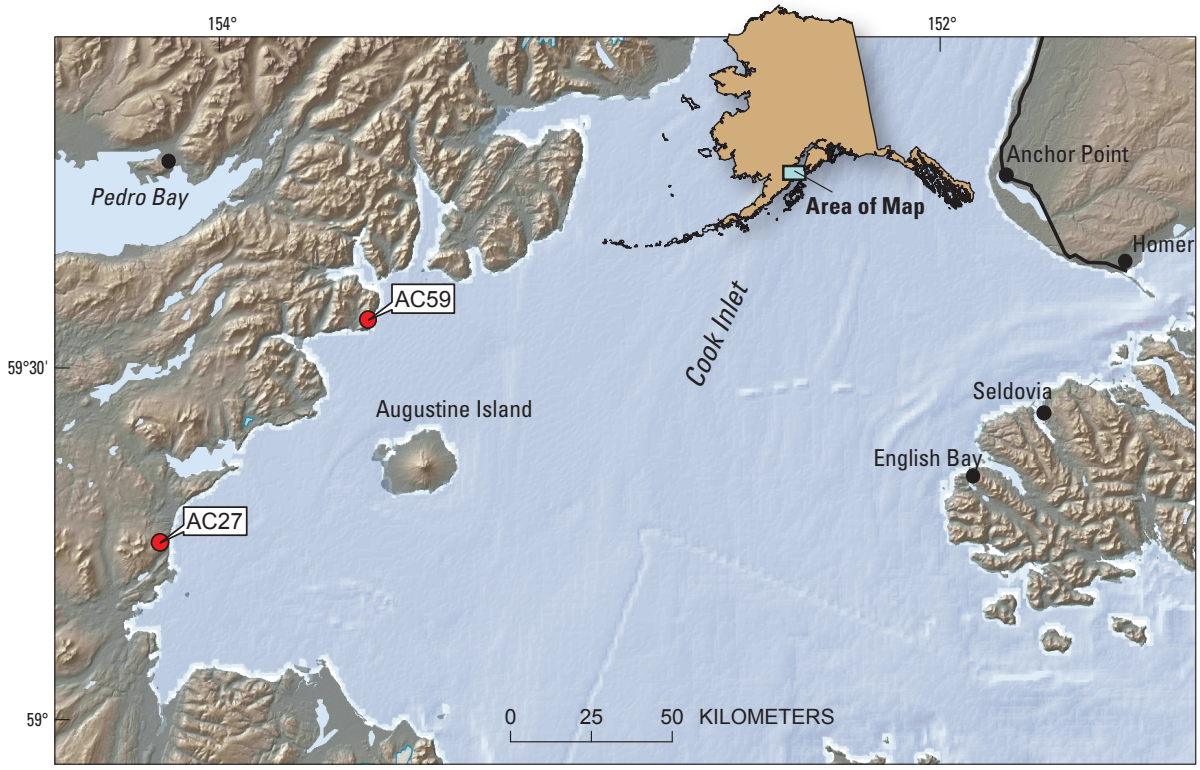


Figure 1. Cook Inlet, Alaska, showing Augustine Volcano, which is about 110 km west of Homer, and Plate Boundary Observatory backbone Global Positioning System (GPS) stations AC27 and AC59. Station AC59, which is used throughout this chapter as a reference station, is far enough away from Augustine to be insulated from volcanic deformation but close enough to measure approximately the same tectonic signal.

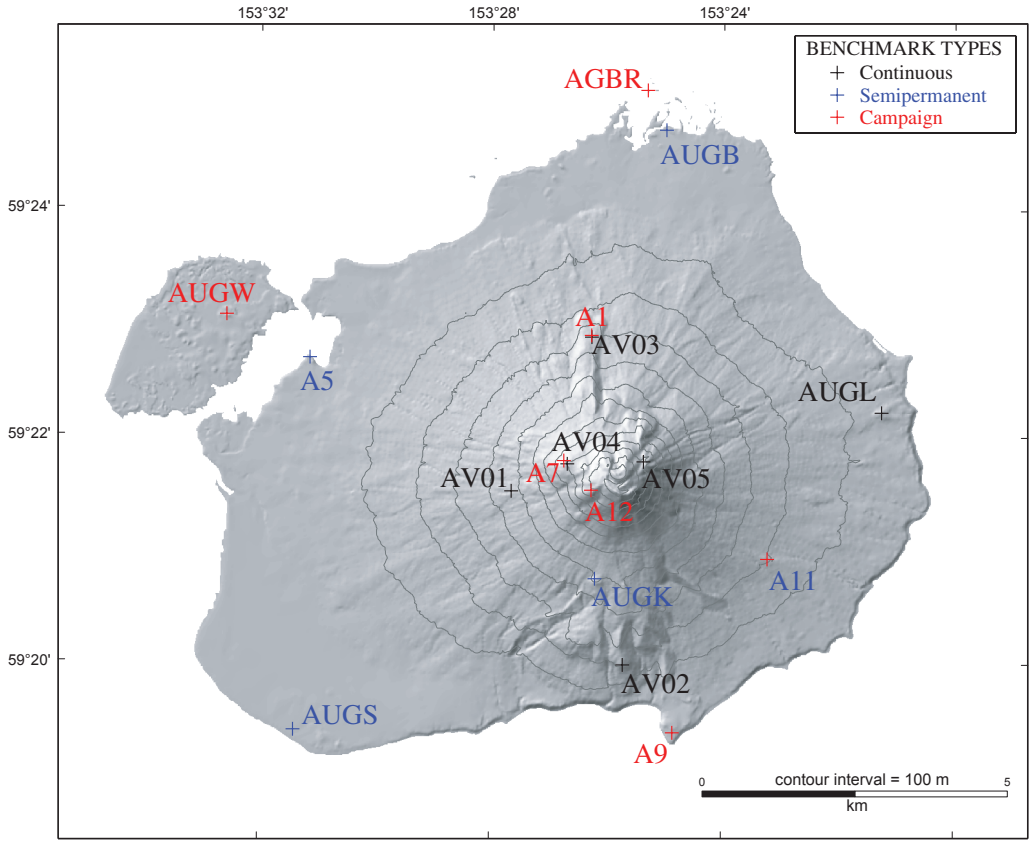


Figure 2. Augustine Island, showing locations of seismic stations in Global Positioning System (GPS) network as it existed in December 2005. Stations AV05, AV04, and AV03 were destroyed during the explosive and continuous phases of 2006 eruption.

Table 2. Instrument metadata and installation history, including station name aliases and other information.

Site Name	Site Name (Pauk and others, 2001)	Site Location		Height (m)	Measurement history			Type	Notes
		Longitude (°W)	Latitude (°N)		2000	2004	2006		
A1	A1	153.437817	59.381555	355.2	•		•	Campaign	
A2	A2	153.424507	59.366622	879.3	•			Campaign	
A3	A3	153.424347	59.367624	865.2	•			Campaign	
A4	A4	153.423468	59.362369	1,055.8	•			Campaign	
A5	A5	153.519228	59.378120	28.9	•	•	•	Semipermanent	Reference station
A6	A6	153.437327	59.371180	677.1	•			Campaign	
A7	A7	153.445662	59.363068	900.6	•		•	Campaign	
A8	A8	153.433094	59.362447	1,218.6	•			Campaign	
A9	A9	153.413985	59.323001	40.9	•		•	Campaign	
A10	A10	153.432707	59.359329	1,243.2	•			Campaign	
A11	A11	153.386769	59.348648	216.9	•		•	Semipermanent	
A12	A12	153.437763	59.358693	1,100.6	•		•	Campaign	
A14	A14	153.425887	59.359396	1,179.9	•			Campaign	
A15	A15	153.428290	59.361713	1,224.1	•	•		Campaign	
A16	A16	153.427410	59.358774	1,219.1			•	Campaign	
A17	A17	153.422530	59.362799	1,038.3			•	Campaign	
A18	A18	153.587795	59.570064	394.9	•		•	Campaign	
AC27	N/A	154.162880	59.252508	417.5		•	•	Continuous	Off island, PBO
AC59	N/A	153.585200	59.567199	308.6		•	•	Continuous	Off island, PBO
AGBR	BURR	153.422443	59.417937	27.8	•		•	Campaign	
AGL1	LU01	153.427329	59.385923	246.2	•	•		Campaign	
AGL2	LU02	153.425045	59.371860	558.8	•			Campaign	
AGWD	N/A	153.437463	59.370604	683.6			•	Campaign	
AUGB	BUR2	153.416421	59.411877	27.5	•		•	Semipermanent	
AUGK	KAMISHAK	153.436557	59.345658	530.9	•		•	Semipermanent	
AUGL	N/A	153.353910	59.370299	104.0		•	•	Campaign	Renamed AV11 in January 2006
AUGM	MOUN	153.355060	59.370688	118.3	•		•	Campaign	80 m from AUGL, therefore excluded
AUGS	SAUG	153.523437	59.323203	28.7	•		•	Semipermanent	
AUGW	WAUG	153.543346	59.384420	44.0	•		•	Campaign	
AV01	N/A	153.460801	59.358531	487.2		•	•	Continuous	PBO
AV02	N/A	153.428391	59.332975	229.8		•	•	Continuous	PBO
AV03	N/A	153.437778	59.381297	360.2		•		Continuous	Destroyed, PBO
AV04	N/A	153.444672	59.362584	915.9		•		Continuous	Destroyed, PBO
AV05	N/A	153.422656	59.362933	1,036.6		•		Continuous	Destroyed, PBO
STEP	STEP	153.764839	59.434311	434.0	•		•	Campaign	Off island

or the degree of independence among the different stations of the network, though important, generally are only secondary considerations, given the logistical conditions in the field at the time of installation.

Previous geodetic field work at Augustine, consisting of electronic distance measurement (EDM) data and theodolite measurements, began in 1986. In 1988 and 1989, an island wide network of 19 trilateration bench marks was installed and measured in its entirety (Power and Iwatsubo, 1998). During 1992 and 1995, GPS surveys occupied parts of this network, but none of these surveys was complete. Additional measurements were made during the summers of 1993, 1994, and 1996. In 2000, a comprehensive GPS survey was undertaken (Pauk and others, 2001). Comparison of the 30 mark-to-mark slope distances measured in 1988 and 1989 with the results obtained from the 2000 GPS survey show differences of less than 5 cm along 24 of these distances. Of the six distances with greater than 5 cm of length change, three involved bench marks high on the 1964 and 1986 lava domes, both of which are known to be unstable and (or) subsiding. The remaining three anomalous distances involved bench marks believed to rest on stable parts of the island; however, no spatially coherent pattern of deformation among these three distances was evident. The locations of the campaign bench marks successfully reoccupied during the extensive geologic and geophysical fieldwork of summer 2006 are shown in figure 2.

Notes on Processing Methodology and Data Quality

Daily GPS solutions were processed with the GIPSY-OASIS software (Zumberge and others, 1997), release GOA4, in network mode, incorporating data from all continuous GPS sites in and around Alaska, using International Terrestrial Reference Frame station ALGO (located in Algonquin, Ontario, Canada) as a reference clock. We applied International Global Navigation Satellite System (GNSS) Service (IGS) 01 elevation-dependent phase-center models for each antenna, with an elevation mask of 10° (see http://www.ngs.noaa.gov/ANTCAL/), using the TPXO.2 ocean-tidal model, and estimated stochastic wet-tropospheric-path delays, using the Niell mapping function (Niell, 1996).

Subdaily solutions were calculated with the program RTD, version 3.0, from Geodetics Inc. (Bock and others, 2004). With RTD, each epoch of the LC (L3) ionospheric-free phase observation is processed independently in network mode to provide a position relative to a fixed master site. Station AUGB (fig. 2) served as the master site for the subdaily processing results presented here. Single-epoch data analysis with RTD is a multistep procedure that resolves integer-cycle phase ambiguities and estimates additional parameters, such as zenith troposphere delays. Our RTD solutions use IGS final orbits, National Geodetic Survey (NGS) elevation-dependent GPS antenna phase-center models, and all observations above 10°.

By late November 2005, enough snow and ice had accumulated at stations AV04 and AV05 (fig. 2) to seriously affect signal quality. Snow and ice accumulation on GPS antennas delays signal transmission along the path from the satellite to the antenna. This delay, unlike, for example, that due to the wet troposphere, is not easily modeled, especially if the size and shape of the obstructing snow and ice mass are unknown. The delays are azimuth and elevation dependent, because the transmission paths through the ice change as the satellites move, resulting in significantly degraded solution quality. However, because large and distinctive postfit phase residuals are diagnostic of unmodeled path delays, we can detect the presence and severity of ice problems without difficulty. At the beginning of each winter, phase residuals increase to more than 25 cm at station AV04, coincident with a large increase in scatter associated with the daily solutions. Phase residuals also increase at station AV05, though much less so—rarely more than 10 cm even at low elevation angles. Station AV05 was located in a higher, more windswept area than station AV04. Although both stations were exposed to similar temperatures and precipitation, higher winds at station AV05 frequently scoured the antenna clean. The net effect of the snow and ice was to make the data from station AV04 essentially unusable during the winter, while station AV05 by and large remained in working condition.

Observations, Interpretations, and Models

Precursory Phase

Though not detected until early autumn 2005, precursory deformation to the 2006 Augustine eruption began in mid-August 2005, as is evident from the baseline length between station AV02 and AV03 (fig. 2), which spans Augustine's summit from north to south (fig. 3). Seismicity began to increase somewhat earlier, at least by April 2005 and possibly as early as October 2004 (Power and Lalla, this volume). Cervelli and others (2006) divided the precursory deformation into three intervals on the basis of deformation style. We preserve these divisions here but rename them slightly for consistency with the rest of the volume. A three-component time series for the station AV05-to-AC59 baseline is plotted in figure 4. Three styles of deformation are evident, named here on the basis of their ultimate interpretations: (1) the inflation stage, (2) the dike-ascent stage, and (3) the preexplosive stage.

Inflation

The horizontal components of the velocity field measured during the early (before mid-November 2005) part of the precursory phase are mapped in figure 5 (black arrows). As noted by Cervelli and others (2006), the deformation pattern

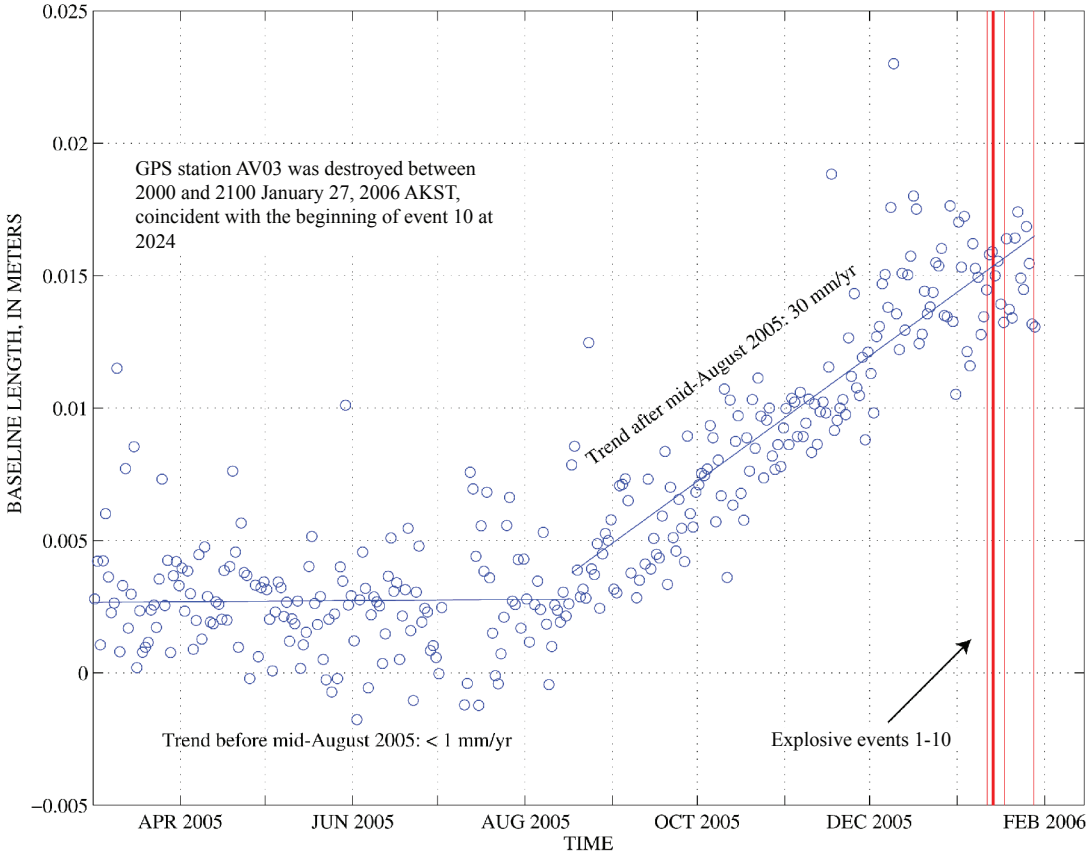


Figure 3. Time series of daily positions indicating distance change (baseline length) between stations AV02 (south of summit, fig. 2) and AV03 (north of summit) on Augustine Volcano between March 2005 and February 2006. Trends are shown before and after mid-August 2005. Vertical red lines denote times of explosive eruptions. These measurements proved extremely useful for forecasting volcanic hazard before destruction of station AV03 by pyroclastic flow on January 27, 2006.

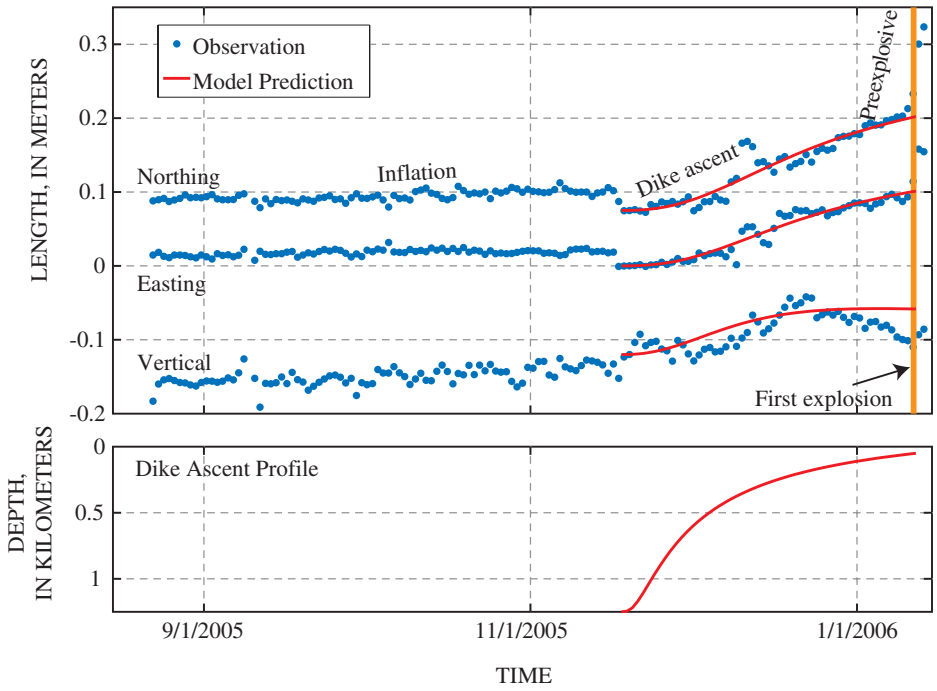


Figure 4. Observed (dots) and modeled (curves) deformation and inferred dike-ascent profile of Augustine Volcano between August 2005 and January 2006. The top panel, easting, northing, and vertical components of observed baseline between stations AV05 and AC59. A positive change in the y-axis direction indicates movement of AV05 eastward, northward, or upward relative to station AC59; a negative change indicates opposite movement. Bottom panel, inferred ascent history of model dike. Predicted deformation from this dike is shown by curves in top panel. Labels in top panel identify divisions of precursory phase. Modified from Cervelli and others (2006).

is clearly radial. The wavelength of the signal appears to demand a shallow source, although the absence of intermediate- and far-field stations introduces some ambiguity into this assessment. The semipermanent network had not yet been established. This deformation field can be modeled with a spherical point source (Anderson, 1936; Mogi, 1958) located approximately at sea level. Because the source depth appears to be shallow, the effect of topography becomes important, especially for comparing the modeled deformation source with other geophysical models on the same vertical datum. For this reason, we included a first-order correction for topography (Williams and Wadge, 1998). The velocities predicted by the model are mapped in figure 5 (red arrows). The predicted vertical velocities agree well with observations at the uppermost stations, AV04 and AV05 (fig. 2); however, the other stations show significantly more uplift than the model predicts. The volume-change rate of the point source is small—about 4×10^5 m^3/yr, or a total volume change of about 2×10^5 m^3. Volume accumulation at this rate would take nearly 200 years to account for the ~7.5×10^7 m^3 of material produced over the course of the eruption (Coombs and others, this volume), and so this small, initial pressurization was likely a slow buildup of volcanic gas beneath a mostly impermeable layer, such as the zeolitized Naknek formation (McClean, 1979).

As discussed below, other deformation models, such as a pressurizing vertical prolate ellipsoid (Bonaccorso and Davis, 1999), can also explain the observed, radial pattern of deformation during the early precursory phase. However, the spatial distribution of stations is insufficient to unambiguously discriminate among different models, especially in light of the high noise level at station AUGL (fig. 2). For this reason, we chose to use the simplest possible model—a spherical point source. Adding complexity will certainly improve data fit, but given that a point source already fits the data almost to within errors, a serious risk of "modeling" noise exists. Given the station distribution, the bottom of the pressurizing body cannot

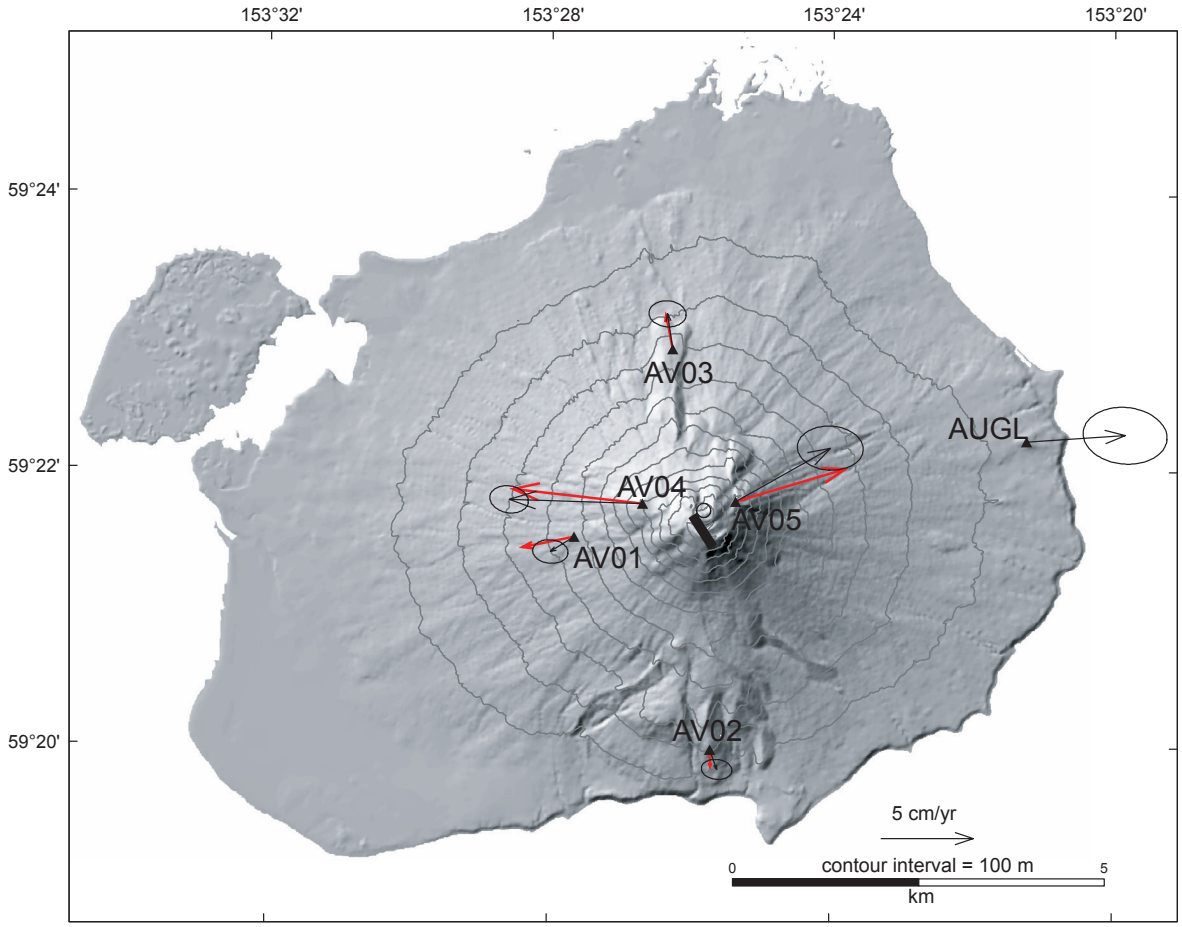


Figure 5. Augustine Volcano showing vectors of observed (black) and predicted (red) Global Positioning System (GPS) velocities relative to station AC59, located approx 24 km northwest (343°) of Augustine (fig. 1), during precursory phase in 2006. Error ellipses indicate 95 percent two-dimensional confidence regions. Predicted velocities are from a point source near sea level. Black circle, horizontal location of the modeled point source of pressurization active during precursory phase. Black bar near summit, surface projection of model dike that was active from mid-November 2005 through early January 2006. Predicted velocity at station AUGL is too small to show in this figure.

be easily constrained, whatever its geometry. The modeled depth of a point source, as mentioned above, probably reflects an impermeable layer rather than the top of a magma body.

Dike Ascent

An abrupt offset appeared in the GPS time series at stations AV04 and AV05 (fig. 2) around November 17, 2006 (fig. 4). By taking the difference between a 4-day mean position before and after November 17, we calculated a displacement of about 3.5 cm to the southwest and an uplift of about 3 cm at both stations. This offset did not appear elsewhere within the Augustine GPS network. Although we did not appreciate its significance at the time of its occurrence (or even its reality as a geologic signal), we now interpret this offset as the abrupt opening of a crack in the Naknek formation above the pressurizing region beneath the summit near sea level. This interpretation is somewhat speculative—there was no earthquake or other geophysical signal associated with the event—and requires that the opening occurred quickly enough to appear abrupt in the daily geodetic time series, but slowly enough (that is, at a low-enough strain rate) for the ductile and, therefore, aseismic failure.

Cervelli and others (2006) argued that magma likely ascended through the edifice in the weeks to months before the onset of the magmatic eruption. The only alternative interpretation is that an active magma column existed within the edifice before the start of unrest, reaching nearly to Augustine's summit. We rejected this interpretation on the basis of the 20-year interval since the latest extrusion and the relatively modest fumarolic temperatures at the summit. Temperatures after the 1986 eruption declined from 870°C in 1987 to about 95°C in the early 1990s. The question remaining, therefore, is whether the magma ascent occurred by the way of dike intrusion or through a diapiric process.

On the basis of the style of deformation observed at station AV05 (figs. 2, 4), we conclude that magma ascent occurred as a dike intrusion. Specifically, the observed change in the vertical component from uplift to subsidence (fig. 4) is characteristic of a shoaling dike, the subsidence arising from a Poisson effect as the rock above the dike is stretched. Further evidence for the dike hypothesis comes from geologic observations of the summit. Beginning in mid-December 2005, features interpretable as extensional became evident, including a new fissure that opened at the summit, striking approximately north (Wessels and others, this volume). Recently analyzed petrologic data (Larsen and others, this volume) indicate that glass compositions in the low-silica- content andesite, believed to be the initial magmatic component of the 2006 eruption, underwent shallow decompression-driven groundmass crystallization before it erupted, an interpretation consistent with the shallow magmatic storage entailed by a dike ascending through the edifice and stalling near the surface for several weeks.

To model the dike, we used rectangular dislocations (Okada, 1985) embedded in a linear, flat, elastic half-space. We then applied a linear least-squares analysis to estimate a dike-ascent history, assuming an exponential model for dike height as a function of time. We assumed an initial depth of 1.25 km and estimated a time constant (or "characteristic" time) for dike ascent and final height as time goes to infinity. We also tried other temporal models, including nonparametric, stochastic models, but observed that only a simple, well-constrained exponential equation fit the data as well as, or better than, any other. Likewise, we tried many different geometric models for the dike and determined that none of them permitted a dike-ascent history with a markedly different (for example, concave upward) ascent history than the one presented here.

The choice for an initial depth of 1.25 km below the top of the half-space was based on the distance between the summit and the location of the pressurizing region near sea level and on the excellent fit of the subsequent model. The dike could have propagated from greater depth, but given the size of the dike—at least when it was in the upper edifice—the existing geodetic network could probably not have detected its presence much below sea level. Thus, choice for initial depth represents an upper limit on the locus of initial dike ascent, rather than our best approximation of where that ascent began.

The estimated dike-ascent history as a function of time is plotted in figure 4. Dike ascent appears to have been begun rapidly, reaching a maximum ascent rate of nearly 100 m per day by November 25, 2005. If this ascent model is correct, the dike came within a few hundred meters of the surface by mid-December 2005, possibly explaining the onset of vigorous steaming and phreatic explosions on December 2, 2005, as well as the local deformation observed at the volcano's summit.

Coombs and others (this volume) argue that the explosions of January 11, 2006, were gas rich, with limited, if any, juvenile magma. They draw this conclusion from the absence of extensive hot flowage deposits and the scarcity of juvenile glassy clasts in tephra-fall deposits (Wallace and others, this volume). Deformation data alone, which are sensitive only to the displacement of the crack wall, cannot differentiate between upward propagation of a gas- versus magma-filled crack. However, given that after the explosions of January 11 no evident reversal of the accumulated deformation occurred, we can conclude that the crack did not close, suggesting that some material remained to keep it open and, in turn, that the observed deformation was, in fact, caused by the ascent of a magma-filled dike, possibly led by a volume of pressurized gas that violently exited in two stages on January 11. Other evidence, as discussed in detail in the next section, suggests that the partially degassed magma from the vanguard dike may have been slowly extruded in the form of a lava dome on January 12 and 13.

Explosive Phase

Average daily solutions, though accurate, are not especially useful for studying quickly evolving volcanic processes. In the hours before the first explosions on January 11, 2006, an energetic earthquake swarm rattled Augustine's summit

(Power and Lalla, this volume), prompting AVO to raise the level-of-concern color code to orange (Neal and others, this volume). Curious to see whether a deformation transient accompanied this swarm, we reprocessed the GPS data, solving for a position at each measurement epoch (every 30 s). We used the RTD processing software (Bock and others, 2004), which estimates each position independently—that is, no temporal smoothing is imposed on the solution time series. This processing methodology requires a stationary reference station, and the resulting solutions are the east, north, and up distances from this origin. Ideally, the reference station should be close enough to the stations of interest so that common error sources (troposphere, orbital errors, and so on) difference out, but far enough away to be outside the deforming area. We opted to use station AUGB (fig. 2), about 5.5 km away from Augustine's summit, as our reference station.

We examined the interval January 9–13, 2006 (UTC). Although the area of station AUGB was slowly deforming from the sea-level inflation source during this interval, the interval is sufficiently brief that the cumulative deformation is well below noise. The time series over the interval at station AV01 is plotted in figure 6. No deformation is evident over the interval on any of the three components, although we know from analysis of the daily solutions that station AUGB and AV01 (fig. 2) were slowly (centimeter per year) moving apart at this time (as primarily evident on the north component of this baseline). The absence of apparent deformation results only from the brevity of the interval under examination. Almost all other stations, except AV04 and AV05, have a similar "flatline" appearance. Icing introduced significant noise in the station AV04 time series. Although icing also affects the time series from station AV05, a signal is still clearly visible beginning around 12:00 a.m. January 11 (fig.7). After the initial explosions midday on January 11, the scatter in hourly median solutions increases, probably because the abundant ash in the air caused unmodeled path delays in the GPS transmissions. The last data were received

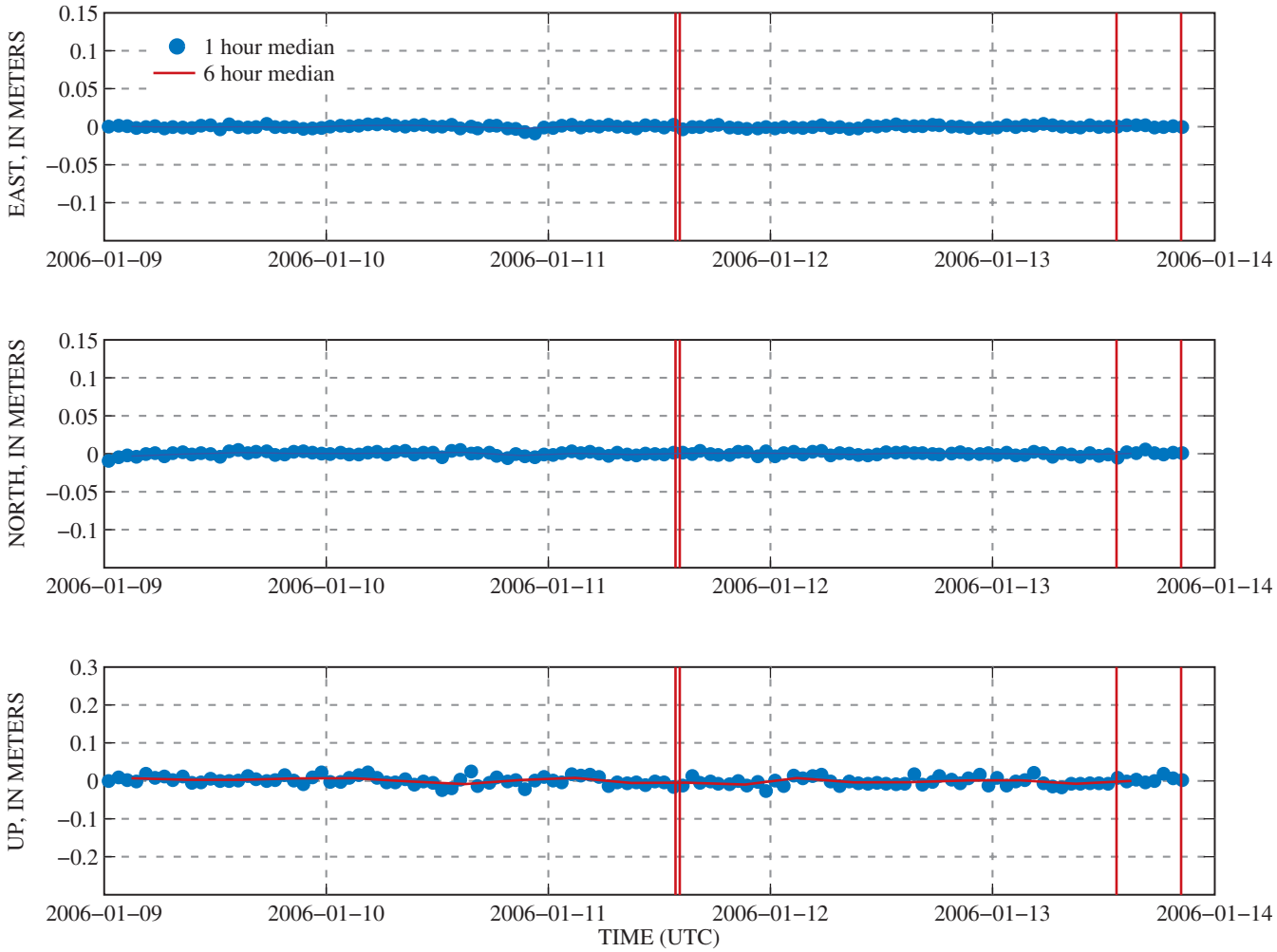


Figure 6. Time series of hourly solutions for distance of station AV01 from station AUGB (fig. 2) on Augustine Island in January 2006. Circles, 1-hour median solutions; curves, 6-hour medians. Note that scale for vertical component is twice that for horizontal components. Vertical red lines denote times of first four explosions. Deformation at station AV01 over this interval is negligible.

from station AV05 at 7 p.m. January 13, just before event 3 (Coombs and others, this volume), which presumably destroyed the station and (or) its telemetry. The signal—an acceleration in deformation—appears unambiguously in the east and north components and is directed northeastward. A vertical signal is difficult to resolve from the noise, but if one exists, it likely takes the form of subsidence.

Inferring a unique mechanical model from a short-lived signal that appears on the record from only a single station is impossible. Nonetheless, close examination of the signal, especially in comparison to seismic signals measured simultaneously, does lead to some interesting insights. The east component of the station AV05 time series, taken as 6-hour medians, is plotted on the same time scale as the Real-Time Seismic Amplitude (RSAM) system at broadband seismic station AU12 BHZ AV (fig. 8; located approx 850 m west of GPS station AV03, fig. 2). The first interesting observation is that the deformation transient begins almost concurrently with the energetic earthquake swarm early on January 11 (Power and Lalla, this volume). Both observations may be explained by upward propagation of a magma-filled crack into the highest part of the edifice. The absence of this signal on the record from nearby station AV01, which is 550 m below and 2,200 m west-southwest of station AV05, strongly suggests that the deformation source is close to station AV05 and, owing to the elevation difference, quite high.

The deformation transient appears to continue for many hours after the explosions of January 11, only to flatten out early on January 12 just as drumbeat earthquakes began to be recorded. Drumbeat earthquakes are commonly associated

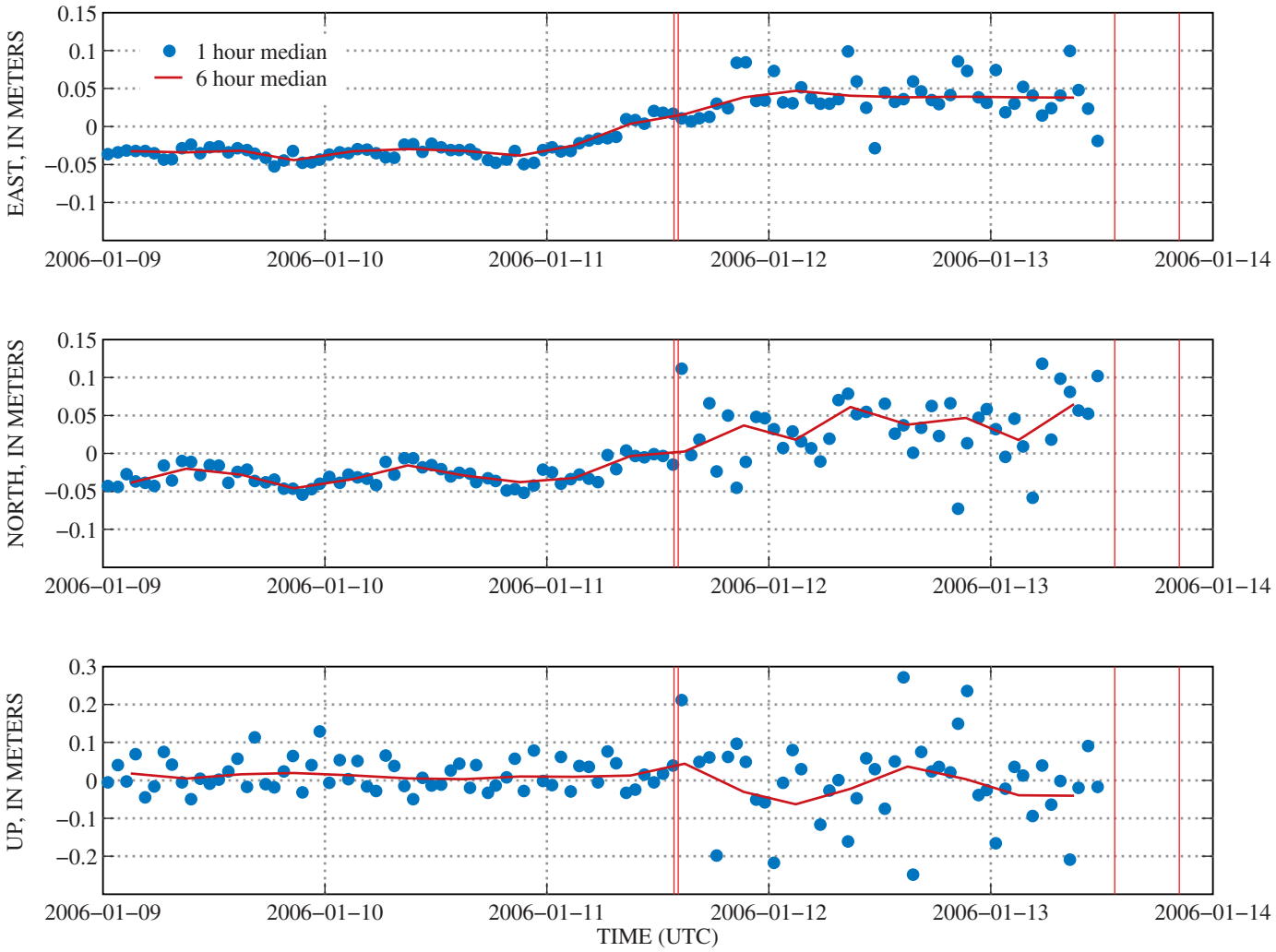


Figure 7. Time series of hourly solutions for distance of station AV05 from station AUGB (fig. 2) on Augustine Island in January 2006. Same scale as in figure 6. Circles, 1-hour median solutions; curves 6-hour median solutions. A clear acceleration in deformation occurs shortly after January 11 in east and north components. Overall noise level relative to station AV01-AUGB is higher, probably owing to a combination of factors, including antenna icing and presence of ash and volcanic gasses near summit. Noise level increases markedly after first explosions (vertical red lines), possibly owing to increased ash emission.

with the extrusion of lava (Moran and others, 2008; see Power and Lalla, this volume). During the period between the first explosions and the beginning of drumbeats, seismic activity declined markedly, in spite of the ongoing deformation. One explanation for this observation is that the explosions relieved the volatile pressure within the tip of ascending magma and removed the driving force behind much of the seismicity. Moreover, the explosions may have contributed to the physical erosion of a pathway for magma ascent. Deformation persisted as the walls of the pathway were pushed apart by the ascending magma. Finally, when lava extrusion began (as signaled by the drumbeats), a quasi-steady state (or open system) was established, and the deformation flattened.

Throughout the explosive phase, the baseline between stations AV02 and AV03 (fig. 2) continued to indicate slow, but unmistakable, extension (fig. 3). Indeed, the rate of extension seemed to remain steady to within measurement uncertainty, suggesting that explosions, individually and in aggregate, did little to relieve pressure within the shallow magmatic system.

Continuous Phase

The geodetic signal associated with the continuous phase of the eruption consisted of a sharp deflation from about January 28 through February 10, 2006. This pattern of deformation has two primary characteristics: it is directed radially inward, and it is uniformly downward. The radial direction of the deformation becomes particularly evident upon transformation to a cylindrical coordinate system. If each station coordinate is represented as a distance from Augustine's summit, then the

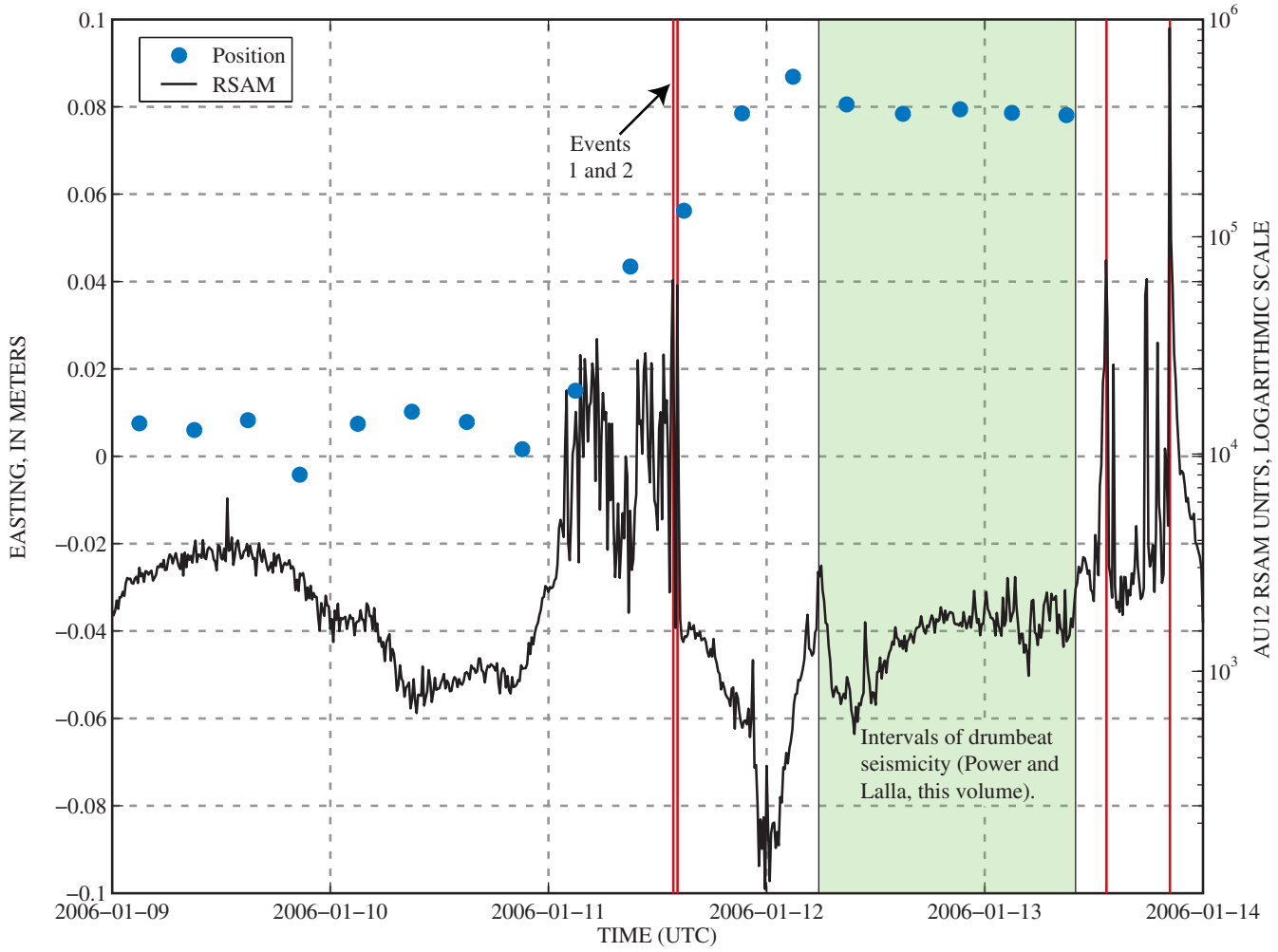


Figure 8. Preexplosive and postexplosive deformation at station AV05 compared to RSAM computed from broadband seismometer AU12. Circles, 6-hour median solutions for east component of baseline between stations AV05 and AUGB; curve, record from Real-time Seismic Amplitude (RSAM) at station AU12 BHZ AV, a broadband seismometer located about 850 m west of station AV03. Note that deformation accelerates suddenly at about midnight January 11, 2006, concurrently with increase in RSAM record corresponding to energetic earthquake swarm that preceded first explosions. Accelerated deformation continued for about 24 hours and then flattened at about the same time when drumbeat earthquakes were first observed (early on January 12).

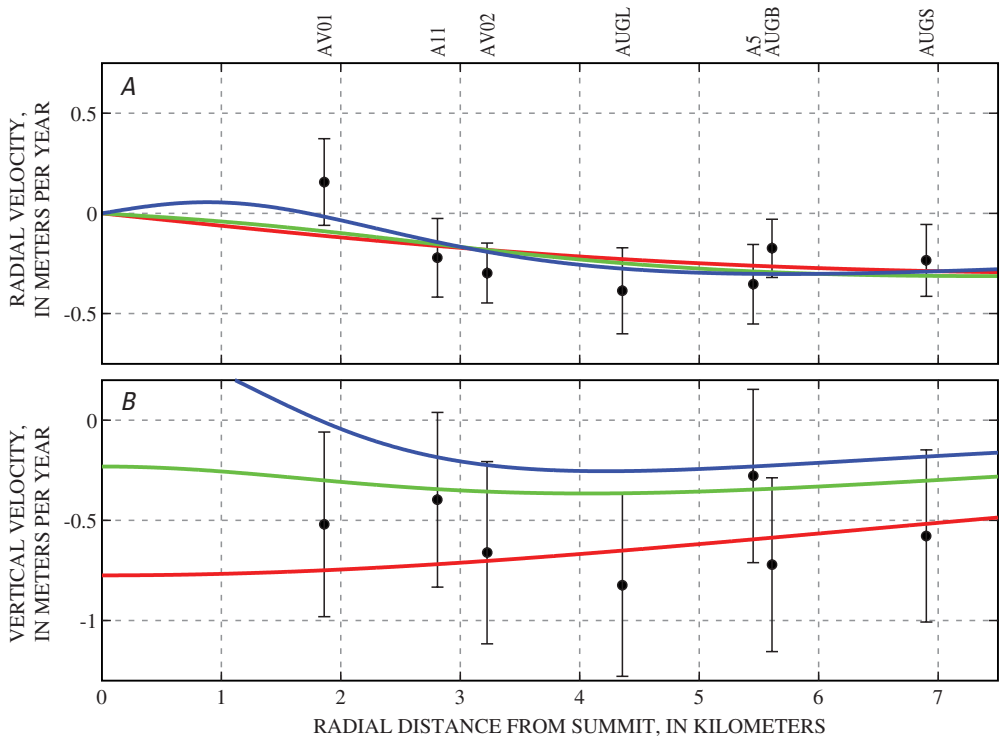


Figure 9. Summit deformation at Augustine Volcano during continuous phase in 2006. Observed velocities (circles) are shown rotated into radial (*A*) and vertical (*B*) components. Error bars are depicted at 95-percent confidence level. Radial component is in direction from observation site to summit. Model predictions over a range of 0 to 7.5 km are given for a spherical point source (red curve), closed pipe (green curve), and an open pipe (blue curve).

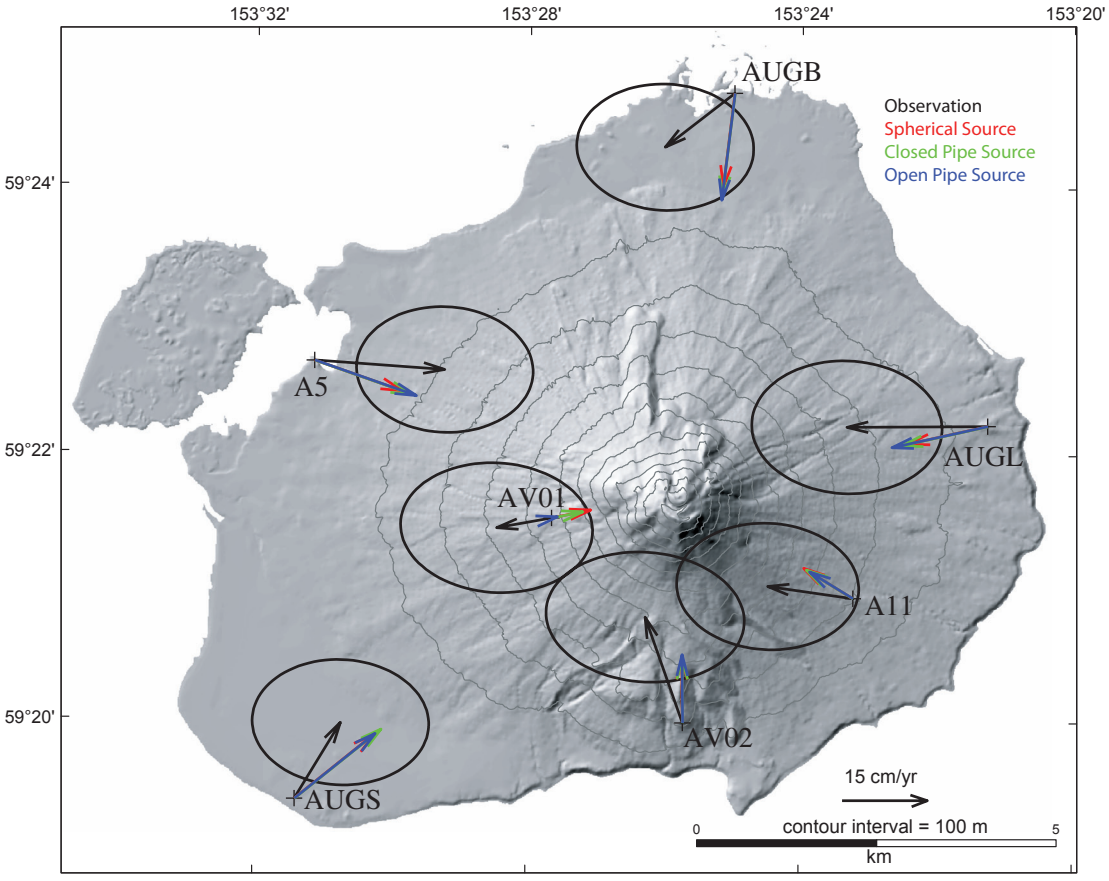


Figure 10. Augustine Volcano, showing vectors of continuous-phase deformation. Error ellipses of observations are scaled by (black vectors) scatter about mean velocity over interval and shown at 95-percent confidence level. Scaled signal-to-noise ratio (SNR) of data (including undepicted vertical components) is ~12; unscaled SNR is about double that. Model predictions are shown for a spherical point source (red vectors), a closed pipe (green vectors), and an open pipe (blue vectors).

three components of deformation can be expressed as (1) radial, motion toward or away from the summit; (2) tangential, motion perpendicular to the direction of the summit; and (3) vertical. In a "purely" radial deformation pattern, the second component will be zero. The estimated GPS velocities during the continuous phase, transformed into radial and vertical components, are plotted in figure 9 and mapped in figure 10. Within uncertainties, no single measurement of tangential deformation is distinguishable from zero, and the scatter about zero shows no obvious positive or negative tendency. The absence of any statistically significant tangential signal all but precludes modeling the deformation pattern with anything other than a radially symmetric source centered at the summit. Although the presence of a shear source, dike, or sill cannot be ruled out, if such a source was active during the continuous phase, it did not produce sufficient deformation for positive resolution.

Figures 9 and 10 also show that the radial deformation measured at the nearest station to the summit differs in sign from that measured at all other stations—station AV01 (fig. 2) actually appears to have moved away from the summit during the deflation of the continuous phase. Taken as an individual measurement, the previous observation is not decisive to within uncertainties; however, given that every other measurement is, within uncertainties, less than zero (directed toward the summit) the apparent sign difference is probably real. The overall trend of the radial deformation shows a gradual increase in motion after a sign change at around 2.5 km, reaching a maximum at about 4.5 km and flattening beyond that. Although the deformation almost certainly extends farther than the coastline, no measurements are available, except for the distal PBO backbone sites (stations AC27, AC59; fig. 1), where no volcanic deformation is visible.

The observed vertical deformation appears to be constant at all stations at about -0.55 ± 0.4 m/yr. Thus, the vertical deformation is distinguishable from zero, although no convincing trend in the magnitude of deformation as a function of radial distance is apparent. The uniformity of the vertical signal suggests a possible correlated noise source. For example, because the calculated velocities are relative to a stationary (over this short interval) station on the Alaska Peninsula, AC59 (fig. 1), position errors at that station can lead to correlated error across the network of remaining stations. The uniformity of the vertical signal, however, does not stretch to include the station AC27, 44 km southwest of Augustine (fig. 1), which, unlike the other seven stations, appeared to rise somewhat relative to station AC59 over the interval under consideration. Therefore, the uniformity—at least in sign if not in value—of the vertical signals probably reflects a volcanic process and not simply measurement error.

Given the abundance of erupted material, about 25 million m^3 each, during the explosive and continuous phases (Coombs and others, this volume), we conclude that the deflation imaged by the GPS network resulted from the withdrawal of magma out of a storage area, or chamber, at depth. Regarding this chamber, geodetic measurements can shed light on three main questions: (1) what is its shape? (2) how deep is it? and (3) how much did it contract?

Modeling Deformation During the Continuous Phase

The deformation observed during the continuous phase, though large when expressed as a rate, was quite small in terms of absolute displacement. Indeed, the signal-to-noise ratio (SNR), defined as the norm of the weighted data vector, of the geodetic measurements from the continuous phase was about a sixth that of the SNR of the precursory phase through mid-November 2005. Models of geodetic measurements with such modest SNRs are not likely to be well constrained or even unique. Nonetheless, modeling can be useful in ruling out interpretations that would otherwise remain plausible. Furthermore, although individual model types and their associated parameters are typically not well constrained with low SNR, constraints can be imposed on classes of models and ranges of model parameters, particularly when other corroborating data are available.

The first deformation source that we consider is a spherical point source (Anderson, 1936; Mogi, 1958), exactly the same source type as the one we used to model the precursory inflation. Maximum radial deformation from a spherical point source occurs at a distance of source depth over $\sqrt{2}$. Simply on the basis of inspection of the observed data in figure 5, a spherical point source must be at least 7 km deep to fit the observed horizontal deformation. Maximum vertical deformation from a point source occurs directly above the source and is inversely proportional to the square of source depth. The vertical deformation decays to half its maximum value at a distance of about 3/4 of a source depth. This fact, in combination with the large and uniform subsidence signal, suggests that a source depth greater than 10 km would be required to fit the data well.

In addition to a spherical point source, we also consider two additional deformation models—closed and open pipes (Bonaccorso and Davis, 1999). Both of these models share a similar geometry, although we model a closed pipe as a degenerate ellipsoid with equal semi minor axes, and an open pipe as a cylinder. Both models are parameterized similarly: (1) easting, (2) northing, (3) depth to the top of the pipe, (4) depth to the bottom of the pipe, (5) the pipe's semiminor axis (radius), and (6) a source strength. The two models differ with respect to the boundary conditions on the pipe walls. A closed pipe is characterized by constant pressure change on the pipe walls, while the conditions for a open pipe stipulate constant displacement on the pipe walls, along with zero pressure change at its top and bottom. The effect of this difference is that for an open pipe, no excess upward force (that is, force other than lithostatic) is exerted on the top of the pipe, hence the "openness." In an open pipe the source strength is a length change (a displacement), whereas in a closed pipe it is a pressure change.

Bonaccorso and Davis (1999) gave approximate expressions for surface deformation from both types of pipe, the approximation stemming from the fact that the boundary conditions on the cylinder walls are not met exactly. Results are accurate, however, if the cylinder radius is small relative

to its height and depth. Mathematically, the level and characteristics of the approximation are similar to that of a spherical point source—an infinitesimal representation of a finite body. Indeed, a spherical point source, which approximates the deformation from a pressurized spherical cavity, also becomes more accurate as the ratio of the source depth to the source radius increases. Segall (2010) notes that the expressions of Bonaccorso and Davis (1999) are not general and apply only when Poisson's ratio equals 0.25. Segall (2010) provides the general expressions, which we employ here.

We derived the three-dimensional deformation fields (that is, deformation in the body as well as at the surface) for both pipe models, which permits the maximum displacement on the pipe walls to be calculated. This calculation, in turn, allows source strengths to be characterized as approximate volume changes rather than pressure or length changes. In the volume derivations that follow, for the sake of simplicity we use expressions for the internal deformation in an elastic full space (rather than a half-space). This simplification should yield satisfactory levels of approximation, provided that the tops of the pipes are well below (kilometers) the actual ground surface (that is, the top of the half-space).

In a closed pipe, the maximum displacement of the pipe wall, which occurs at the middle of the pipe along its height, is given by:

$$u_{max} = \frac{a\,p}{2\,\mu},$$

where a is the pipe's semi minor axis (radius), p is the pressure change, and μ is the shear modulus. Using the maximum-displacement term, a volume change can be estimated. For a closed pipe, the total volume is given by the formula for an ellipsoid:

$$V = \frac{4}{3}\,\pi a^2\,\frac{h}{2},$$

where V is total volume and $h/2$ is the semi major axis. Taking the first term of the Maclaurin Series of V as a function of a yields a simple approximation for volume change:

$$\Delta V = \frac{4}{3}\,\pi\,a\,h\,u_{max}.$$

Earlier, we referred to a "source strength" for closed and open pipes. We can extend this notion to a "potency," which is essentially a lumped parameter in the expressions for deformation that does not depend on the either the location of the observation coordinate or the source. In a closed pipe, the potency is given by:

$$P_{\mathrm{cp}} = \frac{a^2 \rho}{4\,\mu}.$$

Substituting this term into the equation for volume change yields an expression for volume change that depends on only the potency term, thereby side stepping the necessity for estimating a source radius, pressure change, and shear modulus:

$$\Delta V = \frac{8}{3}\,\pi\,h\,P_{\mathrm{cp}}.$$

In an open pipe, the maximum displacement on the pipe walls is given by:

$$u_{max} = \frac{s}{2(1-\upsilon)},$$

where s is the displacement and υ is Poisson's ratio. Following an analysis similar to above, we can estimate the volume change for an open pipe as well. The total volume of an open pipe is given by the formula for a cylinder:

$$V = \pi a^2 h,$$

where V is total volume and h is the cylinder height. Again, taking the first term of the Maclaurin Series we get an approximation for volume change:

$$\Delta V = 2\,\pi\,a\,h\,u_{max}$$

The potency term for an open pipe is given by:

$$P_{\mathrm{op}} = \frac{a\,s}{8(\upsilon - 1)},$$

which leads to an expression for volume change in terms of potency:

$$\Delta V = 8\,\pi\,h\,P_{\mathrm{op}}.$$

Again, because of this expression, we can focus on the volume change, side stepping the need to estimate the source radius and the displacement on the pipe wall. We note, however, that for our purposes, Poisson's ratio is not estimated but assumed. Through this analysis, we set Poisson's ratio equal to ¼.

Modeling Results and Discussion

In spite of our earlier remarks that a spherical point source must be quite deep to fit the data well, we nonetheless inverted for such a source, solving for depth and volume change. In contrast to the precursory source, near sea level, the potential source depths for the deflation observed during the continuous phase seem to be considerably deeper. Indeed, we surmise that they are large relative to the scale of regional topography, and so, for the sake of simplicity, we chose to dispense with a topographic correction. Imposing no constraints other than fixing the horizontal position of the point source to the coordinates of Augustine's summit, justified by the absence of deformation in the tangential direction,

the inversion reduces to a simple search over a range of depths, linearly solving for the best-fitting volume—change rate at each iteration. The optimal model prediction is plotted in figure 9 and mapped in figure 10. The model both fails to predict the near-field sign change in the radial component and systematically underpredicts the vertical deformation but fits observations satisfactorily, given the low SNR of the data.

The results of our inversion for a spherical point source by depicting a "misfit" space for this model are plotted in figure 11. The solution that minimizes the misfit occurs at about 12.5-km depth, and corresponding to a volume loss of about 16.5 million m^3 over the interval of the continuous phase. Here and below, we quantify misfit as the difference between observation and prediction as measured by the mean squared error (MSE), a weighted L2 norm of the residual vector scaled by the number of data points less the number of free model parameters. The MSE for a best-fitting point source is approximately 2. We note that a substantial, diagonally trending region (dark blue area, fig. 11) of the graph also shows a relatively low misfit (MSE ≈ 2), indicating a significant correlation between volume loss and source depth and therefore some freedom to choose among precise pairs of these values.

Ideally, a quantitative statistical test could delineate a misfit boundary beyond which the observed data are violated. However, the non linearity of the inversion problem, exacerbated by the low SNR of the data in question, severely complicates such an analysis. For example, see Cervelli and others, 2000, for a discussion of applying an approximate *F*-test to non linear problems. Misfit graphs like that shown in figure 11 obviate these difficulties to a certain extent by presenting a quantitative account of how variations in the model parameters affect misfit when the parameters are considered both individually and together. We can then make qualitative assessments about ranges of plausible model parameters, although we still lack an objective, numerical criterion for when a certain set of model parameters is simply impermissible.

Because our data signal is weak, we cannot use the data alone to uniquely constrain a particular deformation source. We have just shown that the data can be fitted reasonably well by a spherical point source centered below the summit. The pipe sources considered below are geometrically more complex than the spherical source and should also fit the data well. The main questions, therefore, are: do the pipe models improve data fit in a statistically significant way? and, perhaps more importantly, are any of the models tested better suited to other (for example, petrologic, seismic) data?

The question arises as to whether to consider a closed pipe at all. We know that at least to a certain extent, the system was open during the continuous phase because the volcano was erupting throughout this interval. Yet we cannot simply dismiss closed models, including spherical and nondegenerate ellipsoidal sources (for example, Yang and others, 1988), both of which share the same pressure boundary conditions with a closed pipe, as useless. Eruptions necessitate a connection with an underground magma body; however, even in the event of continuous extrusion, the extrudate itself does exert some downward force or overpressure by way of its own mass (gravity), from internal friction, or from friction along the conduit walls. Likewise, the question whether

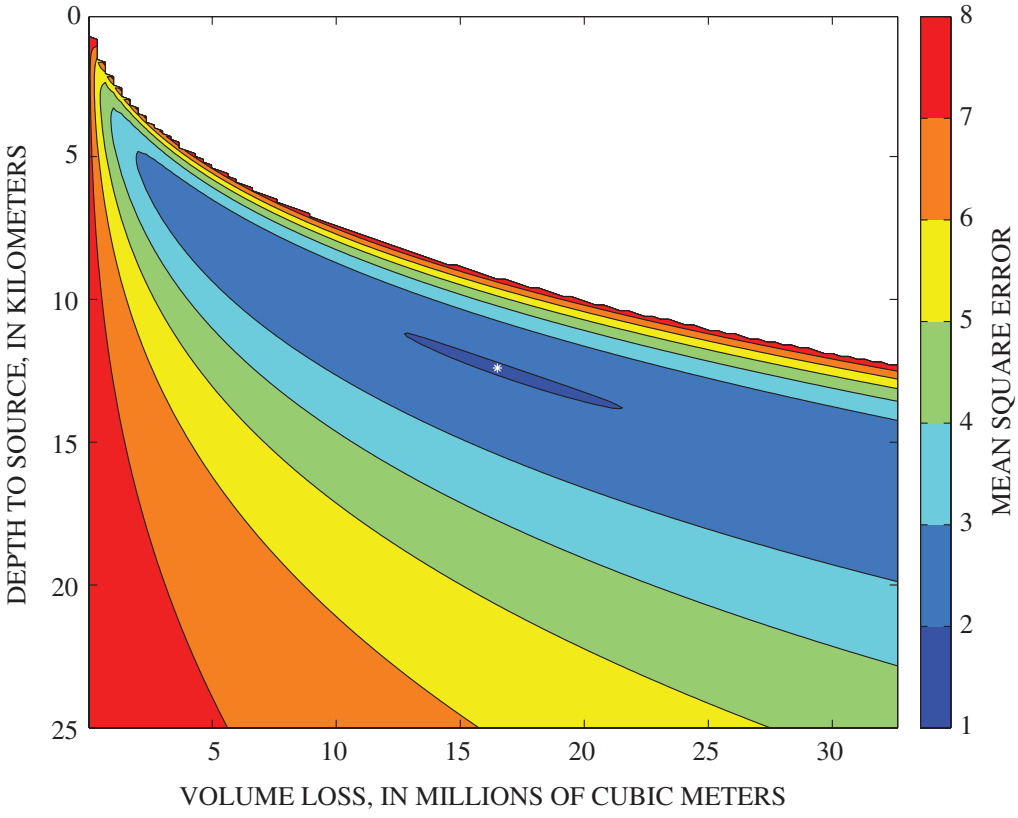


Figure 11. Model misfit for a point source. Colored regions depict misfit as a function of point source depth and volume loss based on measured velocities during continuous phase of 2006 eruption of Augustine Volcano (fig. 1). Model that minimizes misfit (white star) is about 12.5 km deep, with a volume loss of 16.5 million m^3 over interval.

an open pipe is a useful model also arises. What does it mean for a pipe to be "open" when it has a top depth of kilometers below sea level with a column of rock and magma above it? We note that both of these sources model not absolute pressures but changes in pressure over an interval. After deformation, an open pipe is not required to exert zero pressure at its top; instead, the net pressure change must be zero, and the total displacement on the pipe walls must be everywhere constant.

To evaluate data fit (that is, MSE) for both pipe models, we vary the pipe height and the depth to the pipe top over a wide range, using least squares to solve for the optimal potency parameter for each height/depth pair. As for a spherical point source, the horizontal positions of the pipes are constrained to lie directly at Augustine's summit. The results of these analyses are plotted in figures 12 and 13, which depict the misfit space for closed-and open-pipe models, respectively. Also shown are the contours of volume change, so that for any point on the graph, misfit for a given set of the three parameters can be determined. The observed deformation from both the closed and open pipe models are plotted in figure 9 and mapped in figure 10. We note that in figure 10, all the predicted deformation vectors point in the same direction, although their magnitudes vary. This relation stems from the radial symmetry of the source models and the constraint that horizontal coordinates of the models lie at the origin (Augustine's summit).

All of the tested model types—point source, open pipe, and closed pipe—fit the data adequately. Each model has a corresponding region in its misfit space bounded by an MSE of about 2, which is a reasonable fit to the data, given the 95-percent-confidence-level

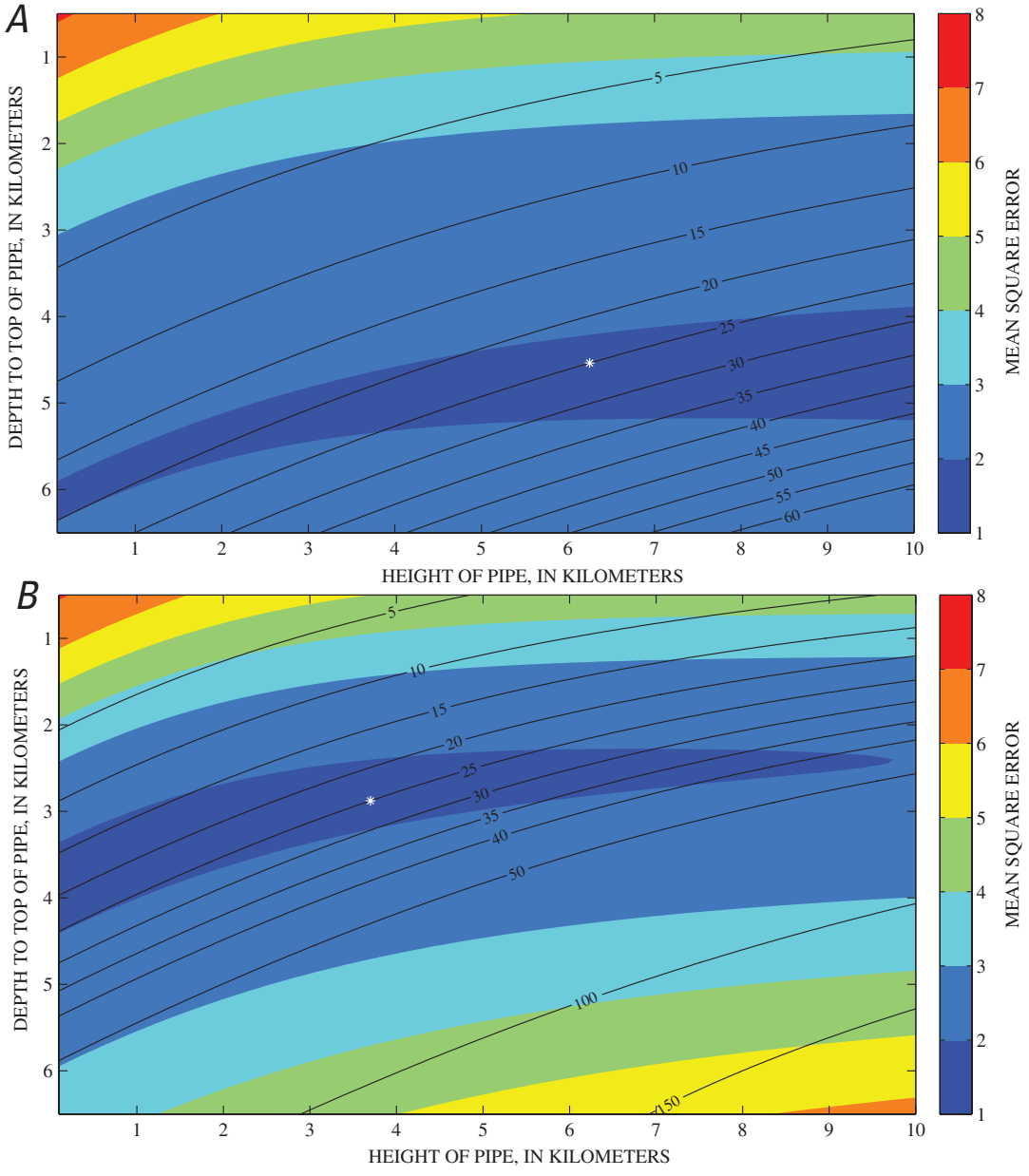


Figure 12. Model misfits for closed (*A*) and open (*B*) pipes. Colored regions depict misfit as a function of depth to pipe top, height of pipe, and volume loss (shown as contours). A substantial plausible region (MSE approx. 2) exists in misfit space, and so a precise set of model parameters is not mandated by data. However, by constraining volume loss to 25 million m^3, a specific top and height are entailed (white star).

uncertainty ellipses. The differences in misfit (that is, the difference between observations and predictions) among the models are not large and certainly not statistically significant. Misfit, therefore, cannot be a sole criterion for favoring one type of model over another. Each model type has different consequences that can be compared with other, nongeodetic data, enabling us to move beyond the mere satisfaction of a necessary condition—data fit—into the realm of sufficient conditions for determining which, if any, of our models is a useful approximation to a real geologic structure.

Petrologic analysis, including Al-hornblende geobarometry from Holocence fall deposits, indicates magma-storage pressures corresponding to no greater than 9-km depth (Tappen and others, 2009). Moreover, melt inclusions obtained from 1986 and older deposits suggest crystallization depths of less than 8 km (Roman and others, 2005; see Webster and others, this volume), and melt-inclusion volatile contents from 2006 high-silica andesite, erupted during the continuous phase, indicate pressures as high as 100 MPa, equivalent to depths of 3 to 4 km (Webster and others, this volume). All of these studies seem to contradict the 12.5-km depth of the point-source model. Indeed, even if we relax the data-fit requirement, figure 11 shows that to achieve a source depth consistent with the petrologic depth constraints, only a small volume loss (~ 5 million m^3) is needed. This value is only a tenth of the volume of magma erupted by the end of the continuous phase, a discrepancy that seems too large, even accounting for magma compressibility.

The geodetic data do not fully constrain the parameters for either a closed or an open pipe. "Plausible" regions bounded by the condition that MSE ≈ 2 are plotted in figures 12 and 13. These regions cover fairly extensive areas: 17 percent of the total graph for a closed pipe and 13 percent for an open pipe. Defining the plausible regions as bounded by MSE ≈ 2 is somewhat arbitrary, though not without justification. Sorted lists of MSE values for each pipe model, when plotted, show plateaus of MSE ≈ 2, with the values increasing sharply thereafter, implying that the plausible regions are, as well as being compatible with the data, well constrained, at least with respect to the total range of calculated misfits.

For a closed-pipe model, the plausible region extends to (and, though not plotted beyond) the right side of figure 12, corresponding to pipe heights of 10 km and greater. The data poorly constrain the height of a closed pipe or putting it another way, the depth to the pipe bottom. The only firm check on a closed pipe's height is the absence of observed deformation at the far- field PBO site AC29, 44 km WSW of Augustine (fig. 1).

For both closed and open pipes, the contour corresponding to 25 million m^3 of volume change runs through the middle of the plausible regions. This contour also has the property—again, for both pipe models—of having a well-defined

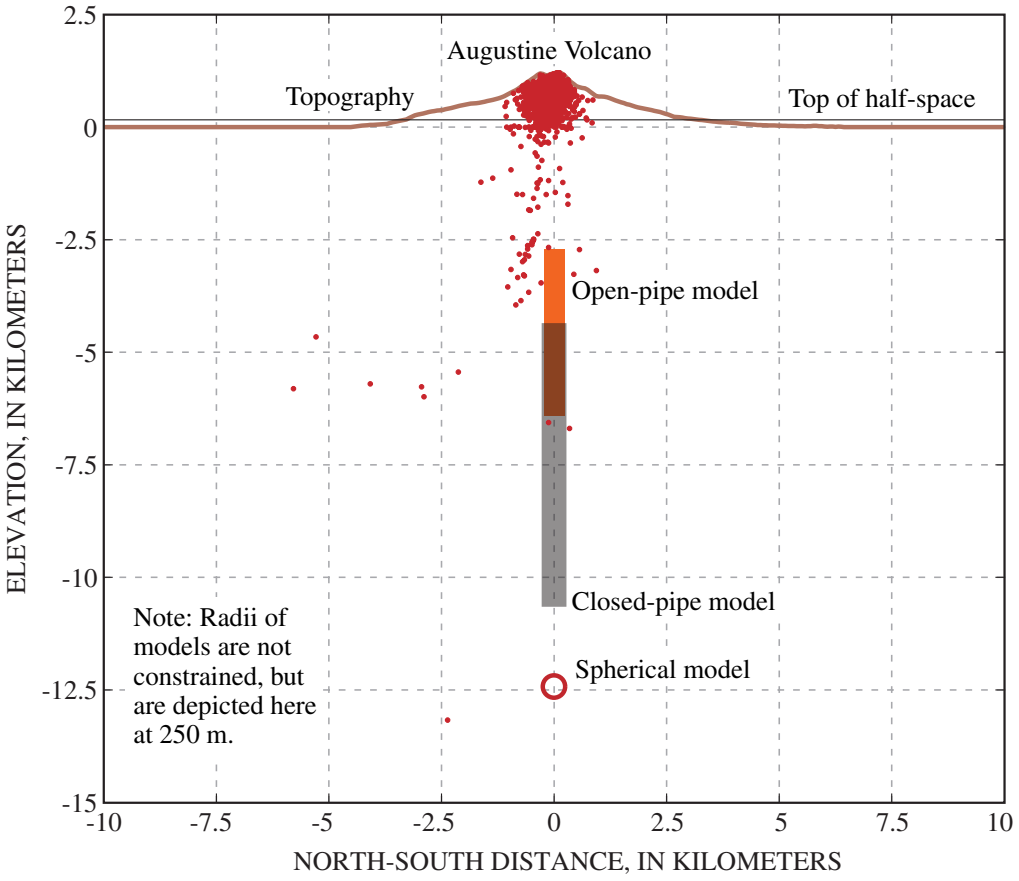


Figure 13. North-south cross section of Augustine Volcano (fig. 1), showing cross-sectional view of three source models under consideration for deflation during continuous phase, along with topography (brown curve), hypocenters (red dots), and top of elastic half-space (black horizontal line). Red circle, optimal point-source model; gray rectangle, favored closed-pipe model; orange rectangle, favored open-pipe model. Radii of pipes and sphere are conceptual and not constrained by data.

minimum MSE along its length, enabling us to focus on specific pipe depths and heights. In contrast, the misfit curves corresponding to the adjacent contours (20 million and 30 million m^3) do not exhibit such well-defined minimums. By this means, we choose our preferred parametrizations for open and closed pipes from among all possible values within the plausible regions. The preferred depths and heights for both pipe models are shown in figure 12 and 13 (white stars), and the models themselves are depicted in cross section in figure 13. Numeric descriptions of our preferred models are listed parametrically in table 2.

We note that the 25 million m^3 volume change value agrees well with the estimated eruptive output during the late explosive phase and continuous phase, and might then conclude that geodetic measurements are imaging a simple correspondence between magma withdrawal at intermediate depth and lava and tephra eruption at the surface. Several questions complicate this simple interpretation. Why, during the explosive phase, when 30 million m^3 of material was erupted, did no corresponding volume-loss signal occur in the geodetic data? Indeed almost half of this volume was erupted in the last 2 days of the explosive phase, and yet still no geodetic signal was observed. Second, why, during the hiatus, after the magmatic pathway had been thoroughly reamed out, was there another—albeit minor—episode of inflation? And third, why, during the effusive phase, was still another 25 million m^3 of lava extruded as a lava dome, with only a negligible deflation signal, much smaller than that observed during the continuous phase when a similar volume of lava was erupted?

Experience has shown that geodetic estimates of volume change are consistently too small relative to observed erupted volumes (for example, Owen and others, 2000). Mastin and others, (2008) addressed this discrepancy by noting that the ratio of the eruptive volume (dense-rock equivalent, or DRE) to the geodetically measured deflation volume depends on both the compressibility of the magma and the magma reservoir. Specifically:

$$\frac{V_e}{\Delta V} = -\left(1 + \frac{\kappa_m}{\kappa_c}\right),$$

where V_e is the erupted volume, ΔV is the geodetically inferred volume loss, κ_m is the magma compressibility and κ_c is the compressibility of the magma reservoir. For magma from the 2004-8 Mount St. Helens eruption, Mastin and others (2008) estimated that κ_m fell in the range 3×10^{-10} to 5×10^{-10} Pa^{-1}, whereas κ_c was about 1×10^{-10} to 1.5×10^{-10} Pa^{-1}, implying a $V_e / \Delta V$ ratio of about −4. Magma from the Mount St. Helens 2004–2008 eruption was notably degassed (Gerlach and others), resulting in an abnormally low compressibility. For the more gas- and bubble-rich magmas of Augustine, we estimate κ_m at about 1×10^{-9} Pa^{-1}. Because the P-wave velocity in the vicinity of the magma reservoir at Augustine is lower (~ 5.6 km/s; see Power and Lalla, this volume) than at Mount St. Helens, we estimate, using the methodology of Mastin and others (2008) and accounting for the differently shaped chamber geometries, κ_c at Augustine at about 5×10^{-10} Pa^{-1}. Together, these two compressibilities values yield a $V_e / \Delta V$ ratio of about −3.

Leaving aside for the time being the question whether the appropriate deformation model at Augustine is a closed or open pipe, we argue that the deflation observed geodetically during the continuous phase accounts for almost all the material erupted from Augustine in 2006. The 25-million m^3 volume, scaled by a $V_e / \Delta V$ ratio of about −3, amounts to a total volume loss of about 75 million m^3, quite close to the geologically estimated eruptive volume (Coombs and other, this volume). But how was 30 million m^3 of material erupted during the explosive phase before any geodetic deflation occurred? We suggest that during the explosive phase of the eruption, the gas-rich magma behaved as a "volume buffer." As the eruption proceeded, the pressure in the magma reservoir would instantaneously drop, leading to more bubble creation, which, in turn, kept the pressure (and volume) in a dynamic balance. Eventually, however, enough gas would exsolve and enough magma would erupt to overcome the buffering capacity of the reservoir, leading to a sharp pressure loss, a strong geodetic deflation signal, and the boilover characterizing the continuous phase. Left behind after all this activity would be a slug of relatively degassed magma high in the plumbing system, possibly in the edifice itself, which would eventually be extruded during the effusive phase, driven by a small excess pressure created as the main magma reservoir viscously reequilibrated.

The question remains of how to choose between the closed- and open-pipe models. A closed pipe is overall a deeper and more extensive magma reservoir model than an open pipe. Accounting for the difference between the top of the half-space and the top of the edifice, a closed pipe begins at about 4.5 km below Augustine's summit and extends for another 6 km. In contrast, an open pipe begins at about 2.6-km depth and continues for a little less than 4 km. Are these differences in depth sufficient to favor one model over another on the basis of the constraints from other data? Hypocentral locations of the relatively few earthquakes that occurred beneath Augustine cluster near 3.5 km below sea level (Power and Lalla, this volume), coinciding with the open-pipe-model position. Larsen and others (this volume) infer that most eruptive products during the continuous phase came from a depth of approximately 4 to 6 km below the summit and that melt-inclusion analysis suggests crystallization depths of less than 8 km (Roman and others, 2005; see Webster and others, this volume). Both the hypocenter data and the petrologic analysis seem to slightly favor an open-pipe model, but neither the data nor the analysis is absolutely determinative.

Careful examination of the predictions data from the two pipe models shows two potentially distinguishing characteristics: first, the closed-pipe model fails to capture the near-field curvature (sign change) in the radial deformation; and second, the open-pipe model systematically underpredicts the vertical deformation. These two shortcomings lead to speculation as to

whether a hybrid, or "partially open," source may be at work. Indeed, distinguishing "open" from "closed" sources may not be just a simple choice of one over the other but, instead, the identification of a point on a continuum between a completely closed and a completely open magmatic system. Along with fitting the data better, a hybrid model might also be more physically realistic, in that it would capture the essential openness of an erupting system, while also accounting for the capacity of the extruding magma to sustain a pressure gradient over the height of its column.

Timing

Under ideal circumstances, GPS data can be used to precisely resolve the timing of changes in deformation style. Of particular interest for the continuous phase of the 2006 Augustine eruption is the moment when inflation gave way to deflation, which would be useful for estimating magma-ascent rates. We reprocessed the available GPS data into subdaily solutions, using the RTD software (Bock and others, 2004) as above, but the small SNR of the deflationary signal made our efforts ineffective. We are simply unable to identify the precise time when deflation began. Our best estimate, based on both daily and subdaily solutions, is that it began within 12 hours of 1200 January 29, 2006 UTC.

Hiatus and Effusive Phases

By the time of the hiatus and effusive phase, the deformation signal had begun to diminish. This fact, in combination with the loss of the three close-in GPS receivers due to explosions, pyroclastic flows, and ballistics, makes interpretation of the deformation during these periods difficult. The vertical signal from stations AV01 and AV02 (fig. 2) with respect to station AC59 are plotted in figure 14. Stations AV01 and AV02 were the only ones to show a deformation signal during the hiatus and effusive phase. Although subsidence (deflation) associated with the continuous phase is the most conspicuous signal, we also see a hint of uplift (inflation) during the hiatus. A generous interpretation of these data also shows a small subsidence (deflation) concurrent with the effusive phase, but the purported signal is not statistically significant. Indeed, no

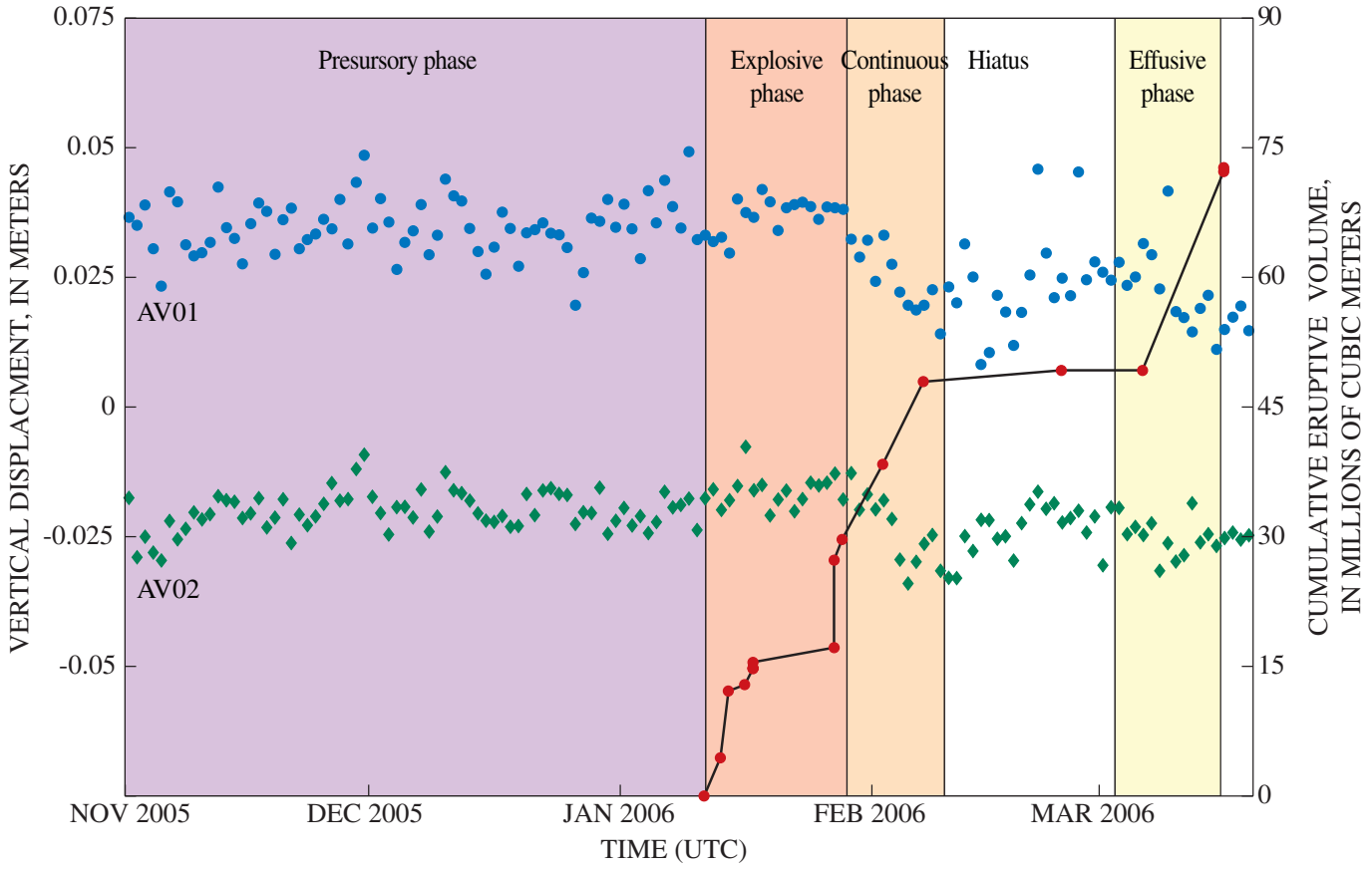


Figure 14. Long-term vertical time series from stations AV01 (top) and AV02 (bottom) with respect to AC59 (fig. 2). These close-in stations are the only two to have survived the course of the eruption intact. Cumulative eruptive volume from Coombs and others (this volume).

single velocity vector calculated from either the apparent hiatus uplift or effusive subsidence lies outside its error ellipse, although taken as whole, the deformation signal appears to slightly exceed the noise.

Modeling these data proved fruitless, although a few constraints on the dimensions and position of the magmatic sources operating over the hiatus and effusive phase can be imposed by the absence of an observed signal. A strong tradeoff exists, however, between source strength and depth that results in an insurmountable ambiguity. The same source that deflated during the continuous phase could have been repressurizing during the hiatus, although a weaker, shallower source is also consistent with the data. Another complicating factor, not considered so far, is the effect of viscoelastic relaxation of the hot material surrounding the subterranean magma. Newman and others (2006) showed that viscoelastic processes can have significant effects on observed deformation, although the short time scales characterizing the phases of the 2006 Augustine eruption probably minimized these effects.

Cumulative Deformation

The question of how much deformation remains after an eruption ends is important for several reasons. First, cumulative deformation is generally the only measurable variable of surface change, in the absence of a continuously recording network of geodetic instruments—a state of affairs characterizing nearly all of the world's volcanoes. Cumulative deformation also provides insight into volcanic processes occurring over the course of an eruption by providing at least partial answers to such questions as: (1) how does the overall shape of the edifice change during an eruption? (2) was there a net volume loss or gain to the edifice? (3) what proportion of the magma that passes through the shallow crust remains behind in comparison with the proportion that is erupted? and (4) what are the quantity, location, and orientation of the net stress change in the edifice after the eruption, and has the stress change contributed to flank instability? Finally, from a geodetic perspective, cumulative deformation amounts to a permanent record of an eruption. If the cumulative deformation is typically much smaller than, or even negligible relative to, coeruptive deformation, this difference will have important ramifications for the use of campaign versus continuous GPS stations for volcano monitoring and research.

To calculate cumulative deformation, we used both campaign and continuous GPS data, of which the campaign data consist of about a dozen bench marks on Augustine Island that were occupied in 2000 and then again after the eruption in summer 2006. Other bench marks exist that had been surveyed in 2000 but were not reoccupied in 2006, either because they could not be found or were inaccessible for logistical or safety reasons. Of interest is the net deformation that occurred over the course of the eruption. By necessity, we employ a proxy for this quantity consisting of the displacement from summer 2000 to summer 2006, subtracting out, to the extent possible, any nonvolcanic deformation (mainly plate motion) that occurred over this interval.

Ideally, a reference station would be located close enough to Augustine to undergo basiclly the same plate motion as the island but far enough away to be isolated from volcanic deformation. Several off-island stations meet this description (STEP, A18, AB22), but none of these stations were occupied throughout both the 2000 and 2006 campaigns. The reference station should be occupied simultaneously with other stations so that the subtraction needed to eliminate plate motion can be performed on each set of daily solutions. This procedure—differencing the daily solutions and then calculating the net displacement from the differences—is preferred over the converse because it (mostly) eliminates the effect of daily reference-frame errors. The only station occupied throughout both the 2000 and 2006 campaigns is A5, located on the northwest coast of Augustine Island (fig. 2). Because of its proximity to the volcano, this station would seem to be unsuitable for use as a reference station; however, calculating the average velocities between station A5 and the distal (15–20 km from Augustine) stations STEP and A18 over the 6-year interval in question reveals no motion distinguishable from zero. For this reason, we decided to use station A5 as a reference station in the following analysis.

The horizontal components of the permanent deformation that accumulated over the course of the 2006 Augustine eruption are mapped in figure 15. Though calculated over different intervals, the displacements from the campaign and continuous data should be comparable, assuming that little or no volcanic deformation occurred between summer 2000 and summer 2005. Lee and others (this volume) suggest island wide uplift from 1992 to 2005, but their results should have little effect on our analysis here because we focused on the intra island deformation gradients rather than the absolute deformation field.

The cumulative deformation at Augustine Volcano is plotted as a function of distance from the summit in figure 16. The horizontal component of the deformation, which is calculated by determining taking the magnitude of the east and north components of the displacement vector, should not be confused with the "radial" data plotted in figure 9, where the component of deformation is determined in the direction from individual stations to Augustine's summit.

Figures 15 and 16 show that the horizontal signal decays rapidly away from the summit, reaching zero by about 2.5-km distance. The vertical signal is negligible in comparison with the uncertainties in the data. Thus, in spite of the fact that three stations (A1, AV01, AV02, fig.2) show a statistically significant drop, we have little confidence of any overall vertical trend, although a slight tendency toward subsidence may exist.

The overall pattern of cumulative deformation resists straightforward modeling efforts. The large displacements close to the summit and the quick decay to zero suggest a shallow source of volumetric increase near the top of the edifice. We suspect that during the effusive phase of March 2006, the construction of a lava dome at the top of the edifice resulted in a permanent dilation of the magma conduit, along with the

accumulation of a small amount of new eruptive material there. If so, we would expect some vertical signal (uplift) as well. However, the loading effect of the new lava dome would result in subsidence and potentially cancel or attenuate the uplift predicted by a dilated conduit. Modeling the expected deformation signal from the new lava dome would entail a fairly involved analysis, taking full account of the edifice topography and the shape and extent of the dome. A finite-element approach seems feasible and is an avenue for future research.

Regarding the question of stress changes within the edifice, we can speculate about a few possible consequences of the cumulative deformation. We are confident that at least a small permanent change occurred in the internal volume of the edifice during the 2006 eruption. Depending on where the volume was added, the competency of the new material, and the change in slope induced by the addition, the strength of the edifice might have been subverted and potentially brought closer to failure. Given Augustine's history of repeated sector collapse (Begét and Kienle, 1992), we expect that a tendency toward instability is the norm and that, on average, each new eruption is more likely to weaken than strengthen the edifice. Reinforcing this notion is the absence of deformation at the more distal stations, which implies that the largest stress changes were concentrated within the steep upper slopes of the volcano. Moreover, the magnitude of the displacements around the circumference of the summit is larger at higher elevation

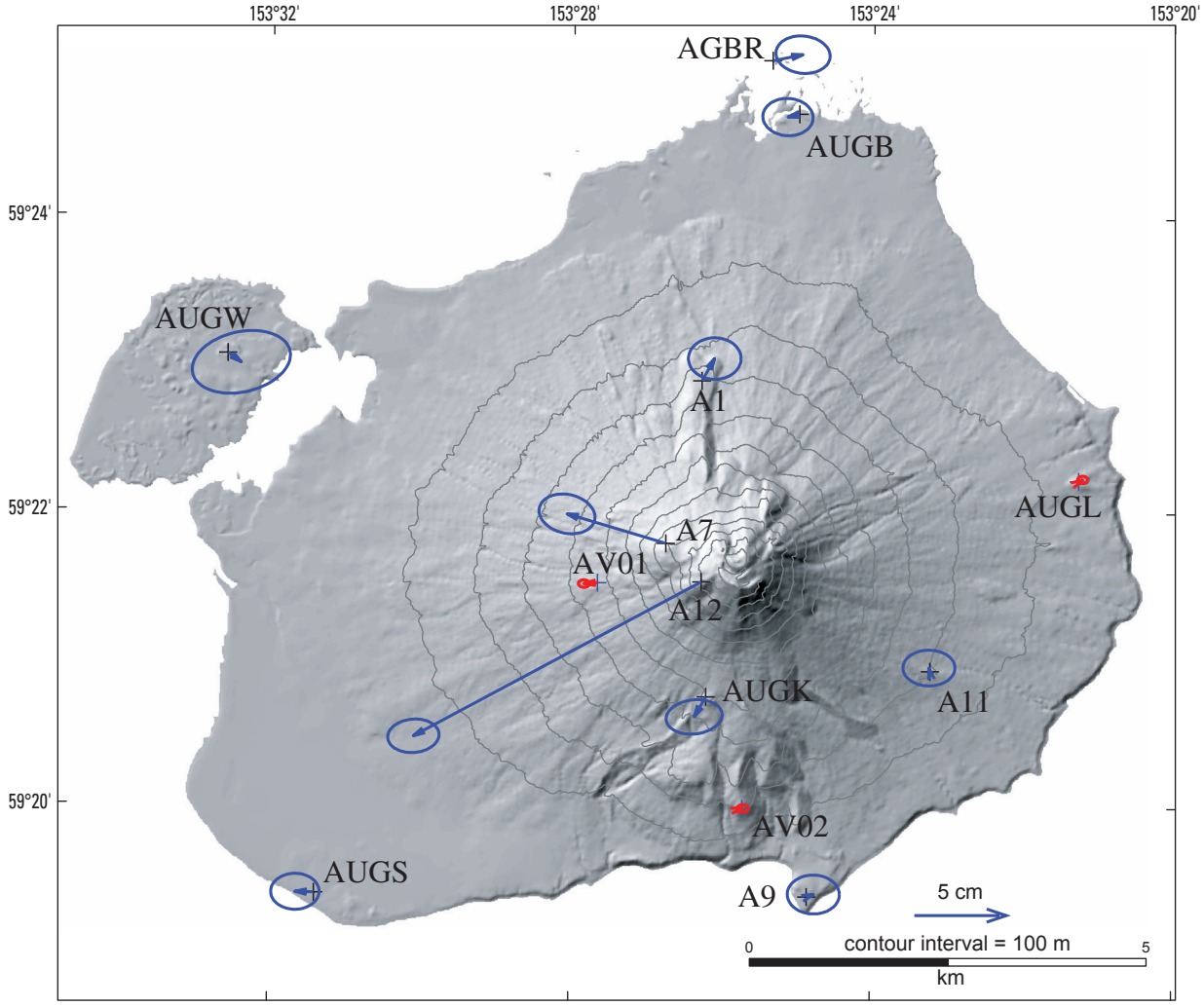


Figure 15. Augustine Volcano (fig.1), showing vectors of cumulative displacement from well before beginning of unrest to after eruption had decisively ended. Red, remaining intact Plate Boundary Observatory stations; blue, campaign bench marks. Only the four closest stations to Augustine's summit show significant deformation, with the maximum horizontal displacement at station A12 exceeding 20 cm.

(~20 cm at station A12, fig. 1) and declines downslope, also suggesting a trend toward steepening over time.

Discussion and Conclusions

Implications for Network Design

In our previous report on surface deformation at Augustine (Cervelli and others, 2006), we noted that the absence of evident precursory deformation at Mount St. Helens before its 2004–2008 eruption (Dzurisin and others, 2008; Lisowksi and others, 2008) prompted concern about whether continuous GPS was a useful monitoring tool on stratovolcanoes. We pointed out, however, that the only continuous GPS receiver operating immediately before the 2004 eruption was station JRO1, located approximately 8.5 km from the center of the crater. In contrast, the most distal Augustine GPS instrument, at station AUGL (fig. 2), was about half that distance from the summit. The total displacement at station AUGL during the precursory phase at Augustine was approximately 1 cm. If the depth of the source responsible for precursory pressurization was about 1.5 km (as we modeled it), then the corresponding displacement at a station 8.5 km laterally distant from the source (such as station JRO1 at Mount St. Helens) would be about 3 mm. Such displacement, emerging over 6 months, would be quite difficult to detect, especially without additional stations. What was needed before the 2004 Mount St. Helens eruption may well have been instrumentation and not signal. However, the magma composition at Mount St. Helens was much less gas rich than Augustine. Thus, at Mount St. Helens, little or no gas-driven precursory pressurization may have occurred, although at least some gas (mostly steam) was released in the initial explosion of the eruption on October 1, 2004 (Scott and others, 2008).

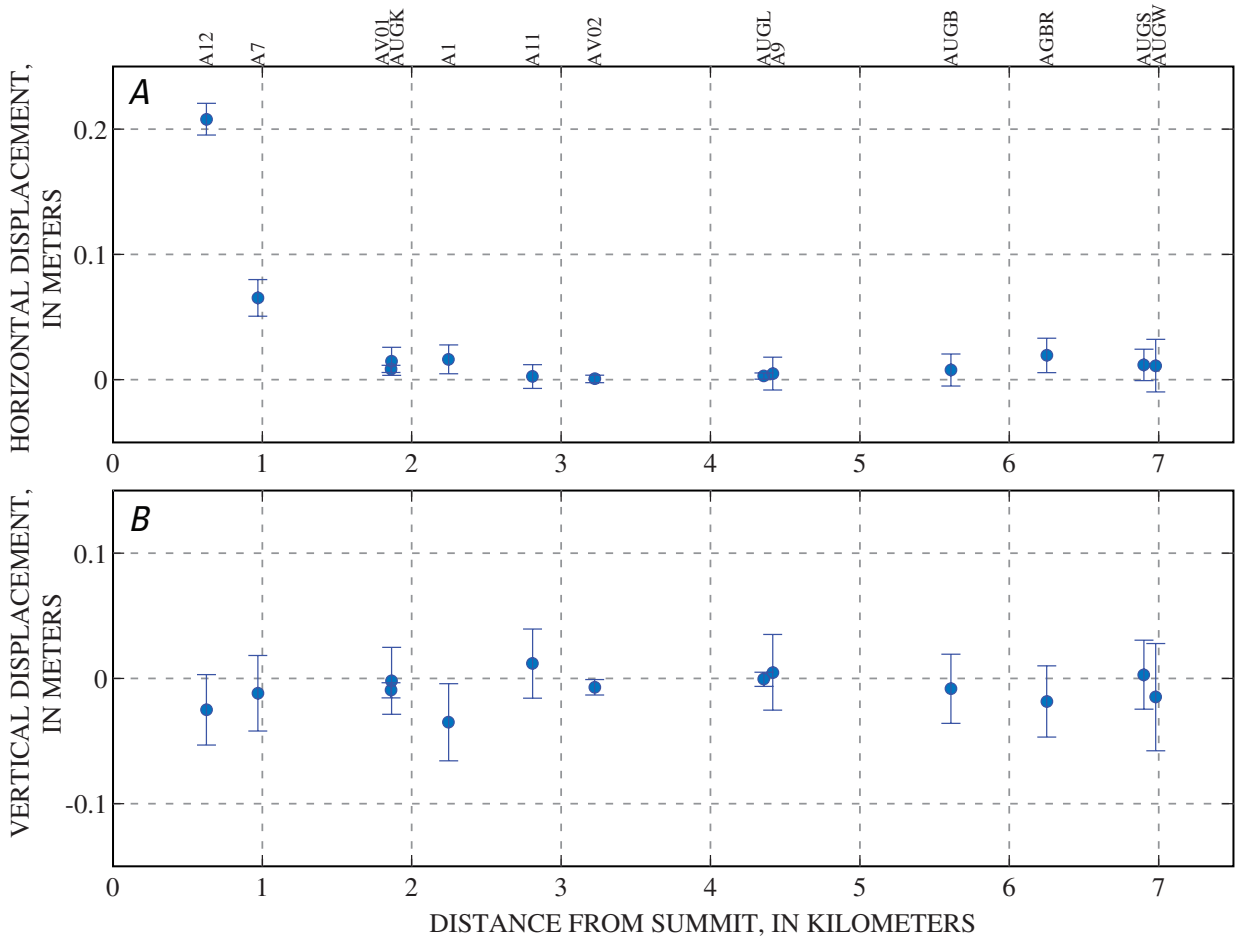


Figure 16. Horizontal (*A*) and vertical (*B*) sections of cumulative displacement over course of eruption 2006 of Augustine Volcano (fig. 1) as a function of distance from volcano's summit. Magnitude of horizontal displacement decreases drastically with distance, reaching zero about 2.5 km from summit. Vertical displacement is predominantly downward, although few individual measurements are statistically distinguishable from zero.

From the perspective of continuous GPS network design on stratovolcanoes, the main lesson of the 2006 Augustine eruption—especially in comparison with the 2004 Mount St. Helens eruption—is that close-in stations (<2 km from the summit) are extremely desirable for both volcano monitoring and research purposes. Installing stations this close to the summit presents many challenges, including steep slopes, friable rock, snow and ice at high latitudes, longer telemetry paths, and permitting issues; however, these challenges were overcome by UNAVCO (Pauk and others, this volume), and their efforts proved worthwhile. In addition to installation challenges, close-in stations are also prone to damage or destruction at even the earliest stages of precursory unrest; for example, several seismic stations became inoperable because of relatively minor phreatic explosions in early December 2005, and three GPS stations were lost in the initial explosive phase of the eruption. Mitigation strategies against station loss can take the form of hardened and (or) redundant installations. Neither strategy is likely to be completely effective, however, and both are expensive. The unavoidable fact is that the most interesting and important signals are commonly obtained in dangerous and inconvenient places. As volcanologists, we must accept this fact and explicitly acknowledge that a working instrument at risk of destruction is far more useful, and indeed, cost-effective than its undeployed counterpart resting safely on a shelf.

Because the cumulative, permanent deformation that accrued over the course of the eruption was concentrated quite close to (~2.5 km) the summit, in the absence of close-in bench marks the 2006 eruption would have been nearly invisible to campaign GPS. This fact reinforces our conclusion above that close is better when it comes to comprehensively imaging the deformation that occurs during unrest at stratovolcanoes, whether for continuously recording instruments or the establishment and occupation of campaign bench marks.

Deformation during the 2006 Augustine eruption arose from multiple sources, and our efforts to interpret these sources have several implications for network design. Two of the deformation sources (the precursory inflation and the deflation during the continuous phase) were clearly characterized by a radially symmetric deformation pattern. Distinguishing among different source types and depths requires a good distribution of stations over a range of distances from the summit. The station distribution at Augustine during the 2006 eruption was adequate, although it initially was hampered by a lack of intermediate (~5 km)-distance stations, which made it difficult to constrain source depths, particularly for sources deeper than a few kilometers. We improved the station distribution by adding temporary instruments at campaign bench marks AUGB, AUGK, AUGS, A5, and A11 (fig. 2). After the destruction of the summit sites, our ability to discriminate different deformation sources was significantly impaired—inflection or sign changes in near-field deformation can be tell tale indicators of deformation-source type.

Length measurements across the summit of a volcano have been used for decades for volcano monitoring (for example, Lipman and others, 1981). Summit-crossing baselines are easy to calculate, relatively insensitive to reference-frame error, and readily interpretable. The station pair AV02/AV03 (fig.2) proved especially useful for this purpose and played an important role in forecasting volcanic hazard. During the 10-day lull between the explosions of mid-January and those on January 27, considerable uncertainty existed about whether the quiescence represented the end of the eruption or only a brief pause. Not only had seismicity declined, but gas measurements were also showing the lowest levels of SO_2 flux since mid-December 2005 (McGee and others, this volume). During the lull, however, the baseline between stations AV02 and AV03 continued to indicate slow, but unmistakable, extension, indicating continued pressurization of the magma system and leading us to conclude that the eruption was not over. Explosions resumed on January 27, 2006, and the continuous phase began shortly thereafter.

One of the main shortcomings of continuous GPS is its relative insensitivity to high-frequency signals, particularly when sub daily solutions are sought in near-real time. This deficiency was felt acutely during the 2006 Augustine eruption, and in retrospect several important signals were clearly missed, at least from the perspective of short-term monitoring. For example, the deformation associated with the energetic earthquake swarm preceding the initial explosions would have been useful for forecasting purposes, had it been recognized at the time. Even after-the-fact post processing can be insufficient to resolve the level of temporal detail required to constrain such variables as the rate of magma ascent or dome growth. For these reasons, we strongly advocate that geodetic instruments with higher temporal precision, such as tiltmeters, be a part of any stratovolcano research and monitoring network. Tiltmeters are in routine use at other volcanoes and have repeatedly proved their usefulness (for example, Eaton, 1959; Dvorak and Okamura, 1987; Cervelli and Miklius, 2003), but nonetheless, instruments of this type remain far less common than continuous GPS. Another advantage of tiltmeters is that they are generally installed a few meters beneath the surface, making them considerably more resistant to damage than delicate GPS antennas. Even if their exposed telemetry system is swept away, tiltmeter data can still be retrieved after the end of the eruption, provided that those data are logged in the instrument and not at the surface and that the instrument is not buried beneath thick new deposits.

Summary

We have analyzed the geodetic data associated with the 2006 eruption of Augustine Volcano. Our main results are summarized as follows: (1) Deformation during the precursory phase of the eruption consisted of shallow (approx. sea level) inflation, probably attributable to volatile pressurization at the impermeable base of the edifice. The negligible volume change calculated during this phase, along with petrologic depth constraints, indicates that this source was

not the primary magma body. (2) In the 60 days preceding the eruption, a dike probably propagated into the edifice, nearly reaching the surface by early January 2006. Evidence for this dike includes a characteristic, easily modeled geodetic signal, consistency with petrologic analysis, and large phreatic explosions on January 11, 2006. (3) In the 2 days before the explosions of January 13, 2006—the first explosions with a clearly juvenile product—the summit deformed rapidly, probably in response to the final ascent of the dike, followed by the initiation of dome growth. (4) During the eruption hiatus between January 17 and January 27, 2006, the edifice continued to inflate, suggesting that magma pressurization continued over this interval and that, from a hazard-forecasting perspective, the eruption was not over. (5) Beginning around January 29, 2006, deformation at Augustine abruptly switched from inflation to deflation. We interpret this deflation as partial draining of the primary magma reservoir, which we model as a cylindrical body starting from a top depth of 2.5 to 4.5 km below Augustine's summit and extending to between 6.5 to 10.5 km at its bottom. This model is consistent with petrologic analysis and earthquake locations. (6) After the end of the effusive phase, declining geodetic signal strength, in combination with the attrition of the GPS network, made quantitative interpretation difficult. Nonetheless, we argue that the geodetic data show a small inflation following the effusive phase, which gradually changes to deflation immediately before the dome building and lava flows of March 2006. Finally, (7) the total accumulated deformation over the course of the eruption is restricted to within about 2.5 km of the volcano's summit, although within this region the deformation is large and spatially coherent. This observation implies the permanent emplacement of new volume within the edifice. However, the absence of a cumulative deformation signal beyond the 2.5-km radius implies almost total recovery of the volume lost from the midcrustal chamber during the continuous and effusive phases. These implications suggest a magmatic system that over years to decades is relatively open from the lower crust to midcrust upward, but that closes at the summit after eruptions.

Acknowledgments

We thank the National Science Foundation's PBO and UNAVCO for constructing, maintaining, and operating the continuous GPS network on Augustine Volcano. USGS reviewers Larry Mastin and Michael Poland provided careful, thorough, and thoughtful reviews of the manuscript. We also thank David Schneider, Max Kaufmann, and Cyrus Read for their help in setting out and retrieving the campaign GPS sites. John Paskievitch, Guy Tytgat, Ed Clark, Tom Parker, Tim Plucinski, and Cyrus Read contributed considerable effort to keep the geophysical networks at Augustine running throughout the eruption. Finally, we are grateful to Michelle Coombs for her encouragement and patience while we were writing this manuscript.

References Cited

Anderson, E.M., 1936, Dynamics of the formation of cone-sheets, ring-dykes, and cauldron-subsidences: Royal Society of Edinburgh Proceedings, no. 56, p. 128–157.

Begét, J.E., and Kienle, J., 1992, Cyclic formation of debris avalanches at Mount St. Augustine volcano: Nature, v. 356, no. 6371, p. 701–704.

Bock, Y., Macdonald, T., Merts, J., Bock, L, and Fayman, J., 2004, Epoch-by-Epoch™ real-time GPS positioning in high dynamics and at extended ranges: ITEA Journal of Test and Evaluation, v. 25, no. 3, p. 37–45.

Bonaccorso, A., and Davis, P.M., 1999, Models of ground deformation from vertical volcanic conduits with application to eruptions of Mount St. Helens and Mount Etna: Journal of Geophysical Research, v. 104, p. 1053–10542.

Cervelli, P.F., and Miklius, A., 2003, The shallow magmatic system of Kilauea Volcano, *in* Heliker, C., Swanson, D.A., and Takahashi, T.J., eds., The Pu'u 'O'o-Kūpaianaha eruption of Kilauea Volcano, Hawai'i: U.S. Geological Survey Professional Paper 1676, p. 149–164.

Cervelli, P.F., Fournier, T., Freymueller, J.T., and Power, J.A., 2006, Ground deformation associated with the precursory unrest and early phases of the January 2006 eruption of Augustine Volcano, Alaska: Geophysical Research Letters, v. 33, 5 p., doi:10.1027/2006GL027219.

Cervelli, P.F., Murray, M.H., Segall, P., Aoki, Y., and Kato, T., 2001, Estimating source parameters from deformation data, with an application to the March 1997 earthquake swarm off the Izu Peninsula, Japan: Journal of Geophysical Research v. 106, no. B6, p. 11217–11237.

Coombs, M.L., Bull, K.F., Vallance, J.W., Schneider, D.J., Thoms, E.E., Wessels, R.L., and McGimsey, R.G., 2010, Timing, distribution, and volume of proximal products of the 2006 eruption of Augustine Volcano, *in* Power, J.A., Coombs, M.L., and Freymueller, J.T., eds., The 2006 eruption of Augustine Volcano, Alaska: U.S. Geological Survey Professional Paper 1769 (this volume).

Dvorak, J.J. and Okamura, A.T., 1987, A hydraulic model to explain variations in summit tilt rate at Kilauea and Mauna Loa volcanoes, *in* Decker, R.W., Wright, T.L., and Stauffer, P.H., eds., Volcanism in Hawaii: U.S. Geological Survey Professional Paper 1350, p. 1281–1296.

Dzurisin, D., Lisowski, M., Poland, M.P., Sherrod, D.R., and LaHusen, R.G., 2008, Constraints and conundrums resulting from ground-deformation measurements made during the 2004–2005 dome-building eruption of Mount St. Helens, Washington, chap. 14 *of* Sherrod, D.R., Scott, W.E., and Stauffer, P.H., eds., A volcano rekindled; the renewed eruption of Mount

St. Helens, 2004–2006: U.S. Geological Survey Professional Paper 1750, p. 281–300.

Eaton, J.P., 1959, A portable water-tube tiltmeter: Seismological Society of America Bulletin, v. 49, p. 177–206.

Gerlach, T.M., McGee, K.A., and Doukas, M.P., 2008, Emission rates of CO_2, SO_2, and H_2S, scrubbing, and preeruption excess volatiles at Mount St. Helens, 2004–2005, chap. 26 in Sherrod, D.R., Scott, W.E., and Stauffer, P.H., eds., A volcano rekindled; the renewed eruption of Mount St. Helens, 2004–2006: U.S. Geological Survey Professional Paper 1750, 543–571.

Larsen, J.F., Nye, C.J., Coombs, M.L., Tilman, M., Izbekov, P., and Cameron, C., 2010, Petrology and geochemistry of the 2006 eruption of Augustine Volcano, *in* Power, J.A., Coombs, M.L., and Freymueller, J.T., eds., The 2006 eruption of Augustine Volcano, Alaska: U.S. Geological Survey Professional Paper 1769 (this volume).

Lee, C.-W., Lu, Z., Jung, H.-S., Won, J.-S., and Dzurisin, D., 2010, Surface deformation of Augustine Volcano, 1992–2005, from multiple-interferogram processing using a refined small baseline subset (SBAS) interferometric synthetic aperture radar (InSAR) approach, in Power, J.A., Coombs, M.L., and Freymueller, J.T., eds., The 2006 eruption of Augustine Volcano, Alaska: U.S. Geological Survey Professional Paper 1769 (this volume).

Lipman, P.W., Moore, J.G., and Swanson, D.A., 1981, Bulging of the north flank before the May 18 eruption—geodetic data, *in* Lipman, P.W., and Mullineaux, eds., The 1980 eruptions of Mount St. Helens, Washington: U.S. Geological Survey Professional Paper 1250, p. 143–156.

Lisowski, M., Dzurisin, D., Denlinger, R.P., and Iwatsubo, E.Y., 2008, Analysis of GPS-measured deformation associated with the 2004–2006 dome-building eruption of Mount St. Helens, Washington, chap. 15 *of* Sherrod, D.R., Scott, W.E., and Stauffer, P.H., eds., A volcano rekindled; the renewed eruption of Mount St. Helens, 2004–2006: U.S. Geological Survey Professional Paper 1750, p. 301–333.

Mastin, L.G., Roeloffs, E., Beeler, N.M., and Quick, J.E., 2008, Constraints on the size, overpressure, and volatile content of the Mount St. Helens magma system from geodetic and dome-growth measurements during the 2004–2006 eruption, chap. 22 of Sherrod, D.R., Scott, W.E., and Stauffer, P.H., eds., A Volcano Rekindled; the renewed eruption of Mount St. Helens, 2004–2006. U.S. Geological Survey Professional Paper 1750, p. 461–492.

McGee, K.A., Doukas, M.P., McGimsey, R.G., Neal, C.A., and Wessels, R.L., 2010, Emission of SO_2, CO_2, and H_2S from Augustine Volcano, 1995–2006, in Power, J.A., Coombs, M.L., and Freymueller, J.T., eds., The 2006 eruption of Augustine Volcano, Alaska: U.S. Geological Survey Professional Paper 1769 (this volume).

McLean, H., 1979, Sandstone petrology; Upper Jurassic Naknek Formation of the Alaska Peninsula and coeval rocks on the Bering Shelf: Journal of Sedimentary Petrology, v. 49, p. 1263–1267.

Mogi, K., 1958, Relations between the eruptions of various volcanoes and the deformations of the ground surfaces around them: Univerity of Tokyo, Earthquake Research Institute Bulletin, v. 36, p. 111–123.

Moran, S.C., Malone, SD., Qamar, A.I., Thelen, W., Wright, A.K.,and Caplan-Auerbach, J., 2008, Seismicity associated with renewed dome-building at Mount St. Helens, 2004–2005, in Sherrod, D.R., Scott, W.E., and Stauffer, P.H., eds, A volcano rekindled; the renewed eruption of Mount St. Helens, 2004–2006: U.S. Geological Survey Professional Paper 1750, p. 27–60.

Neal, C.A., Murray, T.L., Power, J.A, Adleman, J.N., Whitmore, P.M., and Osiensky, J.M., 2010, Hazard information management, interagency coordination, and impacts of the 2005–2006 eruption of Augustine Volcano, *in* Power, J.A., Coombs, M.L., and Freymueller, J.T., eds., The 2006 eruption of Augustine Volcano, Alaska: U.S. Geological Survey Professional Paper 1769 (this volume).

Newman, A.V., Dixon, T.H., and Gourmelen, N., 2006, A four-dimensional viscoelastic deformation model for Long Valley Caldera, California, between 1995 and 2005: Journal of Volcanology and Geothermal Research, v. 150, p. 244–269.

Niell, A.E., 1996, Global mapping functions for the atmosphere delay at radio wavelengths: Journal of Geophysical Research v. 101, no. B2, p. 3227–3246.

Okada, Y., 1985, Surface deformation due to shear and tensile faults in a half-space: Seismological Society of America Bulletin, v. 75, p. 1135–1154.

Owen, S., Segall, P., Lisowski, M., Miklius, A., Murray, M., Bevis, M., and Foster, J., 2000, The January 30, 1997 eruptive event on Kilauea Volcano, Hawaii, as monitored by continuous GPS: Journal of Geophysical Research, v. 27, no. 17, p. 2757–2760.

Pauk, B.A., Power, J.A., Lisowski, M., Dzurisin, D., Iwatsubo, E.Y., and Melbourne, T., 2001, Global Positioning System (GPS) survey of Augustine Volcano, Alaska, August 3–8, 2000; data processing, geodetic coordinates and comparison with prior geodetic surveys: U.S. Geological Survey Open-File Report 01-0099, 20 p.

Pauk, B.A., Jackson, M., Feaux, K., Mencin, D., and Bohnenstiehl, K., 2010, The Plate Boundary Observatory permanent global positioning system network on Augustine Volcano before and after the 2006 eruption, *in* Power, J.A., Coombs, M.L., and Freymueller, J.T., eds., The 2006 eruption of Augustine Volcano, Alaska: U.S. Geological Survey Professional Paper 1769 (this volume).

Power, J.A., and Iwatsubo, E.Y. 1998, Measurements of slope distances and zenith angles at Augustine Volcano, Alaska, 1986, 1988, and 1989: U.S. Geological Survey Open-File Report 98-0145, 17 p.

Power, J.A., and Lalla, D.J., 2010, Seismic observations of Augustine Volcano, 1970–2007, *in* Power, J.A., Coombs, M.L., and Freymueller, J.T., eds., The 2006 eruption of Augustine Volcano, Alaska: U.S. Geological Survey Professional Paper 1769 (this volume).

Roman, D.C., Cashman, K.V., Gardner, C.A., Wallace, P., and Donovan, J., 2005, Storage and interaction of compositionally heterogeneous magmas from the 1986 eruption of Augustine Volcano, Alaska: Bulletin of Volcanology, v. 68, p. 240–254.

Scott, W.E., Sherrod, D.R., and Gardner, C.A., 2008, Overview of the 2004 to 2006, and continuing, eruption of Mount St. Helens, Washington, chap. 1 *of* Sherrod, D.R., Scott, W.E., and Stauffer, P.H., eds., A volcano rekindled; the renewed eruption of Mount St. Helens, 2004–2006: U.S. Geological Survey Professional Paper 1750, p. 3–26.

Segall, P., 2010, Earthquake and Volcano Deformation, Princeton, N.J., Princeton University Press, 458 p.

Tappen, C.M., Webster, J.D., Mandeville, C.W., and Roderick, D., 2009, Petrology and geochemistry of ca. 2100–1000 a.B.P. magmas of Augustine volcano, Alaska, based on analysis of prehistoric pumiceuous tephra: Journal of Volcanology and Geothermal Research, v. 183, p. 42–62.

Wallace, K.L., Neal, C.A., and McGimsey, R.G., 2010, Timing, distribution, and character of tephra fall from the 2005–2006 eruption of Augustine Volcano, *in* Power, J.A., Coombs, M.L., and Freymueller, J.T., eds., The 2006 eruption of Augustine Volcano, Alaska: U.S. Geological Survey Professional Paper 1769 (this volume).

Webster, J.D., Mandeville, C.W., Goldoff, B., Coombs, M.L., and Tappen, C., 2010, Augustine Volcano—The influence of volatile components in magmas erupted A.D. 2006 to 2,100 years before present, *in* Power, J.A., Coombs, M.L., and Freymueller, J.T., eds., The 2006 eruption of Augustine Volcano, Alaska: U.S. Geological Survey Professional Paper 1769 (this volume).

Wessels, R.L., Coombs, M.L., Schneider, D.J., Dehn, J., and Ramsey, M.S., 2010, High-resolution satellite and airborne thermal infrared imaging of the 2006 eruption of Augustine Volcano, in Power, J.A., Coombs, M.L., and Freymueller, J.T., eds., The 2006 eruption of Augustine Volcano, Alaska: U.S. Geological Survey Professional Paper 1769 (this volume).

Williams, C.A., and Wadge, G., 1998, The effects of topography on magma chamber deformation models; application to Mt. Etna and radar interferometry: Geophysical Research Letters, v. 25, p. 1549–1552.

Yang, X., Davis, P.M., and Dieterich, J.H., 1988, Deformation from inflation of a dipping finite prolate spheroid in an elastic half-space as a model for volcanic stressing: Journal of Geophysical Research, v. 93, no. B5, p. 4249–4258.

Zumberge, J.F., Heflin, M.B., Jefferson, D.C., Watkins, M.M., and Webb, F.H., 1997, Precise point positioning for the efficient and robust analysis of GPS data from large networks: Journal of Geophysical Research, v. 102, no. B3, p. 5005–5017.

The 2006 Eruption of Augustine Volcano, Alaska
Power, J.A., Coombs, M.L., and Freymueller, J.T., editors
U.S. Geological Survey Professional Paper 1769

Chapter 18

Surface Deformation of Augustine Volcano, 1992–2005, from Multiple-Interferogram Processing Using a Refined Small Baseline Subset (SBAS) Interferometric Synthetic Aperture Radar (InSAR) Approach

By Chang-Wook Lee[1], Zhong Lu[2], Hyung-Sup Jung[3], Joong-Sun Won[4], and Daniel Dzurisin[5]

Abstract

Augustine Volcano is an active stratovolcano located in southwestern Cook Inlet, about 280 kilometers southwest of Anchorage, Alaska. The volcano produced six significant explosive eruptions between 1812 and 1986. Augustine eruptions typically have an explosive onset followed by dome building. The most recent eruption began on January 11, 2006. We applied the small baseline subset (SBAS) interferometric synthetic aperture radar (InSAR) technique to measure ground surface deformation during 1992–2005 with the use of European Remote Sensing Satellites 1 and 2 (ERS–1 and ERS–2) radar imagery. Through a multiple-interferogram approach, atmospheric delay artifacts, which hinder conventional InSAR measurements, are significantly reduced by spatial and temporal filtering. This allows us to retrieve time-series deformation over coherent points at millimeter-scale accuracy. The deformation results from two independent satellite tracks agree with each other, suggesting 2 to 8 cm wholesale uplift of Augustine Volcano from 1992 to 2005. Global Positioning System (GPS) data acquired in September 2004 and October 2005 confirm the SBAS InSAR results. A preliminary model consisting of a contracting source at 2 to 4 km depth and an inflating source at 7 to 12 km depth fits the observed deformation reasonably well. We interpret the deeper source as a long-term magma storage zone and the shallower source as a subsidiary reservoir that was tapped during the 2006 eruption. The shallow source corresponds approximately to the location of the volcano-tectonic earthquakes that preceded and followed the 1976 and 2006 eruptions, respectively.

Introduction

Mapping volcanic deformation between eruptions can provide important clues to the magma plumbing system and magma supply rate (Dzurisin, 2007). Ground-based techniques, including Global Positioning System (GPS) observations, leveling, and tiltmeters, can measure subtle deformation with an accuracy of a few millimeters. Even though these ground-based techniques can provide accurate point-to-point deformation measurements, they are relatively expensive, logistically challenging, and often inadequate to characterize complex deformation patterns that sometimes are associated with eruptions (Dzurisin, 2007). Interferometric synthetic aperture radar (InSAR) is a satellite-based technique for mapping large-area surface deformation. InSAR has become an important tool for studying volcanoes in Alaska (Lu and others, 2007) and around the world (Zebker and others, 2000). In theory, InSAR can measure relative surface displacements with an accuracy of a few millimeters (Gabriel and others, 1989). In reality, however, atmospheric delay noise and other

[1]ASRC Research and Technology Solutions, contractor to USGS, 1300 SE Cardinal Court, Vancouver, WA 98683.

[2]U.S. Geological Survey, EROS Center and Cascades Volcano Observatory, 1300 SE Cardinal Court, Vancouver, WA 98683-9589.

[3]Department of Geoinfomatics, The University of Seoul, 90 Jeonnong-dong, Dongdaemun-gu, Seoul 130-743, Korea.

[4]Department of Earth System Sciences, Yonsei University, 134 Shinchon-dong, Seodaemun-gu, Seoul, 120-749, Korea.

[5]U.S. Geological Survey, Cascades Volcano Observatory, 1300 SE Cardinal Court, Vancouver, WA 98683-9589.

artifacts reduce the accuracy obtainable with InSAR to a few centimeters (Zebker and others, 1997).

Geodetic measurements began at Augustine Volcano starting in 1986 (Power and Iwatsubo, 1998), and GPS campaign surveys were conducted repeatedly in the early 1990s and in 2000 (Pauk and others, 2001). An initial analysis did not detect any surface deformation that could be attributed to magmatic activity for the period from 1988 to 2000 (Pauk and others, 2001). The campaign GPS data were reprocessed in late 2005 (J. Freymueller, written commun., December 14, 2005). Results indicated that a shallow source (depth less than a few kilometers) beneath the volcano's summit might have deflated at a rate of less than 5 mm/yr during 1988–2000. Five continuous GPS (CGPS) stations were established in September 2004 by the EarthScope Plate Boundary Observatory (Pauk and others, this volume), and detected shallow inflation of about 2 mm/month from June 2005 to January 2006 before the 2006 eruption (Cervelli and others, 2006).

Early results based on a limited number of InSAR images indicated subsidence of 1986 pyroclastic flows on the north flank of Augustine Volcano (Lu and others, 2003). Masterlark and others (2006) constructed a finite element model that simulated post-eruptive thermoelastic contraction of the initially hot and geometrically complex 1986 pyroclastic flow deposits. By combining a 1992–1993 InSAR image, the finite element model, and an adaptive mesh algorithm to iteratively optimize the geometry of the deposit, Masterlark and others (2006) determined an initial excess temperature for the pyroclastic flow unit of 640ºC and an average thickness of 9.3 m. Lee and others (2008) systematically processed all the available InSAR images for Augustine Volcano acquired during 1992–2005 and concluded that (1) typical summer-to-summer InSAR images maintain good coherence for only about 2 years, probably because most of the volcano is mantled by pyroclastic flows and other loose materials that are easily erodible and compactable; (2) atmospheric delay anomalies typically reached 2 to 3 cm in individual interferograms; and (3) stacking multiple InSAR images revealed no significant, centimeter-scale volcano-wide deformation during 1992–2005.

The first obstacle that prevented us from reaching millimeter-scale accuracy for InSAR measurements at Augustine Volcano is atmospheric path-delay anomalies, which are caused mainly by variation in the water vapor content of the atmosphere. Studies have shown that the apparent range change caused by atmospheric delays over Augustine (Lee and others, 2008) and other Aleutian volcanoes (Lu and others, 2007) can be as large as 10 cm. Averaging multiple InSAR images tends to reduce atmospheric noise, because water vapor patterns generally are not spatially correlated over time intervals spanned by interferograms. Nevertheless, the effectiveness of InSAR for monitoring Aleutian volcanoes has been hampered by the typical presence of large atmospheric path-delay anomalies, and theoretical accuracy of 2 to 3 mm for InSAR has not been achieved. A second factor affecting InSAR measurement at Augustine is the loss of InSAR coherence for InSAR images that span more than 2 years. This is because much of the volcano is covered by pyroclastic flows that do not maintain good coherence for C-band InSAR measurements.

Two techniques have been proposed to conduct time-series analysis of multiple interferograms to reduce atmospheric noise: (1) persistent scatterer InSAR (PSInSAR) (Ferretti and others, 2001) and (2) small baseline subset (SBAS) InSAR (Berardino and others, 2002). For PSInSAR, a single master image is used to construct all the interferograms for time-series analysis. This approach did not yield useful results for Augustine Volcano, owing to the problem with coherence loss that was mentioned previously. Instead, we used SBAS InSAR, which utilizes several master images to form interferograms with small baselines that span relatively short time intervals (and therefore tend to maintain coherence).

For this paper, we used all suitable SAR images of Augustine Volcano that were acquired from 1992 to 2005. Our objective was to detect and measure any subtle, small-scale deformation that might have occurred during the time of our investigation. We used SAR data from two independent satellite tracks to intercompare InSAR-derived deformation measurements. In addition, we compared InSAR measurements with continuous GPS measurements for the period September 2004 to October 2005. Finally, we used a two-source model to interpret the observed deformation pattern.

Historical Eruption of Augustine Volcano

Augustine Volcano is a 1,260-m-high and 90-km^2 island stratovolcano in the southwestern part of Cook Inlet, about 280 km southwest of Anchorage, Alaska (fig. 1). Augustine Island formed on Jurassic and Cretaceous sedimentary strata overlain by granitoid glacial erratics and volcanic hyaloclastites (Miller and others, 1998). Augustine Volcano is one of the youngest and most active volcanoes in Cook Inlet (Begét and Kowalik, 2006), with explosive eruptions in 1812, 1883, 1935, 1963, 1976, 1986, and most recently 2006. The most violent of these eruptions was in 1883, when a debris avalanche generated a small tsunami in Cook Inlet (Miller and others, 1998). This tsunami struck the eastern and western coasts of the southern part of Cook Inlet with 6 to 8 m waves (Begét and Kowalik, 2006). Ash clouds from the 1976 eruption were observed in eastern North America and drifted across the Atlantic Ocean (Kienle and Shaw, 1979). Most eruptions of Augustine began with an initial series of vent-clearing explosions with pyroclastic flows, surges, and lahars on the volcano flanks, followed by the extrusion of andesitic lava from the volcano's summit (Waythomas and Waitt, 1998). Proximal eruption hazards include pyroclastic flows and surges, debris avalanches, lahars, ballistics, and ash fallout. Tsunamis generated by debris avalanches can reach the Alaska mainland. Volcanic ash that can drift great distances poses a threat to airliners and to people with respiratory problems (Waythomas and Waitt, 1998).

InSAR Analysis

Data and Preprocessing

For our analysis, we chose SAR data that were acquired from two adjacent tracks by European Remote Sensing Satellites 1 and 2 (ERS–1 and ERS–2). From 1992 to 2005, there were 27 and 25 descending scenes acquired from tracks 229 and 501, respectively. To apply the SBAS InSAR algorithm, 25 and 27 InSAR images with perpendicular baselines of less than about 300 m were created. These were distributed in five and four small-baseline subsets as shown in figures 2*A* and 2*B*, respectively. As a result of the difference in satellite positions, SAR images between adjacent tracks cannot be combined to form interferograms. All the interferograms were obtained by using a complex multilook operation, with 2 looks in the range direction and 10 looks in the azimuth direction, resulting in a pixel dimension of about 40 m by 40 m. Topographic phase contributions in the original interferograms were removed by using the 1-arc-second Shuttle Radar Topography Mission (SRTM) digital elevation model (DEM; Farr and others, 2007).

Introduction to the SBAS InSAR Algorithm

The SBAS InSAR algorithm was recently proposed and demonstrated by Berardino and others (2002) as a means to mitigate atmospheric artifacts and topographic errors in time-sequential interferograms, and thus to obtain time-series deformation information. The algorithm uses only interferograms with small baselines that overlap in time in order to reduce spatial decorrelation.

The phase ($\Delta\phi$) of each interferogram is defined by

$$\Delta\phi(x,r) \approx \frac{4\pi}{\lambda}\Delta d(x,r) + \frac{4\pi}{\lambda}\frac{B_{\perp}}{r\sin\theta}\Delta z(x,r) + \Delta\phi_{atmo}(x,r) + \Delta\phi_{n}(x,r), \quad (1)$$

where x and r are the azimuth and slant-range pixel coordinates, λ is the radar wavelength, Δd is the surface displacement in the radar look direction, $B_{\perp}$ is the perpendicular baseline, θ is the SAR look angle, Δz is the topographic error, $\Delta\phi_{atmo}$ is the atmospheric phase-delay artifact, and $\Delta\phi_{n}$ is the phase due to other noise sources (Berardino and others, 2002).

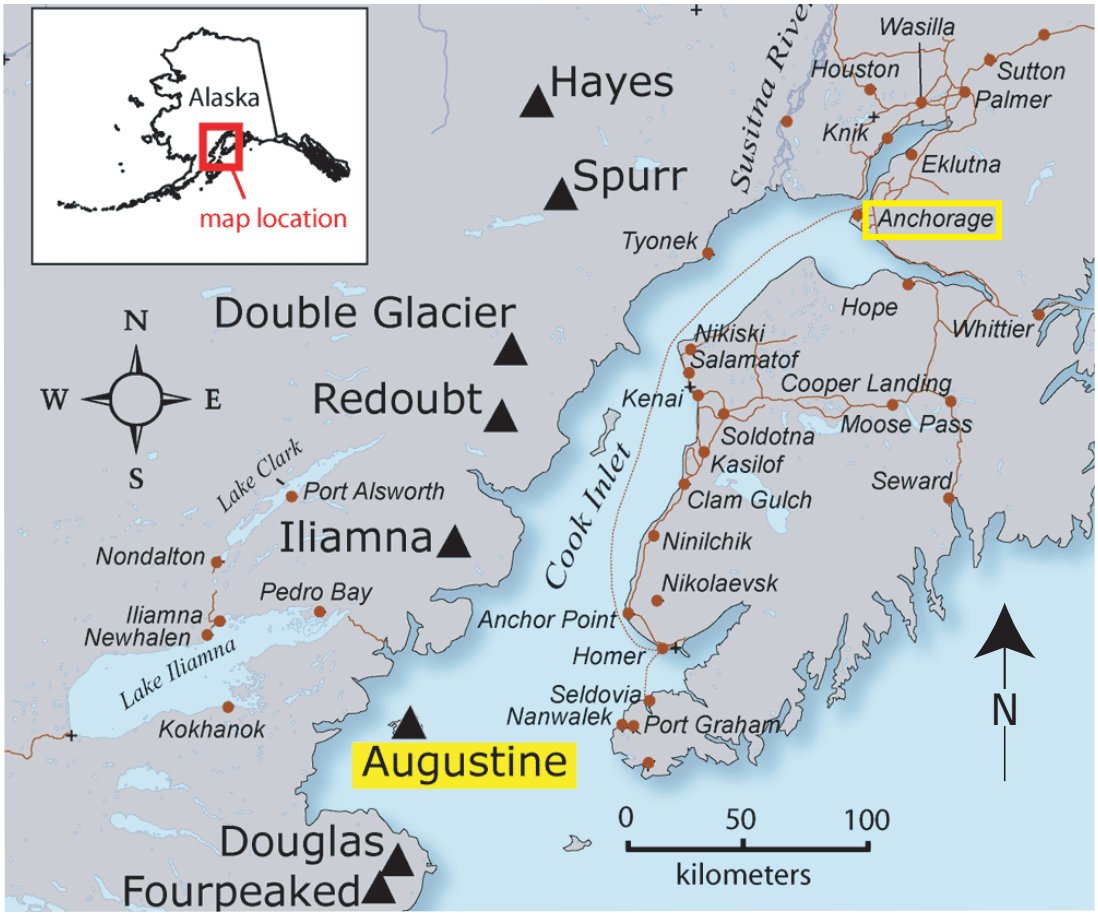


Figure 1. Location of Augustine Island in the southwestern part of Cook Inlet, Alaska. Triangles, volcanoes.

To achieve deformation time-series information from multiple interferograms, the SBAS algorithm estimates the mean deformation rate and the topographic error. The atmospheric artifacts are mitigated through temporal high-pass and spatial low-pass filtering of interferograms after the mean deformation rates have been removed. Because the interferograms are not adjacently linked (there may be temporal overlap or underlap between them), SBAS InSAR uses the singular value decomposition (SVD) approach based on a minimum-norm criterion of the deformation rate to derive time-series deformation measurements.

Although this algorithm is very effective for measuring time-series deformation, the suppression of errors caused by temporal decorrelation and other noise effects is not properly addressed. Linear deformation rates estimated by using interferograms having unwrapping errors commonly lead to misestimates of the actual deformation history. Estimates of atmospheric artifacts and topographic errors based on the assumption of linear deformation rate during the periods spanned by individual interferograms can further detract from the retrieval of accurate time-series deformation measurements. Moreover, the atmospheric artifact and orbital error at the reference point (a pixel location used to reference interferogram phase values at other pixels) have not been properly addressed, which can affect the deformation measurements.

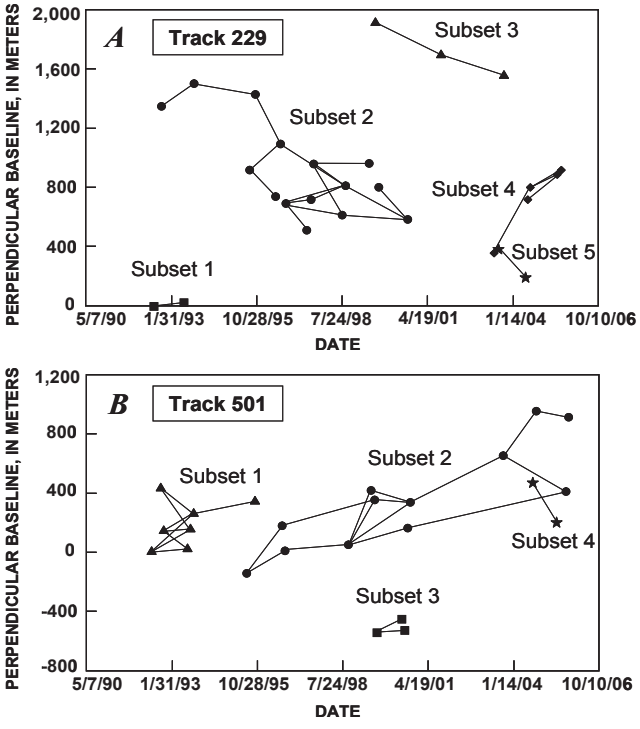


Figure 2. Perpendicular baselines used for small baseline subset (SBAS) interferometric synthetic aperture radar (InSAR) processing at Augustine Volcano, Alaska. *A,* Five different small baseline subsets from satellite track 229 were used for SBAS InSAR processing. *B,* Four different small baseline subsets from satellite track 501 were used for SBAS InSAR processing.

Refined SBAS InSAR Processing

Our refined SBAS InSAR algorithm improves estimates of time-series deformation in four respects. First, we correct phase unwrapping errors by distinguishing between high-quality (HQ) images in which no unwrapping errors could be found and low-quality (LQ) ones where phase jumps due to unwrapping errors are obvious. Second, we refine estimates of atmospheric artifacts, topographic errors, and time-series deformation measurements through an iteration procedure. Third, we further mitigate the temporal noise by the finite difference smoothing approach (Schmidt and Burgmann, 2003). Finally, we implement procedures to correct any possible phase bias at the reference point due to orbital and atmospheric phase artifacts. Specifically, the reference phase correction is based on the assumption that the mean of the unwrapped residual interferogram is approximately zero as given by

$$\frac{1}{N_{az}\,N_{rg}}\sum_{i=1}^{N_{az}}\sum_{j=1}^{N_{rg}}\left[\frac{4\pi}{\lambda}(\Delta d-\Delta\bar{d})+\frac{4\pi}{\lambda}\frac{B_{\perp}}{r\sin\theta}(\Delta z-\Delta\bar{z})+(\Delta\phi_{atmo}-\Delta\bar{\phi}_{atmo})+\Delta\phi_{n}\right]\approx 0, \tag{2}$$

where N_{az} and N_{rg} are total numbers of azimuth and range pixels; i and j are azimuth and range pixel coordinates; and $\Delta\bar{d}$, $\Delta\bar{z}$, and $\Delta\bar{\phi}_{atmo}$ are the estimated values of surface displacement, topographic error, and atmospheric phase delay. Equation 2 is used to correct phase values in each interferogram. The correct reference phase values should be such that the left term in equation 2 accurately represents the noise in a given interferogram (the residual phase values of the interferogram should be approximately zero after spatial averaging).

Figure 3 shows a block diagram of the refined SBAS InSAR processing algorithm. All the interferograms are classified as HQ or LQ, and the mean deformation rate ($\bar{v}$) is estimated from the HQ interferograms by using the relation

$$\bar{v}(x,r)=\frac{\lambda}{4\pi}\frac{\sum_{k=1}^{N_{hq}}\Delta\phi_{k}\,(x,r)}{\sum_{k=1}^{N_{hq}}\Delta t_{k}}\quad, \tag{3}$$

where k is the k th interferogram, N_{hq} is the total number of HQ interferograms and Δt is the time difference between master and slave images. This approach is better than deriving the mean deformation rate from linear regression of the deformation rates estimated from all interferograms, because atmospheric and orbital artifacts are, to a certain degree, mitigated

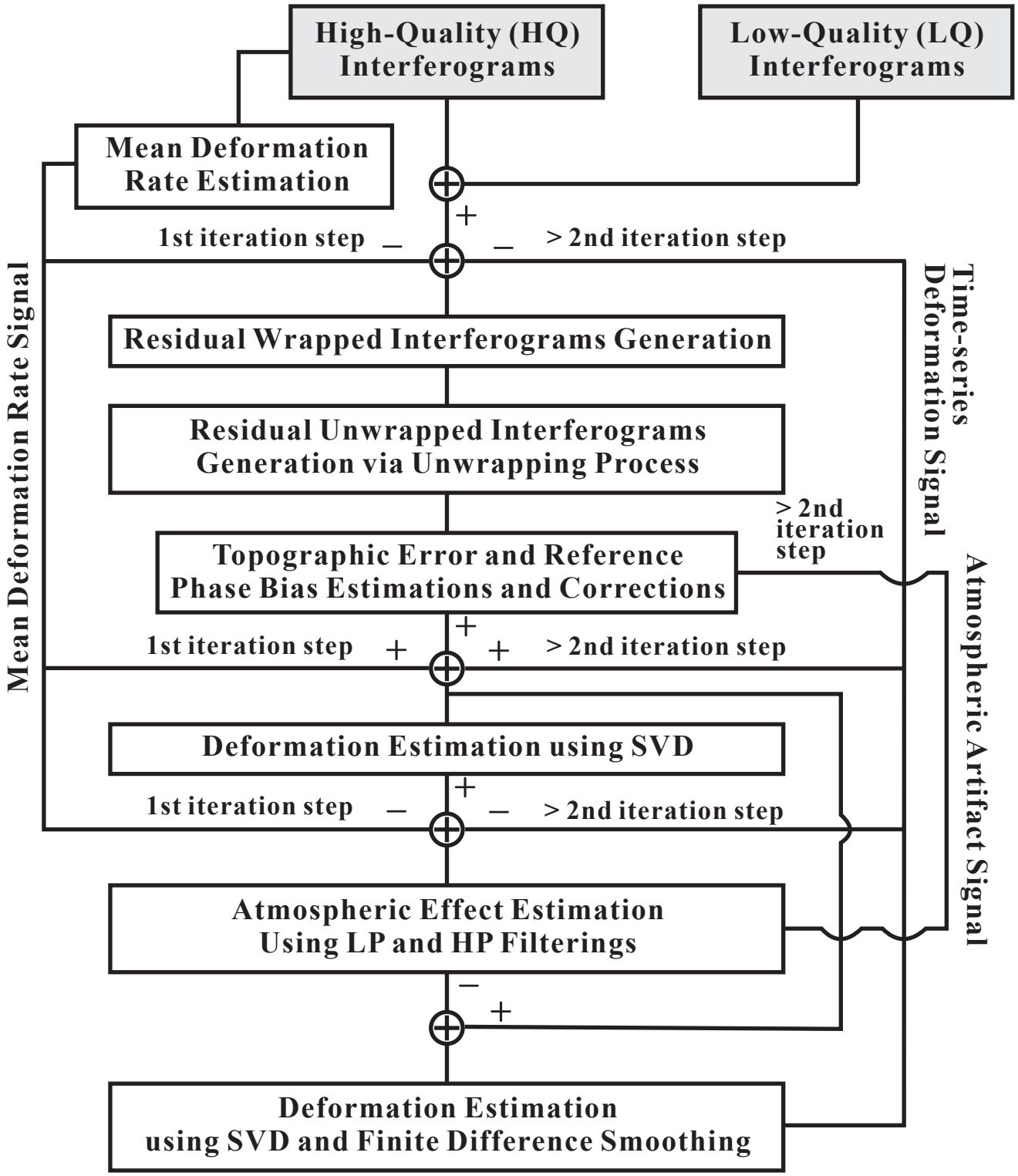


Figure 3. Block diagram of the refined small baseline subset (SBAS) interferometric synthetic aperture radar (InSAR) processing algorithm.

by eliminating LQ interferograms from the computation. New, wrapped residual interferograms are formed by subtracting the estimated linear deformation from each interferogram on a pixel-by-pixel basis. The residual interferograms are reunwrapped to create new unwrapped interferograms. This step essentially removes phase unwrapping errors from the LQ interferograms, because the fringe rates in the residual interferograms are much lower than those in the original interferograms.

The phase values in residual interferograms, ϕ_r, include topographic errors that depend on the perpendicular baselines. The topographic errors are estimated from all the residual interferograms as follows:

$$\Delta z(x,r) = \frac{\lambda}{4\pi} r \sin\theta \frac{\sum_{k=1}^{N_i} \left(\Delta\phi_r\right)_k (x,r)}{\sum_{k=1}^{N_i} \left(B_\perp\right)_k} , \quad (4)$$

where N_i is the total number of interferograms. The residual interferograms after removing the topographic errors are defined by

$$\left(\Delta\phi_{rt}\right)_k (i,j) = \left(\Delta\phi_r\right)_i (i,j) - \frac{4\pi}{\lambda} \frac{\left(B_\perp\right)_k}{r\sin\theta} \Delta z(i,j)$$
$$\text{for } k = 1, 2, \ldots N_i , \quad (5)$$

where $(\Delta\phi_{rt})$ k is the k th residual interferogram corrected for topographic error, and the reference phase bias (ϕ_{ref}) for the k th interferogram is estimated from coherent pixels as follows:

$$\left(\phi_{ref}\right)_k = \frac{1}{N_{az} N_{rg}} \sum_{i=1}^{N_{az}} \sum_{j=1}^{N_{rg}} \left(\Delta\phi_{rt}\right)_k (i,j)$$
$$\text{for } k = 1, 2, \ldots N_i . \quad (6)$$

Next, the topography-corrected interferogram phase, $\Delta\phi_{rt}$ in equation 5, is further corrected by using the reference phase bias, ϕ_{ref} in equation 6. At this stage, the estimated linear deformation from equation 3 is added back to the topography-corrected interferograms, in which the reference phase bias has also been corrected by using equation 6. We call the resulting interferograms "corrected interferograms."

Our next objective is to estimate and remove atmospheric artifacts. To achieve this, we estimate the time-series deformation histories at each coherent pixel by using the SVD operation, and remove them from the corrected interferograms. The atmospheric artifacts are then removed by temporal high-pass (HP) and spatial low-pass (LP) filtering operations, because the atmospheric artifacts are spatially correlated and temporally random. After the atmospheric contributions are removed in this way, we recompute the time-series deformation by simultaneously applying the SVD approach and the finite difference smoothing method (Schmidt and Burgmann, 2003) in order to further suppress the noise contribution. This completes the first iteration of our refined SBAS InSAR processing, and results in time-series deformation estimates at each coherent pixel.

Parameter optimization and estimation in the above implementation of SBAS InSAR processing are based on the assumption of the linear deformation (equation 3). To get beyond the assumption of linearity, all processing steps are reapplied to the interferograms by using the estimated time-series deformation from the first SBAS InSAR iteration instead of the linear deformation estimated from equation 3. Our second iteration of SBAS InSAR processing corrects the topographic error, the reference phase bias, and the atmospheric artifact. Furthermore, the reference phase correction in equation 6 is refined by taking into account the estimated atmospheric artifact phase from the first iteration:

$$\left(\phi_{ref}\right)_k = \frac{1}{N_{az} N_{rg}} \sum_{i=1}^{N_{az}} \sum_{j=1}^{N_{rg}}$$
$$\left[\left(\Delta\phi_{rt}\right)_k (i,j) - \left(\Delta\bar{\phi}_{atmo}\right)_k (i,j)\right]$$
$$\text{for } k = 1, 2, \ldots N_i . \quad (7)$$

Refined SBAS InSAR Applied to Augustine Volcano

We investigated surface deformation of Augustine Volcano from 1992 to 2005 using a refined multiple-interferogram processing procedure. Our SBAS InSAR processing improves the original SBAS InSAR algorithm in the following aspects:

1. We divide all InSAR interferograms into HQ and LQ interferograms, and estimate the initial mean deformation rate by using the HQ interferograms only. This is critical because the topographic error, the atmospheric contribution, and the residual phase estimate largely depend on the estimated mean deformation rate. If the mean deformation rate is estimated poorly, the measured time-series deformation will be distorted. For this reason, the initial mean deformation rate is estimated by using only high-quality interferograms in which phase coherence is good and no phase unwrapping error exists.
2. The mean deformation rate is calculated under the assumption that the deformation rate is constant. Any departure from this assumption (such as time-variant deformation) will introduce significant errors in estimating the atmospheric contribution and the topographic error. To overcome this drawback in the original SBAS InSAR algorithm, an iterative approach was applied to our refined SBAS InSAR algorithm. In the first step, our SBAS InSAR algorithm estimates the atmospheric

contribution and the topographic error by using the initial mean deformation rate, and then calculates the time-series deformation. In the second step, our algorithm estimates the atmospheric contribution and the topographic error by using the time-series deformation from the first iteration instead of the initial mean deformation rate. This approach efficiently separates the atmospheric contribution and the topographic error from interferograms and improves the time-series deformation measurement. The original SBAS InSAR algorithm does not include the iteration step

3. We have incorporated the finite-difference noise compression approach (Schmidt and Burgmann, 2003) into the original SBAS InSAR algorithm.

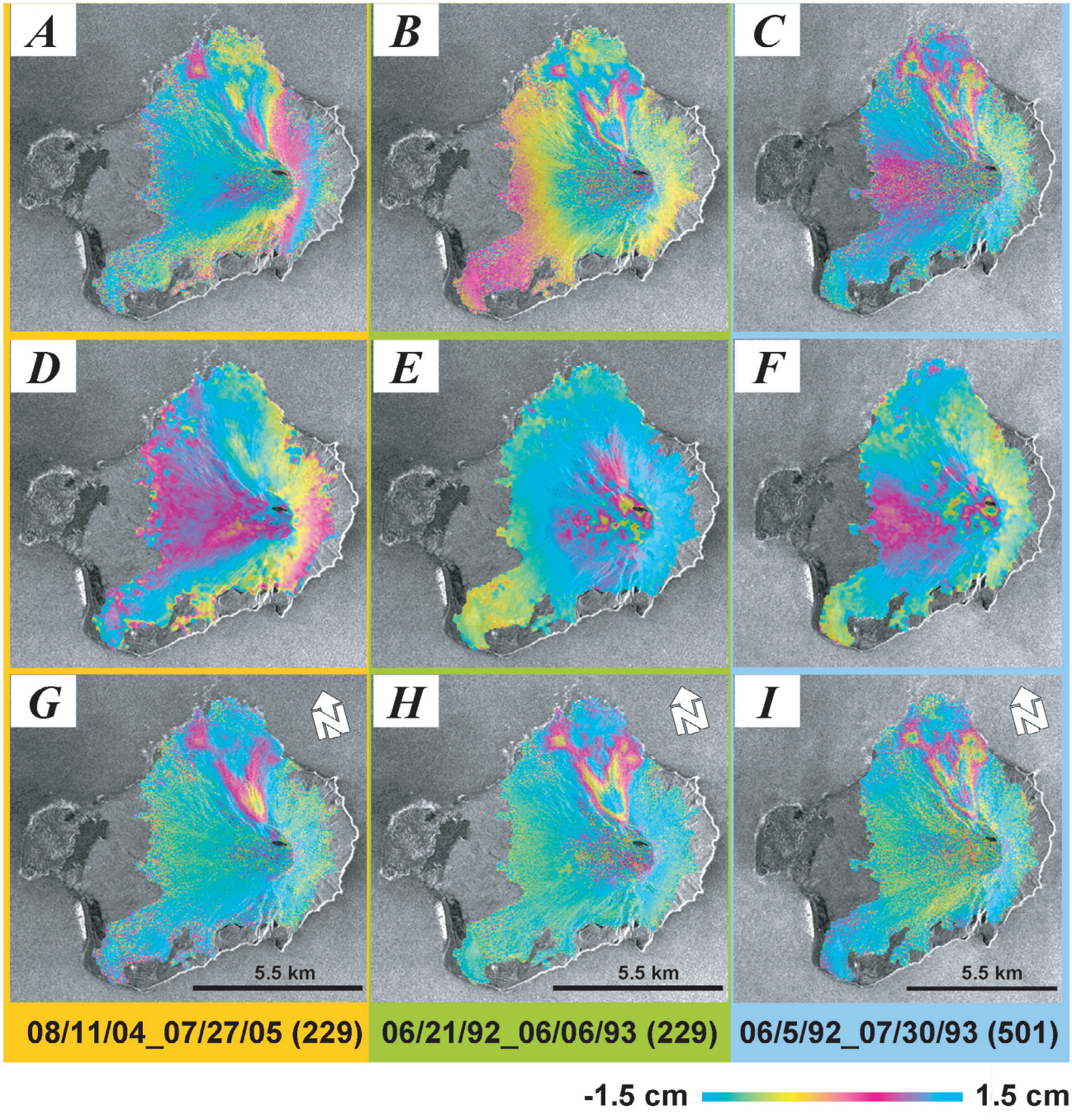


Figure 4. *A, B,* and *C,* Unwrapped interferograms of Augustine Volcano before small baseline subset (SBAS) interferometric synthetic aperture radar (InSAR) processing. *D, E,* and *F,* Atmospheric effects modeled using spatial low-pass filtering and temporal high-pass filtering. *G, H,* and *I,* Refined interferograms after removing atmospheric effects.

4. The reference phase correction procedure is a significant improvement in our refined SBAS InSAR algorithm. The reference phase is refined by several iteration steps. The initial reference phase correction is applied to the unwrapped residual interferograms. The correction is performed by removing the mean of the unwrapped residual interferograms and removing the bias caused by the atmospheric contribution. The initial phase correction can be slightly biased, but the bias is further corrected through iterations while the estimates of the atmospheric contribution and the topographic error are refined.

We applied the refined SBAS InSAR processing algorithm to 25 and 27 interferograms from satellite tracks 229 and 501, respectively. Among interferograms from track 229, there were 16 classified as HQ and 9 as LQ on the basis of the amount of phase unwrapping error. For track 501, there were 17 and 10 interferograms classified as HQ and LQ, respectively. A point near GPS station P2 (fig. 5) was selected as an initial reference point for SBAS InSAR processing.

Our processing procedures are briefly summarized here. During the first iteration of SBAS InSAR processing, unwrapped interferograms are corrected for the phase value at the reference point and the mean deformation rates are estimated in all coherent pixels from the HQ interferograms by using equation 3. The estimated mean deformation rates are then removed from all original wrapped interferograms (both HQ and LQ ones) to produce new wrapped residual interferograms. Then the phase unwrapping procedure is applied to the wrapped residual interferograms. We then estimate and remove topographic errors from the residual interferograms by using equation 4 and correct the reference phase bias by using equation 6. The corrected residual phase values are restored by adding back the linear deformation phase, and the initial time-series surface deformation histories are estimated from all interferograms by using the SVD approach. Spatial low-pass filtering and temporal high-pass filtering are then applied to estimate atmospheric artifacts. After the phase values due to the atmospheric contribution are removed from interferograms, the SVD approach and the finite difference smoothing method are applied simultaneously to further suppress the noise contribution. During the second iteration of SBAS InSAR processing, all processing steps are reapplied using the estimated time-series deformation histories from the first iteration. These final time-series deformation measurements are improved through iteratively refining the topographic error, the reference phase bias, and the atmospheric artifact.

Figure 4 shows three sets of interferograms, demonstrating the effectiveness of our refined SBAS InSAR algorithm in reducing atmospheric artifacts. Figures 4*A*–4*C* are three original InSAR images in which atmospheric anomalies amount to 3 to 5 cm.figures 4*D*–4*F* are primarily atmospheric artifacts modeled using spatial low-pass filtering and temporal high-pass filtering of multiple InSAR images. Figures 4*G*–4*I* are refined InSAR images in which atmospheric artifacts are mostly removed.

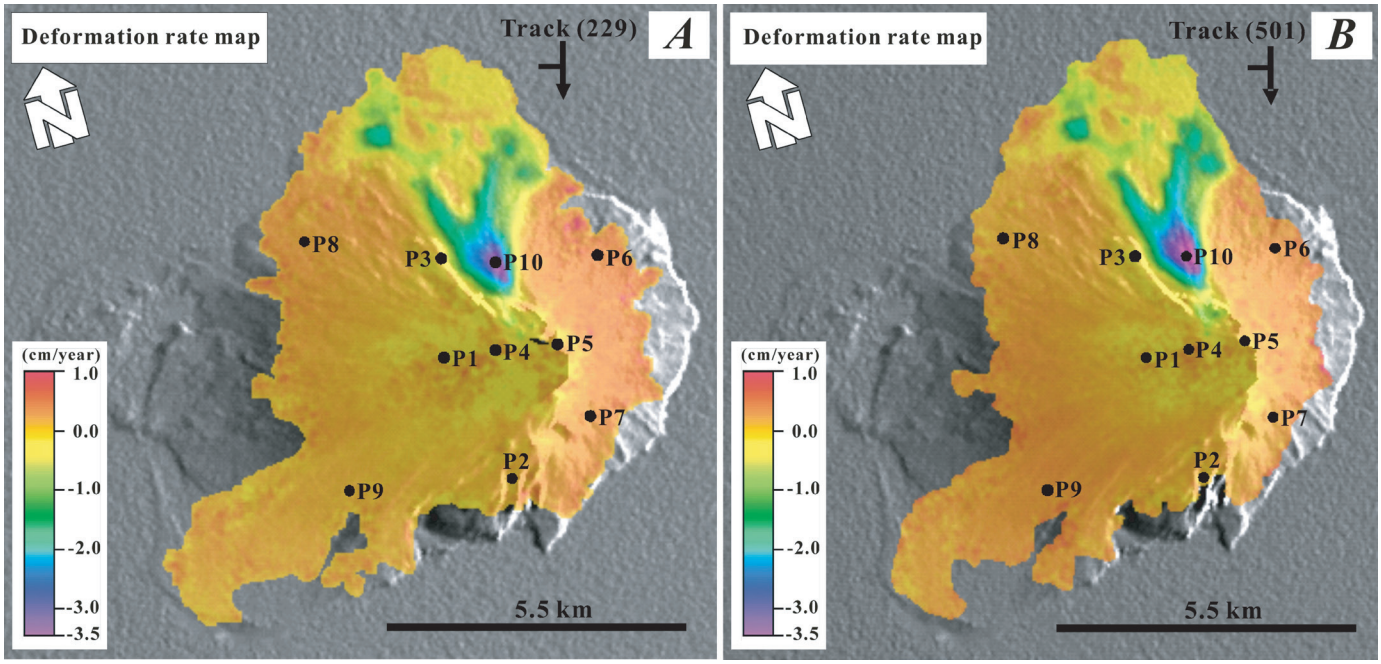


Figure 5. Maps of averaged deformation rate for Augustine Volcano from the refined small baseline subset (SBAS) technique for the period 1992–2005. *A,* Satellite track 229. *B,* Satellite track 501. Results from two independent tracks show similar results. Largest displacements are associated with subsidence of 1986 pyroclastic flow deposits in upper right quadrants of the maps.

Using our SBAS InSAR processing procedure, we conducted time-series analysis for interferograms from two independent satellite tracks: 229 and 501. We do not have other time-series deformation measurements during most of the time of investigation to compare with our results, so we compared results from two independent tracks for quality assurance. Figures 5*A* and 5*B* show mean deformation rate maps for Augustine Volcano from 1992 to 2005 that were created by using the refined SBAS InSAR technique. The mean deformation rates from the two independent tracks agree with each other well (figs. 5*A* and 5*B*). In general, we observe a wholesale uplift of Augustine Volcano, with slightly more uplift on the lower flanks.

Next, we show time-series deformation for several locations across the island. Figure 6 shows the corresponding time-series surface deformation histories at each point from tracks 229 and 501. Figures 6*A*–6*D* show surface displacement (uplift) of 4 to 6 cm for the lower flanks of Augustine

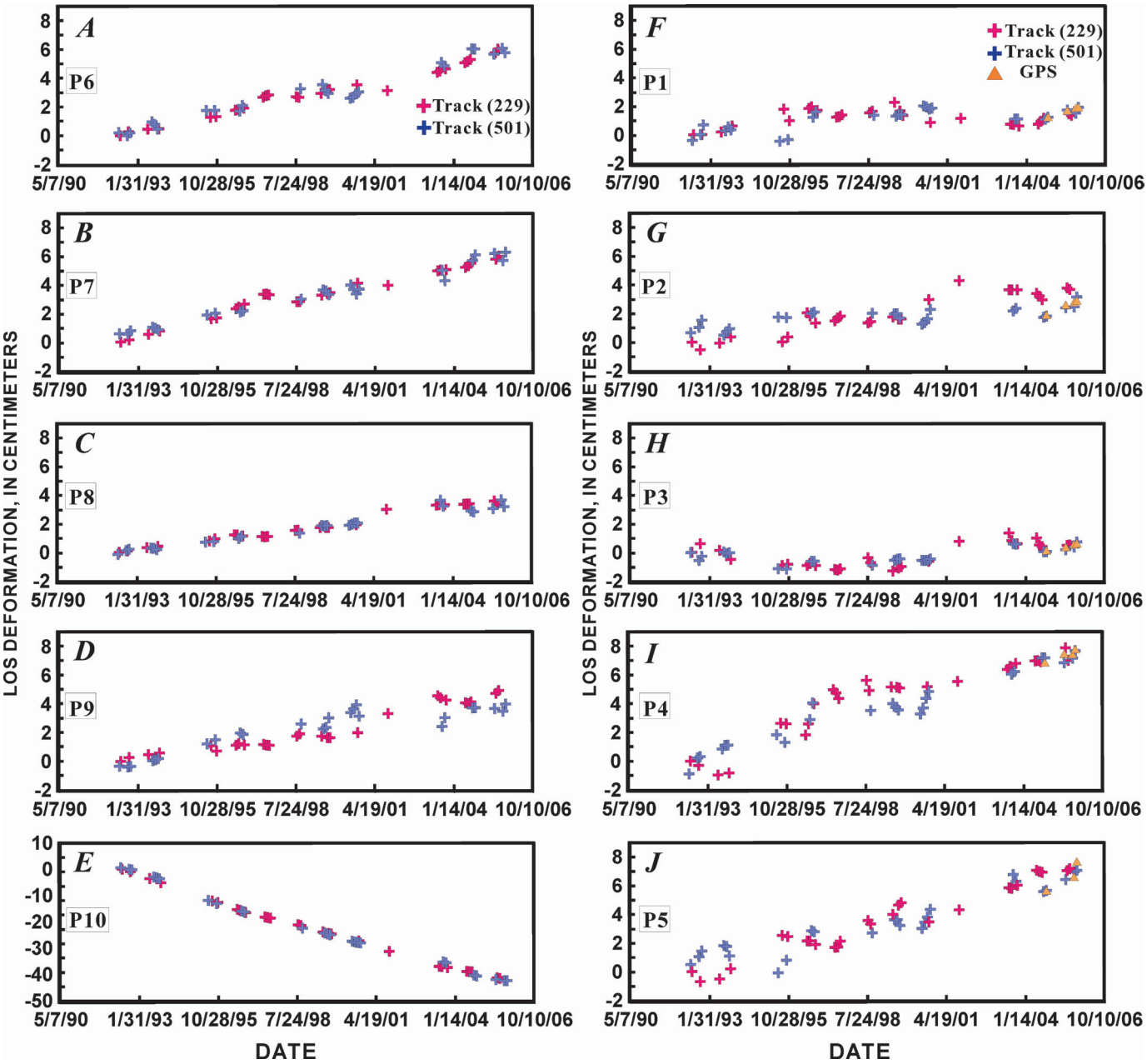


Figure 6. Line-of-sight (LOS) surface-displacement time-series for selected points (see fig. 5) on Augustine Volcano for the period 1992–2005. Red and blue symbols reflect satellite tracks 229 and 501, respectively. Continuous Global Positioning System (CGPS) measurements at five locations for 2004–2005 are also shown (triangles).

Volcano during the 13 years of the investigation. Figure 6*E* shows about 40 cm of subsidence for the 1986 pyroclastic flow deposit.

A network of continuous Global Positioning System (CGPS) receivers (P1–P5) was installed on the volcano by the Plate Boundary Observatory in fall 2004 (Pauk, this volume). We used the GPS data to validate InSAR measurements for the overlapping time interval between September 2004 and October 2005. All GPS data were converted into the InSAR line-of-sight (LOS) vector. Figures 6*F*–6*J* show time-series displacement at CGPS locations, comparing SBAS InSAR results and CGPS data from September 2004 to October 2005. The CGPS displacements were projected to the LOS vector by using the InSAR imaging geometry for track 501. About 3 to 8 cm of uplift is observed at five CGPS locations (figs. 6*F*–6*J*). In general, we find that the interferometric coherence on the upper part of Augustine Volcano, where CGPS stations are located, is worse than on the lower flanks (figs. 6*A*–6*E*). This is the main reason why SBAS InSAR time-series results look noisy (figs. 6*F*–6*J*). From September 2004 to October 2005, SBAS InSAR results indicate about 5 to 15 mm uplift at the five CGPS locations. These results agree with the CGPS observations that indicate Augustine Volcano had been inflated from early summer 2005 to the time of its eruption in January 2006 (Cervelli and others, 2006; Cervelli and others, this volume).

Deformation Modeling and Analysis

Our refined SBAS InSAR algorithm allows us to retrieve temporal surface deformation information while minimizing atmospheric artifacts, DEM errors, and phase unwrapping errors. We have processed InSAR images from two descending satellite tracks and found that the independent results indicate very similar trends, giving us confidence in our refined algorithm. CGPS observations during September 2004 to October 2005 further validate the refined SBAS InSAR processing algorithm.

Surface displacement at Augustine Volcano can be characterized as a wholesale uplift of the island by 2 to 8 cm during the 13 years of investigation. The amount of uplift of the upper flanks is slightly less than that of the lower flanks. To estimate the location of the source responsible for the observed surface displacement, we modeled the averaged deformation interferograms in figure 5 by using two point sources embedded in an elastic homogeneous half-space (Mogi, 1958). The four parameters used to describe a Mogi source are horizontal location (x, y), depth, and strength, which is related to a change in pressure, volume, or both. A nonlinear least squares inversion approach was used to optimize the source parameters. This approach minimizes a merit function defined as the chi-squared difference between the observed and synthetic interferograms. The Levenberg-Marquardt Method (Press and others, 1992) was used to iteratively improve the trial solution until the chi-squared effectively stopped decreasing. To account for topographic effects, we adopted a simple approach proposed by Williams and Wadge (1998) in which the elevation of the reference surface varies according to the elevation of each computation point in the model.

To model the deformation by using two Mogi sources, we first masked out the subsidence associated with the 1986 pyroclastic flow deposit, which was attributed to thermoelastic contraction (Masterlark and others, 2006). Next, we used a Mogi source to model the deformation of the upper part of the volcano by masking out the deformation over the lower half. In this case, we also included three ramping phase terms ($a+bx+cy$, where x and y are pixel coordinates) to account for the wholesale uplift of the volcano. The best source model is located 1.7 to 3.8 km below mean sea level, with an averaged contracting volume of about 0.2 million m^3/yr. Using the best-fit location for this first Mogi source, we generated a modeled deformation image (fig. 7*B*) and removed it from the observed deformation image (fig. 7*A*). The resulting deformation field over the lower part of the volcano was modeled with a second Mogi source. In this case, we did not include the three ramping phase terms in order to model the long-wavelength uplift, and we fixed the horizontal location of the second source to that of the first source (the second source is located directly beneath the first). The depth of the second Mogi source is poorly constrained. The best fit was obtained with a source 7 to 12 km below mean sea level inflating at about 2 million m^3/yr (fig. 7*C*). Figure 7*D* shows the modeled deformation from the use of two Mogi sources, which reproduce most aspects of the observed displacement field relatively well. We recognize that our modeling is preliminary and acknowledge that many alternative models can explain the observed deformation equally well.

A preliminary two-source model that reproduces the observed displacement field at Augustine Volcano during 1992–2005 consists of a contracting source 2 to 4 km below mean sea level and an inflating source 7 to 12 km below mean sea level. The shallower source might represent a shallow magma reservoir that fed the 1976 and 2006 eruptions, and was responsible for the volcano-tectonic earthquakes at depths of 2 to 5 km below sea level that preceded the 1976 eruptions and followed the 2006 eruptions (Power and Lalla, this volume). Petrologic evidence also suggests this as a source depth for 2006 magma (Larsen and others, this volume). The deeper source could be a long-term magma storage zone beneath the volcano.

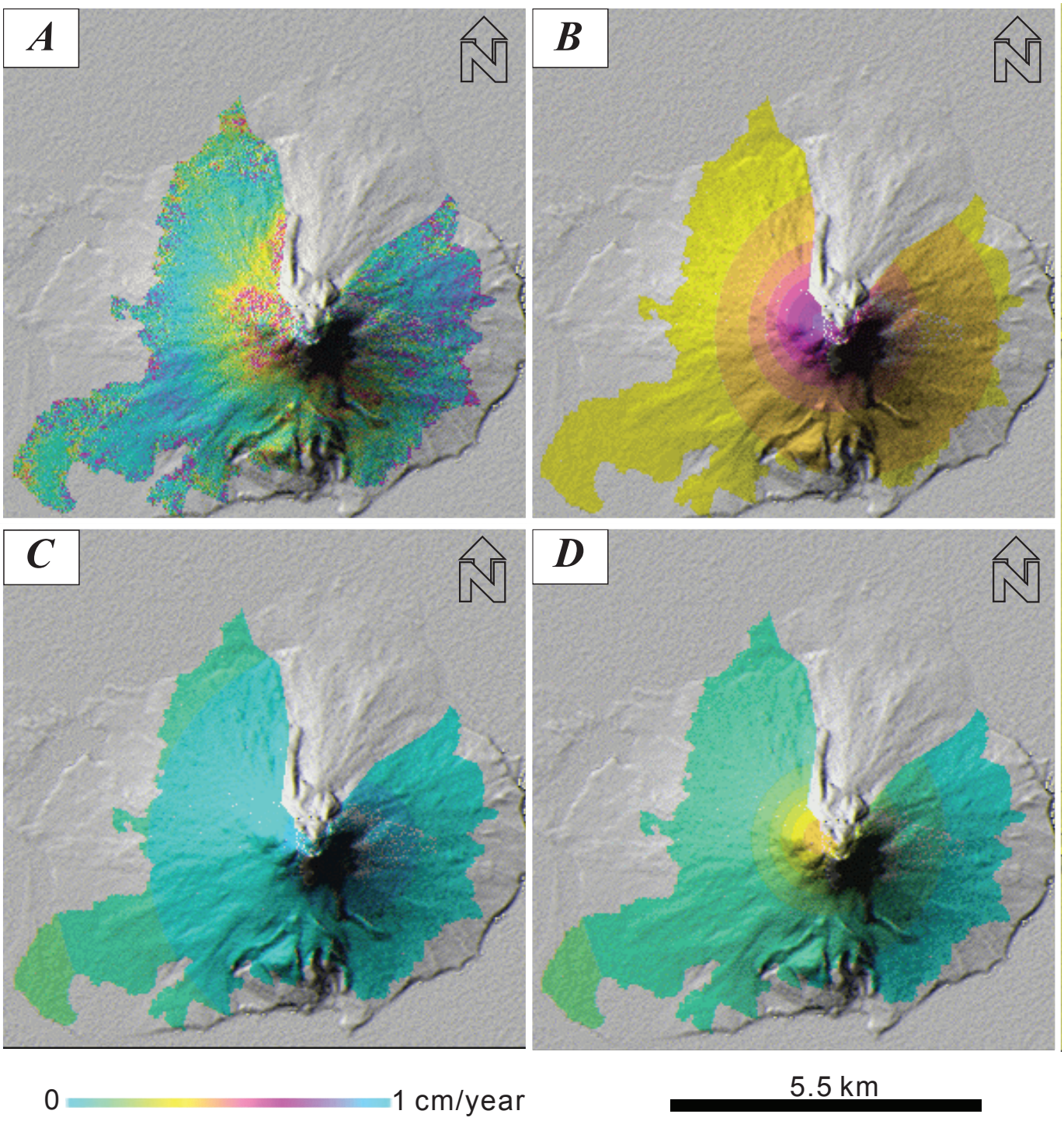


Figure 7. *A,* Observed averaged deformation rate of Augustine Volcano, 1992–2005. *B,* Modeled deformation from a contracting source 3.3 km below mean sea level. *C,* Modeled deformation from an expanding source 9.6 km below mean sea level. *D,* Modeled deformation from both Mogi sources (*B* and *C*).

Conclusions

We have developed a SBAS InSAR processing algorithm to study ground surface deformation by characterizing and removing atmospheric artifacts and DEM errors to improve surface deformation measurements through a multi-interferogram approach. The technique represents a significant advance and is particularly capable of retrieving subtle deformation over a long time interval. We applied the SBAS InSAR technique to Augustine Volcano by using SAR images from two independent datasets during 1992 and October 2005. Time-series deformation measurements from two satellite tracks agree with each other, both suggesting 2 to 8 cm uplift of the volcano during the time of investigation. The InSAR results also agree with CGPS observations at five stations that began operating in September 2004. A preliminary model consisting of a contracting Mogi source 2 to 4 km below mean level and an inflating Mogi source 7 to 12 km below mean sea level reproduces the observed displacement field reasonably well. The deeper source might represent a long-term magma storage zone beneath the volcano, and the shallower source a magma reservoir responsible for swarms of volcano-tectonic earthquakes that preceded and followed the 1976 and 2006 eruptions. Net contraction of the shallower source during a 13-year period leading up to the 2006 eruption might be a result of magma degassing or cooling. If so, both sources would seem to be long-term features of the magma plumbing system at Augustine. The shallower source, in particular, might be amenable to investigation by seismic tomography or other geophysical techniques.

Acknowledgments

SAR data used in this study are copyrighted by the European Space Agency (ESA) and were provided by the Alaska Satellite Facility. We thank Chuck Wicks for sharing his Matlab modeling codes, J. Power for sharing his insightful information about Augustine seismicity, and J. Power and R. Rykhus for technical review. This work is supported by the National Aeronautics and Space Administration (NASA) Earth Surface and Interior Program (05/0021), the U.S. Geological Survey (USGS) Volcano Hazards Program, and the USGS Land Remote Sensing Program.

References Cited

Begét, J.E., and Kowalik, Z., 2006, Confirmation and calibration of computer modeling of tsunamis produced by Augustine Volcano, Alaska: Science of Tsunami Hazards, v. 24, no. 4, p. 257–267.

Berardino, P., Fornaro, G., Lanari, R., and Sansoti, E., 2002, A new algorithm for surface deformation monitoring based on small baseline differential SAR interferograms: Institute of Electrical and Electronics Engineers Transactions on Geosciences and Remote Sensing, v. 40, no. 11, p. 2375–2383.

Cervelli, P., Fournier, T., Freymueller, J., and Power, J.A., 2006, Ground deformation associated with the precursory unrest and early phases of the January 2006 eruption of Augustine Volcano, Alaska: Geophysical Research Letters, v. 33, L18304, doi: 10.1029/2006GL027219.

Cervelli, P.F., Fournier, T.J., Freymueller, J.T., Power, J.A., Lisowski, M., and Pauk, B.A., 2010, Geodetic constraints on magma movement and withdrawal during the 2006 eruption of Augustine Volcano, *in* Power, J.A., Coombs, M.L., and Freymueller, J.T., eds., The 2006 eruption of Augustine Volcano, Alaska: U.S. Geological Survey Professional Paper 1769 (this volume).

Dzurisin, D., 2007, Volcano Deformation—Geodetic Monitoring Techniques: Springer Praxis Publishing Ltd., UK.

Farr, T., and 17 others, 2007, The Shuttle Radar Topography Mission: Reviews of Geophysics, 45, RG2004, doi:10.1029/2005RG000183.

Ferretti, A., Prati, C., and Rocca, F., 2001, Permanent scatterers in SAR interferometry: Institute of Electrical and Electronics Engineers Transactions on Geosciences and Remote Sensing, v. 39, p. 8–22.

Gabriel, A.K., Goldstein, R.M., and Zebker, H.A., 1989, Mapping small elevation changes over large areas—differential interferometry: Journal of Geophysical Research, v. 94, p. 9183–9191.

Kienle, J., and Shaw, G.E., 1979, Plume dynamics, thermal energy and long-distance transport of vulcanian eruption clouds from Augustine Volcano, Alaska: Journal of Volcanology and Geothermal Research, v. 6, no. 1-2, p. 139–164.

Larsen, J.F., Nye, C.J., Coombs, M.L., Tilman, M., Izbekov, P., and Cameron, C., 2010, Petrology and geochemistry of the 2006 eruption of Augustine Volcano, *in* Power, J.A., Coombs, M.L., and Freymueller, J.T., eds., The 2006 eruption of Augustine Volcano, Alaska: U.S. Geological Survey Professional Paper 1769 (this volume).

Lee, C., Lu, Z., Kwoun, O., and Won, J., 2008, Deformation of Augustine volcano, Alaska, 1992–2005, measured by ERS and ENVISAT SAR interferometry: Earth, Planets and Space, v. 60, 447–452.

Lu, Z., Wicks, C., Dzurisin, D., Power, J., Thatcher, W., and Masterlark, T., 2003, Interferometric synthetic aperture radar studies of Alaska volcanoes, Earth Observation Magazine , v. 12, no. 3, 8–18.

Lu, Z., Dzurisin, D., Wicks, C., Jr., Power, J., Kwoun, O., and Rykhus, R., 2007, Diverse deformation patterns of Aleutian volcanoes from satellite interferometric synthetic

aperture radar (InSAR), *in* Eichelberger, J.C., Gordeev, E., Izbekov, P., Kasahara, M., and Lees, J.M., eds., Volcanism and tectonics of the Kamchatka Peninsula and adjacent arcs: American Geophysical Union Geophysical Monograph 172, p. 249–261.

Masterlark, T., Lu, Z., and Rykhus, R., 2006, Thickness distribution of a cooling pyroclastic flow deposit on Augustine Volcano, Alaska—optimization using InSAR, FEMs, and an adaptive mesh algorithm: Journal of Volcanology and Geothermal Research, v. 150, p. 186–201.

Miller, T.M., McGimsey, R.G., Richter, D.H., Riehle, J.R., Nye, C.J., Yount, M.E., and Dumoulin, J.A., 1998, Catalog of the historically active volcanoes of Alaska: U.S. Geological Survey Open-File Report 98-582, 104 p.

Mogi, K., 1958, Relations between the eruptions of various volcanoes and the deformations of the ground surface around them: Bulletin of the Earthquake Research Institute, University of Tokyo, v. 36, p. 99–134.

Pauk, B.A., Jackson, M., Feaux, K., Mencin, D., and Bohnenstiehl, K., 2010, The Plate Boundary Observatory permanent global positioning system network on Augustine Volcano before and after the 2006 eruption, *in* Power, J.A., Coombs, M.L., and Freymueller, J.T., eds., The 2006 eruption of Augustine Volcano, Alaska: U.S. Geological Survey Professional Paper 1769 (this volume).

Pauk, B.A., Power, J.A., Lisowski, M., Dzurisin, D., Iwatsubo, E.Y., and Melbourne, T., 2001, Global Positioning System (GPS) survey of Augustine Volcano, Alaska, August 3–8, 2000—data processing, geodetic coordinates and comparison with prior geodetic surveys: U.S. Geological Survey Open-File Report 01-099, 20 p.

Power, J.A., and Iwatsubo, E.Y., 1998, Measurements of slope distances and zenith angles at Augustine Volcano, Alaska, 1986, 1988, and 1989: U.S. Geological Survey Open-File Report 98-0145, 17 p.

Power, J.A., and Lalla, D.J., 2010, Seismic observations of Augustine Volcano, 1970–2007, *in* Power, J.A., Coombs, M.L., and Freymueller, J.T., eds., The 2006 eruption of Augustine Volcano, Alaska: U.S. Geological Survey Professional Paper 1769 (this volume).

Press, W., Teukolsky, S., Vetterling, W., and Flannery, B., 1992, Numerical recipes in C, the art of scientific computing: Cambridge University Press, 994 p.

Schmidt, D., and Burgmann, R., 2003, Time-dependent land uplift and subsidence in the Santa Clara Valley, California, from a large interferometric synthetic aperture radar data set: Journal of Geophysical Research v. 108, no. B9, 2416, doi:10.1029/2002JB002267.

Waythomas, C.F., and Waitt, R.B., 1998, Preliminary volcano-hazard assessment for Augustine Volcano, Alaska: U.S. Geological Survey Open-File Report 98-0106, 39 p.

Williams, C.A., and Wadge, G., 1998, The effects of topography on magma reservoir deformation models—application to Mt. Etna and radar interferometry: Geophysical Research Letters., v. 25, 1549–1552.

Zebker, H.A., Amelung, F., and Jonsson, S., 2000, Remote sensing of volcano surface and internal processes using radar interferometry, *in* Mouginis-Mark, P., ed., Remote sensing of active volcanism: American Geophysical Union Monograph, v. 116, p. 179–205.

Zebker, H., Rosen, P., and Hensley, S., 1997, Atmospheric effects in interferometric synthetic aperture radar surface deformation and topographic maps: Journal of Geophysical Research, v. 102, p. 7547–7563.

This page intentionally left blank

The 2006 Eruption of Augustine Volcano, Alaska
Power, J.A., Coombs, M.L., and Freymueller, J.T., editors
U.S. Geological Survey Professional Paper 1769

Chapter 19

The Plate Boundary Observatory Permanent Global Positioning System Network on Augustine Volcano Before and After the 2006 Eruption

By Benjamin A. Pauk[1], Michael Jackson[2], Karl Feaux[2], David Mencin[2], and Kyle Bohnenstiehl[2]

Abstract

In September of 2004, UNAVCO and the National Science Foundation (NSF) funded EarthScope Plate Boundary Observatory (PBO) installed five permanent Continuous Global Positioning System (CGPS) stations on Augustine Volcano, supplementing one existing CGPS station operated by the Alaska Volcano Observatory. All six CGPS stations proved crucial to scientists for detecting and monitoring the precursory deformation of the volcano beginning in early May 2005, as well as for monitoring the many subsequent small inflationary and deflationary episodes that characterized the 2006 eruption. Following the eruption, in September of 2006, PBO added six additional permanent CGPS stations. The 2006 eruption and its precursors were the first significant activity of the volcano in 20 years and the PBO CGPS network provided an unprecedented opportunity to monitor and detect volcanic ground deformation on an erupting Alaskan stratovolcano. Data from the new CGPS stations coupled with the existing seismic stations provided scientists with the first real opportunity to use geodetic data and real time seismic data to assess the volcanic hazards before, during, and after an Alaskan eruption.

Introduction

This paper describes the development and expansion of the Continuous Global Positioning System (CGPS) before and after the 2006 eruption of Augustine Volcano. In September of 2004, the EarthScope Plate Boundary Observatory (PBO) installed five permanent CGPS stations on Augustine Volcano. In planning for the installation of the stations, staff from the PBO Alaska regional office worked closely with staff from the Alaska Volcano Observatory (AVO) and the PBO Magmatic Systems Site Selection Committee to install CGPS stations at strategic locations around the volcano. The goal was to provide a good spatial distribution of stations to monitor and detect both short- and long-term volcanic deformation in response to magmatic intrusions at depth and magma migration through the volcanic edifice.

Owing to its frequent eruptive activity, Augustine was a relatively well instrumented volcano prior to the 2006 eruption (Power and others, 2006). In 1992, AVO installed a three-station GPS network on the volcano consisting of dual-frequency, high-power-consumption Ashtech LD-XII receivers (Murray and others, 1992). These receivers were located on the base of the volcano (station AUGL), on the flank of the volcano, and on the top of the 1986 volcanic dome. Due to the high power consumption of the receivers, they were operated for only a few hours a day. A telemetered network of tiltmeters was installed in 1993 and 1994 to extend the coverage of deformational monitoring on the volcano (Dzurisin and others, 1994). In 1996, the Ashtech LD-XII receivers were replaced with lower power L1-only Ashtech SCA-12 receivers (Murray and others, 1996). In 2000, AVO replaced station AUGL with a dual frequency Trimble 4700 GPS receiver and dual frequency choke ring antenna, and the remaining two stations were no longer maintained. The continuous instrumentation deployed in the 1990s and repeated Electronic Distance Measurement (EDM) and GPS measurements of the volcano for the period 1988 to 2000 suggested no discernible pattern of displacement that could be attributed to magmatic activity on Augustine Volcano (Power and others, 1998; Pauk and others,

[1] U.S. Geological Survey, Cascades Volcano Observatory, 1300 SE Cardinal Court, Vancouver, WA 98683.

[2] UNAVCO, 6350 Nautilus Drive, Boulder, CO 80301.

2001). Prior to the installation of the five PBO CGPS stations in 2004, AVO operated only the one dual frequency CGPS station (AUGL) located on the east quadrant of the volcano. AUGL was incorporated into the PBO network in 2006 and subsequently renamed AV21 to comply with the PBO volcanic station naming scheme.

All five of the PBO CGPS stations and the one AVO CGPS on the volcano were operating normally at the onset of the eruption, but half of the network went offline shortly thereafter due to volcanic activity. Pyroclastic flows generated by the eruption completely destroyed two of the original five PBO stations and severely damaged a third, but spared the remaining three CGPS stations. These stations continued to operate throughout the explosive and effusive phases of the 2006 eruption.

In 2006, PBO installed six additional CGPS stations on the volcano at the request of the PBO Magmatic Systems Site Selection Committee to improve ongoing geodetic monitoring of the volcano. The Committee requested new locations to strengthen the existing network geometry and to improve the detection of subtle ongoing volcanic deformation signals at the volcano. The new stations were installed on the lower western and northern flanks of the volcano, on the southwest flank of the volcano, and on the upper flanks on the north and south side of the volcano (fig. 1; table 1). The spatial distribution of the new stations was dictated by the availability of competent bedrock on the volcano, line of site between stations and the AVO data communication facility in Homer, and attempts to fill gaps in the original network geometry and strengthen the geodetic monitoring of the volcano.

2004 CGPS Station Installations

PBO installed short drilled-braced monuments (SDBM) as the primary monument type for all the PBO CGPS stations on Augustine during both the 2004 and 2006 installations (fig. 2). The SDBM is a very stable, inexpensive, and durable monument that can be installed in exposed competent bedrock with off-the-shelf construction tools. The monument is constructed of 1-inch diameter Type 316 stainless steel rods that are welded into a stable tripod structure. The SDBM consists of a vertical leg braced by three diagonal legs inclined at approximately 55 degrees to the ground. All the legs extend approximate 2 m into the bedrock and converge with the center leg approximately 1.5 m above the ground surface. An electric hand held drill is used to drill all four 3.5 cm holes into the rock and each leg is grouted in place and the angled legs are welded to the central leg. The UNAVCO Web site (http://facility.unavco.org/project_support/permanent/monumentation/sdbm.htm, accessed September 28, 2009) provides detailed instructions and equipment lists for the construction of the SDBM. A stainless steel leveling mount is welded onto a threaded adaptor on the top of the center leg. A dual-frequency choke ring GPS antenna is attached to the leveling mount and a protective radome is put over the antenna.

For the Augustine network, PBO used the Trimble NetRS geodetic grade GPS receiver, Trimble part number 48164, and a radome covered Trimble dual frequency (L1/L2) choke ring antenna, model number TRM 26959.00, at each station. The NetRS is a low-power (3 Watt) rugged GPS receiver that allows for remote operation, status monitoring, and programming using Internet Protocol (IP) (fig. 3). Utilizing a standard internet browser, a user can access NetRS data and change data recording parameters. This proved helpful during times of volcanic unrest when conditions prohibited site access. The choke ring antenna is a reliable, low-power, multipath-resistant geodetic antenna that maintains millimeter precision (fig. 4).

The five CPGS stations were installed in competent bedrock outcrops with excellent sky view and clear telemetry paths to the AVO communications facility in Homer (fig. 1 and appendix 1). Unfortunately, the lack of competent bedrock in each quadrant prevented an ideal distribution of the stations; however, the final station distribution was sufficient to capture deformation on the upper and lower flanks of the volcano prior to and after the eruption. The network was concentrated within 5 km of the volcano's summit to ensure detection of shallow magmatic sources.

Each CGPS station on Augustine consisted of a Plaschem fiberglass hut or enclosure that houses the GPS receiver, a charge controller, surge protector, and 24 rechargeable 12 volt, 110 amp hour, sealed lead-acid batteries (fig 2). The 24 battery bank provides sufficient continuous power to all equipment throughout the long winter when there is limited daylight and the solar panels are encased in ice or snow and are not charging the batteries. The fiberglass huts are 5 ft square, 5 ft high, and weigh approximately 650 lbs. Due to the size and weight of the hut, a helicopter is required to sling the hut from an established base of operations to the designated remote station location on the volcano. One 64-watt solar panel was mounted to the angled south face of the hut to recharge the batteries. Three additional solar panels are mounted to an aluminum solar panel mounting structure or "swing set" located adjacent to the hut. The swing set is constructed of 2-inch-diameter, schedule-80 aluminum pipe that is coupled to the ground on the corners with rock bolts cemented into the bedrock or set in cement when installed in soil (fig. 5). Solar panels on the swing set recharge the batteries that supply the primary power source for the GPS receiver and digital radio components at each station. The swing sets used at the Augustine stations are a modified version of the swing set developed and utilized by AVO at many seismic stations on other Alaskan volcanoes. Complete metadata information including all equipment types, equipment serial numbers, data products, and photos for each Augustine station can be found on the PBO Web site at (http://pboweb.unavco.org/shared/scripts/gmap/, accessed September 28, 2009).

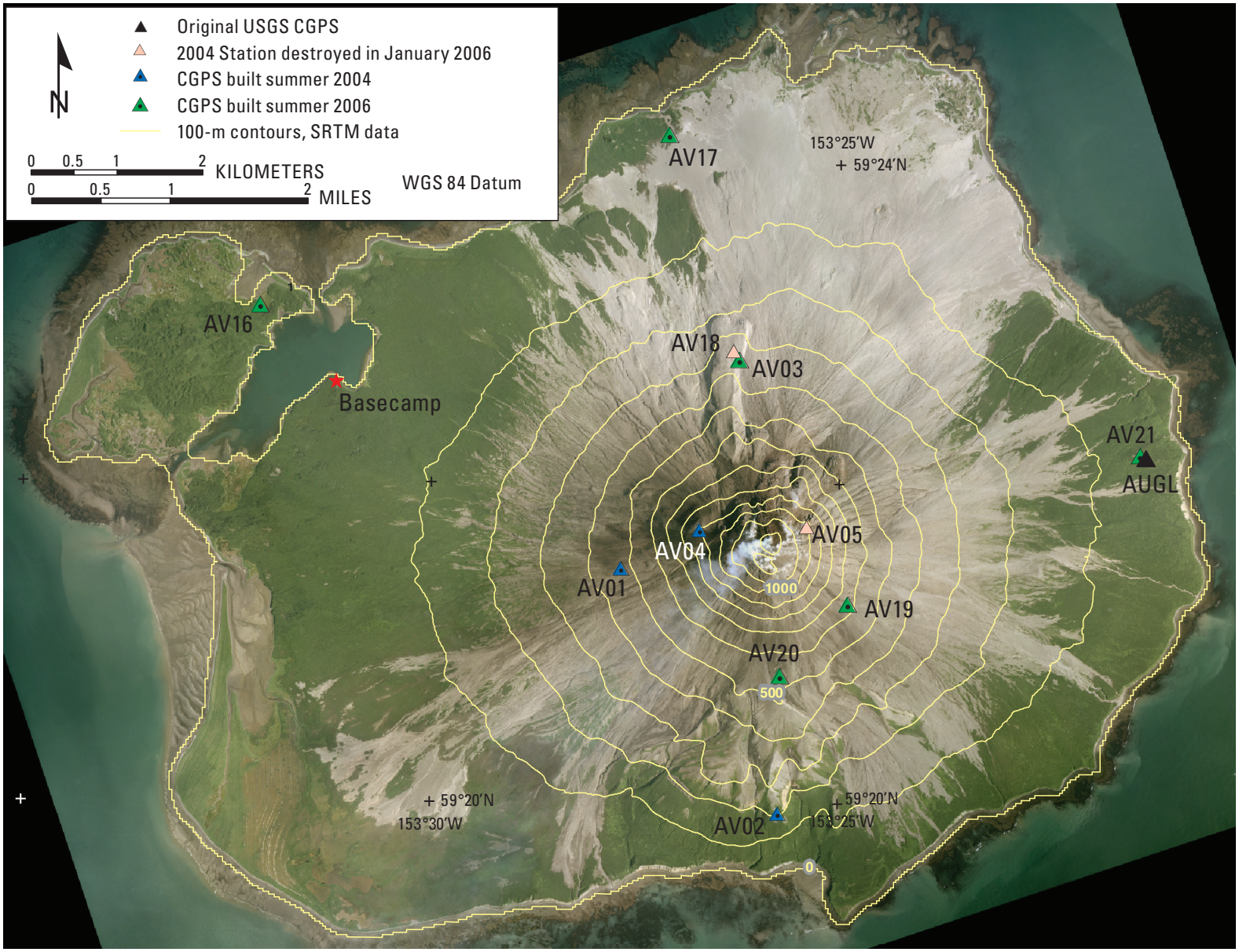


Figure 1. Map of Augustine Volcano showing Plate Boundary Observatory (PBO) Continuous Global Positioning System (CGPS) stations installed in 2004 and 2006, stations destroyed in the 2006 eruption, and Alaska Volcano Observatory (AVO) station on the volcano before the 2004 PBO installations. Note that station AV21 is in the same location as station AUGL. Base map from U.S. Geological Survey (USGS), orthophoto taken on July 12, 2006. Shuttle Radar Topography Mission (SRTM) contours.

Table 1. Geodetic coordinates of the Augustine GPS network and nearby regional Plate Boundary Observatory (PBO) GPS stations as of October 2006, including stations installed in 2004 and destroyed during the 2006 eruption of Augustine Volcano.

Station ID	PBO formal name	Longitude (degrees W)	Latitude (degrees N)	Elevation (meters)	Install date	Removal date
AC27	AC27MNEILAK2004	154.1630	59.2525	420.0	09/17/2004	Active
AC59	AC59URSUSAK2004	153.5852	59.5672	308.8	09/11/2004	Active
AUGL[1]	N/A	153.3539	59.3702	104.0	06/01/1996	01/09/2006
AV01	AV01AUGST_AK2004	153.4608	59.3585	47.9	09/10/2004	Active
AV02	AV02AUGST_AK2004	153.4284	59.3329	231.1	09/11/2004	Active
AV03	AV03AUGST_AK2004	153.4377	59.3812	360.2	09/08/2004	1/28/2006
AV04	AV04AUGST_AK2004	153.4447	59.3626	915.9	09/08/2004	Active
AV05	AV05AUGST_AK2004	153.2521	59.2146	1036.6	09/16/2004	1/13/2006
AV11	AUGS_MOUNAK2006	153.3546	59.3706	114.4	09/10/2006	Active
AV16	AUGLAGOONAK2006	153.5350	59.3859	26.5	09/04/2006	Active
AV17	AUGSTINNWAK2006	153.4510	59.4040	30.0	09/05/2006	Active
AV18	AUGVNORTHAK2006	153.4370	59.3800	370.0	09/03/2006	Active
AV19	AUGSTINSEAK2006	153.4140	59.3550	650.0	09/06/2006	Active
AV20	AUGS_SOUTHAK2006	153.4280	59.3470	540.0	09/11/2006	Active
AV21[1]	AV21AUGST_AK2006	153.3539	59.3702	104.0	01/09/2006	07/18/2008

[1] Sites AUGL and AV21 represent the same physical location. Only the name was changed.

2006 Augustine Eruption

All six CGPS stations on Augustine were operating prior to the 2006 eruption and proved useful in detecting inflation of the volcano before the eruption and subsequent deflation after the eruption (Cervelli and others, 2006; Cervelli and others, this volume). Unfortunately, pyroclastic flows damaged three of the stations early in the eruption. Station AV05 was destroyed on January 13 during the explosive stage of the eruption. Station AV04 was heavily damaged and stopped transmitting data on January 17 as the result of a large pyroclastic flow (fig. 6). Station AV03 continued to collect data until it was destroyed by a pyroclastic flow generated by an explosion on January 28 (fig. 7). Stations AV01, AV02, and AUGL were not damaged and remained operational throughout the entire eruption and subsequent debris flows generated on the volcano. Unfortunately, because of weather constraints and concern for crew safety, no attempt was made to repair AV04 until several months after the eruption had stopped and seismic activity had subsided. As a result of the station being offline, any deformation on the western flank of the volcano was not thoroughly recorded in the months that immediately followed the eruption.

2006 GPS Installations and Network Maintenance

In October of 2005, the PBO Magmatics Systems Site Selection Committee requested that the Alaska PBO regional office install an additional five to six permanent CGPS stations on Augustine in response to the precursory deformation of the volcano observed in the GPS data time series. The Alaska regional staff immediately began initial planning for the installation; however, severe winter conditions in Cook Inlet and concern about crew safety working on a restless volcano led to the decision to delay the installations until activity subsided and weather conditions were more favorable. However, in December of 2005, AVO staff upgraded the GPS station AUGL with a NSF-purchased NetRS GPS receiver, and the station was renamed AV21 and incorporated into the PBO network. Because of continued activity on the volcano after the 2006 eruption began, and because of other regional commitments, the Alaska regional office was unable to install the new stations until September of 2006.

During September of 2006, PBO installed an additional six new GPS stations on Augustine (fig. 1) and repaired AV04. At each new station, PBO built SDBM monuments and



Figure 2. Photo of Plate Boundary Observatory (PBO) station AV03, located on north side of Augustine Volcano. Station includes a standard PBO Short Drilled Braced Monument (SDBM) geodetic monument with GPS antenna enclosed in a plastic radome. Note that the original PBO style gray fiberglass enclosure and aluminum solar panel "swing set" installed in 2004. The station was completely destroyed by the 2006 eruption. Photo by Benjamin Pauk, September 12, 2004.

installed Trimble NetRS GPS receivers, Trimble choke ring antennas, and Intuicom digital radios. All data collected at the new stations were incorporated into the existing digital radio network telemetered to Homer.

The fiberglass enclosure huts deployed in 2006 are a larger and remodeled version of those installed in 2004. One key advantage of the new huts is that they were designed to accommodate two 64 watt solar panels (fig. 8). In addition, a new equipment mounting plate or back panel was developed and incorporated in the design for the interior of the enclosure. The new back panel is made of noncorrosive stainless steel and mounts to one of two sets of four bolts on either of the interior sides (east or west side) of the hut (fig. 9). The NetRS, Intuicom radio, charge controller, surge protector, and other associated equipment is mounted on to a single panel allowing rapid modular replacement of equipment.

The six stations installed in September of 2006 completed a robust network. Stations AV16 and AV17 were installed on the lower northwestern and western flanks of the volcano. Stations AV18 was installed within 300 m of the destroyed station AV03 on the north side of the volcano.



Figure 3. Photo of Trimble NetRS and Intuicom EB1 radio mounted inside an older style Plate Boundary Observatory (PBO) fiberglass enclosure installed on the volcano in 2004. Photo by Benjamin Pauk, September 9, 2004.

Station AV19 was installed on the southwestern flank of the volcano on a small spine of bedrock at an altitude of about 650 m. AV20 was installed in a bedrock outcrop approximately 1 km due north of station AV02 at a higher elevation on the volcano's southern flank. Due to concerns about the monumentation at AV21, a SDBM monument was built approximately 200 m west of AV21 and was designated as AV11, and AV21 was deactivated from the PBO network after the 2 stations recorded in parallel for almost two years. The heavily damaged station AV04 was repaired in 2006 and routine maintenance was performed at stations AV01, AV02, AC27, and AC59.

In addition to the 2006 hut modifications, a more rigid and durable swing set was designed and installed at three of the six new stations. No swing sets were needed at stations AV18, AV19, and AV20 as they have good southern exposure and are located on wind swept ridges where snow accumulations have historically been minimal. The new swing set was designed to withstand greater ice, snow, and wind loads commonly experienced by solar mounts on Augustine and other remote Alaskan volcanoes. Additional aluminum angled bar was bolted to the sides across the back of the panels to minimize flexure of the solar panels. The new hut and swing sets used the same 64-W solar panels deployed in 2004. As on the 2004 swing sets, all external connecting wires were enclosed in ½-inch-diameter Liquitite conduit, securely clamped to the aluminum poles and fed into the hut's power panel through a watertight plastic pass-through connection mounted to the side of the hut. In addition to the corners of the swing sets



Figure 5. Photo of solar panel "swing set" structure with three 64 watt panels installed in 2004 Plate Boundary Observatory (PBO) GPS stations on Augustine Volcano. Photo by Karl Feaux, September 11, 2004.



Figure 4. Photo of PBO station AV02 located on the south side of Augustine Volcano. Photo shows a Trimble L1/L2 choke ring dual frequency GPS antenna on a Plate Boundary Observatory (PBO) Short Drilled Braced Monument (SDBM). Plastic radome is removed to expose radome base, Southern California Integrated GPS Network (SCIGN) adapter and antenna. Monument is made of Type 316 1-inch diameter stainless steel rods. Photo by Karl Feaux, September 11, 2004.



Figure 6. Photo of damaged Continuous Global Positioning System (CGPS) station AV04, located on the upper west flank, after the 2006 eruption of Augustine volcano. The station was damaged by passing pyroclastic flow that ripped off the plastic radome, melted the coax antenna cable, conduit, and the middle of the L1/L2 choke ring antenna. Photo by Benjamin Pauk, September 2, 2006.

being set in concrete, it was further coupled to the ground using a minimum of four 3/16-inch diameter guy wires connected to 0.5×6 inch-long galvanized eyebolts on the swing set connected to another nongalvanized eyebolt cemented into available bedrock adjacent to the base of the swing set.

To minimize the time to install a complete station during the 2006 project, all swing sets were built at the base camp during weather delays and slung to each station by helicopter. Preconstruction of all equipment and programming of radios and receivers in the PBO warehouse before deployment to the island reduced the average site installation time from two days to one. During the 2006 installation period, Augustine was at Aviation Color Code Yellow and Volcano Alert Level Advisory indicating signs of elevated unrest and increased seismic activity at the volcano. Consequently, it was critical to minimize the amount of time spent working on the island in the event that volcanic activity increased, thereby necessitating a crew evacuation.

Network Installation Logistics

All operations for the 2004 and 2006 installations were based out of a camp established on the west side of the island adjacent to the informally named West Lagoon (fig.1). All gear, including huts, swing set materials, batteries, tools, and associated installation and camping equipment was transported to Augustine Island from Homer, Alaska, by the M/V *Maritime Maid* in 2004 and by the M/V *Kittiwake* in 2006. A Bell Long Ranger helicopter was used to sling all gear from the ships to the base camp staging area because no docks or landing areas are present on the island. Additional support, including equipment and crew transport to and from the island, was completed with float planes based in Homer. These support aircraft were able to take off and land in the lagoon. The lack of road and trails on the island required that a helicopter be used during both installations in order to provide logistical support and sling external loads of gear as well as transport internal loads of equipment and crew to and from each location on the island.

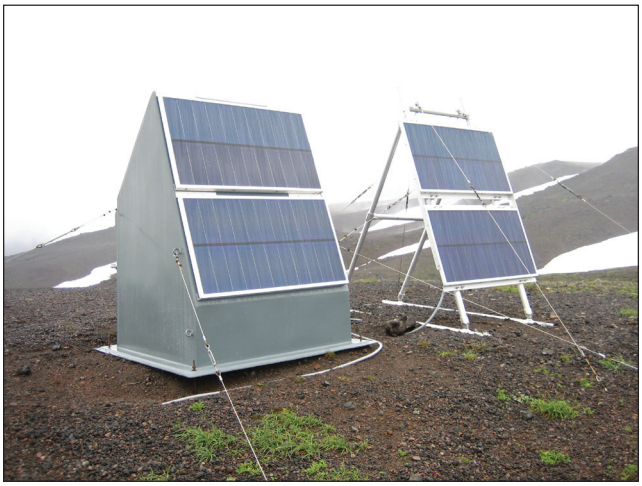


Figure 8. Photo of modified fiberglass enclosure and solar panel structure deployed on Augustine Volcano during the 2006 installations. The new enclosure can accommodate two 64 watt solar panels, and both the enclosure and swing set use guy wires for added anchoring to the ground. Photo by Dave Mencin, September 4, 2006.



Figure 7. Photo of deformed and decapitated Continuous Global Positioning System (CGPS) monument AV03 after the 2006 eruption. Trimble antenna, plastic radome, and leveling mount were ripped off and monument was deformed in direction of pyroclastic flow that swept over the monument. The swing set and fiberglass enclosures were completely destroyed and buried by flow deposits. Photo by Benjamin Pauk, September 3, 2006.

Current PBO Augustine Radio Network and Telemetry

Data from each existing GPS station in the Augustine network (except for AV20) are transmitted in real time through a point-to-multipoint, spread-spectrum 900 MHz ISM-band Ethernet radio network to a master radio located at the AVO communications facility in Homer (fig. 10). The radios are connected to an appropriate Yagi directional antenna mounted to vertical poles inside of each fiberglass hut. In some cases, an external mount on a 2-inch-diameter aluminum pole is used. The huts are transparent to frequencies in this 900 MHz range and protect the antenna from the elements. Stations AV04, AV16, AV17, and AV18 are stand-alone stations with only one slave radio located within the hut and transmit data to Homer through a repeater radio at PBO station AC59 16 km northwest of the volcano on the Alaska Peninsula at Ursus

Head. The slave radio connects to the NetRS GPS receiver through a standard CAT5 Ethernet patch cable. Station AV01, which serves as a slave repeater station, has two radios located in its hut. One is a slave radio that transmits data collected at AV01 to station AC59, whereas the second radio in the hut repeats data from AC27, located on the Alaskan Peninsula west of Augustine Island, to station AC59 and then to Homer (fig. 10). Data from stations AV02, AV11, and AV19 are routed directly to Homer. Station AV20 has no line of site to any other PBO station on the volcano or in the Cook Inlet region. As of this writing, the station is manually downloaded on a biannual basis and will be incorporated in to the existing radio telemetry at a later date.

PBO Augustine GPS Data Collection

The Trimble NetRS has 1 GB of internal memory for storing data and the standard operating procedures for all PBO CPGS is to split the data space on the receiver into two separate ring buffers, a 800 MB partition for data collection at 1 Hz to be used only during events such as a volcanic eruption, earthquakes, or other events of great scientific interest, and a 200 MB partition for daily data files with a 15 second data collection rate. The size of daily files sampled at the 15 seconds averages about 1 MB and it typically takes about six months to completely fill the 200 MB partition, at which point the receiver will overwrite older data.

Prior to the eruption, AVO requested PBO to set up three separate data partitions on each GPS receiver for simultaneous collection of three different sample rates. The three partitions stored daily and hourly files, both sampled at 15 seconds, and also hourly files sampled at 1 Hz. Prior to the eruption and request for additional sample rates, PBO only collected hourly and daily 15-second data files. Before, during, and after the eruption, all hourly 15-second data files were downloaded hourly whereas the 15-second daily files continued to be downloaded daily. During the explosive phase of the 2006 eruption, PBO collected and downloaded hourly 1-Hz data files from stations AV01 and AV02 on the volcano. Due to the large size of the 1-Hz data files and larger bandwidth requirements, the 1-Hz files were only collected for a few weeks during the explosive phases of the eruption and were no longer collected after the onset of the effusive phase of the eruption.

All raw data collected from the CGPS network on Augustine are available for download from the UNAVCO Data Archive Facility, with raw receiver files converted to standard Receiver Independent Exchange (RINEX) format for easy processing, analysis, and interpretation. In addition to raw data, PBO provides higher-level data products consisting of station position and velocity solutions in the Stable North America Reference Frame (SNARF), along with their related Solution Independent Exchange (SINEX) files. PBO's data analysis occurs at two analysis centers, one at the New Mexico Institute of Mining and Technology using the GAMIT processing package and the other at Central Washington University using the GIPSY processing package, with combined solutions generated at the Massachusetts Institute of Technology. These data products and the specific PBO Augustine data products collected before, during, and after the eruption can be accessed from the UNAVCO Archive Facility through the UNAVCO Web page at (http://www.unavco.org, accessed September 28, 2009) as well as directly from the PBO Web site at (http://pboweb.unavco.org, accessed September 28, 2009).



Figure 9. Photo of stainless steel back panel mounting system developed for new huts deployed during the 2006 Augustine Volcano installations. Trimble NetRS and Intuicom EB1 spread spectrum radio mounted on to upper portion of panel. Photo by Benjamin Pauk, September 4, 2006.

Conclusions

The original PBO CGPS network on Augustine Volcano was designed to follow the existing telemetry paths of the AVO seismic network, minimizing the need for extensive radio testing in the field. Extensive planning, organization, radio network development, and bench testing of the GPS and digital radio network in the laboratory prior to deployment proved extremely valuable in minimizing the amount of time spent in the field

troubleshooting the radio network. Additionally, the original radio network design was implemented to allow for expansion. Consequently, the PBO engineers in 2006 were able to incorporate the radios for the new stations without having to significantly alter the existing radio telemetry paths.

The destruction of three of the original six stations early in the eruption severely affected AVO's ability to use GPS as a key monitoring tool during the entire eruption. Had field conditions permitted, PBO field crews could have redeployed new equipment shortly after the eruption began to ensure continued data collection. This would have provided invaluable information about flank deformation of the volcano after the onset of the eruption. Unfortunately, severe winter weather and hazardous conditions on the volcano prevented access and work during the eruption.

The interval between the original 2004 network deployment and the 2006 eruption response deployment provided PBO engineers ample experience to make marked improvements to GPS monument construction and enclosure and electronics design. One fundamental lesson learned from the 2004 installations was the need for well-defined logistics for this type of operation. The 2004 installations on Augustine were the first large-scale deployment for PBO field engineers in Alaska and many logistical items, such as scheduling of boats, helicopter contracts, and equipment transport, was conducted late in the planning process. As a result, additional float plane charters were required to bring some tools and equipment not available at time of shipping to the island after the 2004 installations began. In 2004, all construction, including assembly of the huts and swing sets, was done on site, adding significantly to construction time at a site. Logistics and construction of the 2006 installations were streamlined by effective planning that began in October of 2005 and included a thorough organization of equipment and materials, additional acquisition of tools, and construction of the enclosures in the warehouse prior to shipment to the volcano.

Another valuable lesson learned during the time between the two installations was the need for a larger enclosure with an accessible and standardized equipment panel for easy access and rapid replacement of equipment. Between the 2004 and 2006 installations, enclosures were redesigned to accommodate more solar panels, which in some cases during the 2006 installations, removed the need for swing sets in areas of good southern exposure and historically low snow accumulation. These modifications allowed for efficient installation of the new CGPS stations at the request of the PBO Magmatic Systems Site Selection Committee in 2006. As a result of the streamlined construction procedures, PBO field engineers were able to reduce site construction time by about 50 percent from two days to one. In the future, these procedures will allow for stations to be built quickly, efficiently, and safely in remote volcanic settings before the onset of volcanic unrest. The lessons learned from the 2004 and 2006 installations, combined with the hut and swing set improvements and streamlined construction procedures, proved extremely valuable to PBO volcanic network installations on Unimak Island in 2008 and contributed to their success.

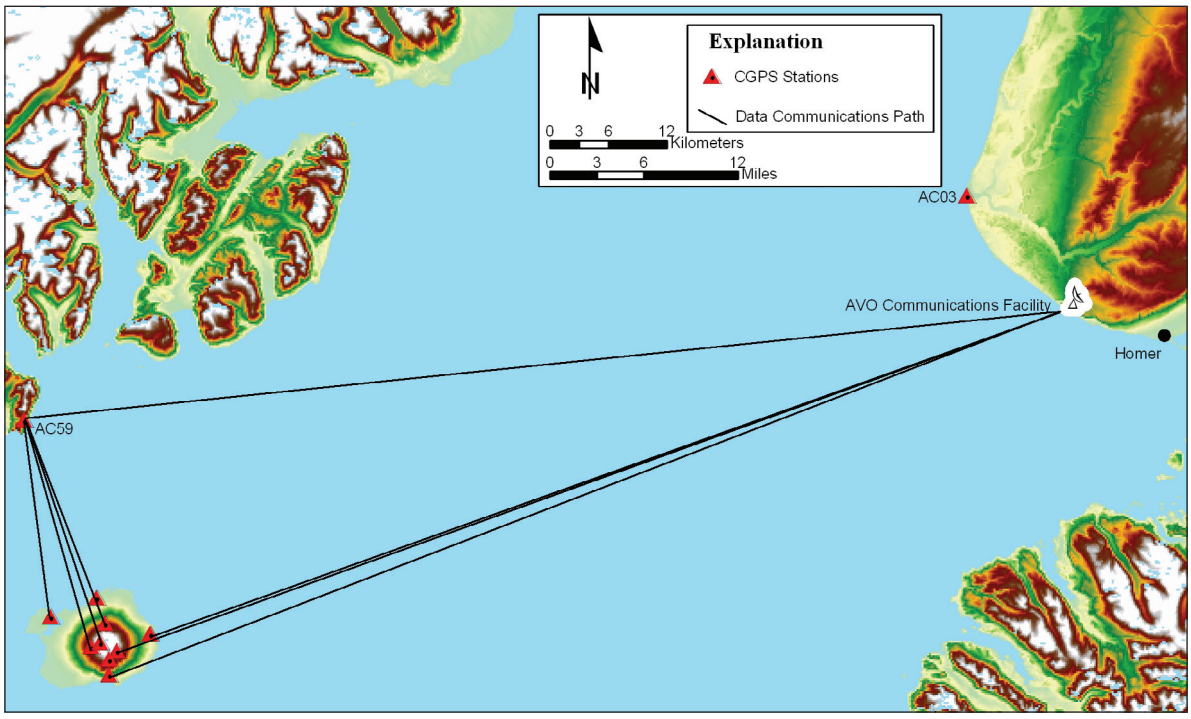


Figure 10. Regional map showing radio telemetry links of the Plate Boundary Observatory (PBO) Augustine Volcano GPS network. Map projection is Universal Transverse Mercator Projection, Zone 5, North American Datum of 1983 (NAD 83). CGPS, Continuous Global Positioning System.

Acknowledgments

The 2004 and 2006 GPS network installations on Augustine were both cooperative efforts involving personnel from UNAVCO, Inc., the Alaska Volcano Observatory, and the University of Alaska Fairbanks Geophysical Institute. Beluga Air, Kachemak Air Service, Maritime Helicopters, and Katmai Coastal Bear Tours provided safe, reliable, and efficient transportation of gear and crew to and from the island. The authors gratefully acknowledge all those who contributed to the success of both installations. We are also indebted to the support and advice from the Alaska Volcano Observatory for both installations; in particular we are grateful for the advice and assistance from Tom Murray, John Power, and John Paskievitch on permitting, logistics, and network operations. Material and results presented in this paper are based on data, equipment, and engineering services provided by the Plate Boundary Observatory operated by UNAVCO for EarthScope (http://www.earthscope.org, accessed September 28, 2009) and supported by the National Science Foundation (No. EAR-0323309).

References Cited

Cervelli, P.F., Fournier, T.J., Freymueller, J.T., Power, J.A., Lisowski, M., and Pauk, B.A., 2010, Geodetic constraints on magma movement and withdrawal during the 2006 eruption of Augustine Volcano, *in* Power, J.A., Coombs, M.L., and Freymueller, J.T., eds., The 2006 eruption of Augustine Volcano, Alaska: U.S. Geological Survey Professional Paper 1769 (this volume).

Cervelli, P.F., Fournier, T., Freymueller, J., and Power, J.A., 2006, Ground deformation associated with the precursory unrest and early phases of the January 2006 eruption of Augustine Volcano, Alaska: Geophysical Research Letters, v. 33, L18304, doi: 10.1029/2006GL027219.

Dzurisin, D., Iwatsubo, E.Y., Kleinman, J.W., Murray, T.L., Power, J.A., and Paskievitch, J.F., 1994, Deformation monitoring at Augustine Volcano, AK [abs.]: Eos, (American Geophysical Union Transactions), v. 75, n. 44, p. 166.

Murray, T.L., Endo, E.T., Iwatsubo, E.Y., and Dzursisin, D., 1996 A feasible real time radio-telemetered GPS network for short baseline applications [abs.]: Eos, (American Geophysical Union Transactions), v. 77 n. 46, p. 146.

Murray, T.L., Kleinman, J.W., Iwatsubo, E.Y., and Dzurisin, D, 1992 Establishment of a permanent radio-telemetered GPS network on Augustine Volcano, Cook Inlet, Alaska [abs.]: Eos, (American Geophysical Union Transactions), v. 73, n. 43, p. 124.

Pauk, B.A., Power, J. A., Lisowski, M., Dzurisin, D., Iwatsubo, E. Y., and Melbourne, T., 2001, Global Positioning System (GPS) survey of Augustine Volcano, Alaska, August 3–8, 2000—data processing, geodetic coordinates and comparison with prior geodetic survey: U.S. Geological Survey Open-File Report 01-0099, 20 p.

Power, J.A., and Iwatsubo, E.Y., 1998, Measurements of slope distances and zenith angles at Augustine Volcano, Alaska, 1986, 1988, and 1989: U.S. Geological Survey Open-File Report 98-145, 17 p.

Power, J.A., Nye, C.J., Coombs, M.L., Wessels, R.L., Cervelli, P.F., Dehn, J., Wallace, K.L., Freymueller, J.T., and Doukas, M.P., 2006, The reawakening of Alaska's Augustine Volcano: EOS, (American Geophysical Union), v. 87, no. 37, p. 373.

Appendix 1. Station and telemetry description of existing Plate Boundary Observatory (PBO) Augustine GPS network.

AV01: Station is located on the western flank of volcano on a prominent andesite outcrop. Radio telemetry path for the station is to PBO station AC59 located at Ursus Head, about 15 miles to the northwest, and is repeated to the AVO communications facility in Homer. AV01 also host a repeater radio that repeats data from PBO regional station AC27 located in McNeil River State Refuge. AV01 consists of an original style PBO fiberglass enclosure, swing set, and SDBM.

AV02: Station is located on the southern flank of the volcano on a prominent outcrop of sedimentary rock. The radio telemetry path is from the station directly to the AVO communications facility located in Homer. The station consists of an original style PBO fiberglass enclosure, swing set, and SDBM.

AV04: Station is located on the upper western flank of the volcano on a prominent flat spot. The radio telemetry path is to Homer through a radio repeater located at PBO station AC59. The station consists of an original style PBO fiberglass enclosure and SDBM.

AV11: Station is located in bedrock on the western end of a low lying east-west trending ridge on the northeastern side of the volcano. The radio telemetry path is directly to the AVO communications facility in Homer. The station is near the old AVO GPS station AUGL and consists of an older style AVO fiberglass enclosure, swing set, and SDBM.

AV16: Station is located on a large rock outcrop west of the main lagoon on the west side of the island. The radio telemetery path is to Homer through a repeater radio located at PBO station AC59. Station consists of a newer style fiberglass enclosure, newer style swing, set and SDBM.

AV17: Station is located on a 20 foot diameter rock outcrop on the northern base of the volcano. The radio telemetry path is to Homer through a repeater radio located at PBO station AC59. The station consists of a newer style fiberglass enclosure and SDBM.

AV18: Station is located in bedrock on the prominent lava flow on the north side of the volcano within 100 feet of location of the destroyed PBO station AV03. The radio telemetry path is to Homer through a repeater radio located at PBO station AC59. The station consists of a newer style fiberglass enclosure, newer style swing set, and SDBM.

AV19: Station is located on a bedrock spine on the southwest flank of volcano. The radio telemetry is directly to the AVO communications facility in Homer. The station consists of a newer style fiberglass enclosure and SDBM.

AV20: Station is located on the southern flank of the volcano about 0.5 miles north of station AV02. The station is manually downloaded once every three months and is not currently part of the existing telemetry network. The station consists of a newer style fiberglass enclosure and SDBM.